Studies of Dust and Gas in the Interstellar Medium of the Milky Way

Francisco Javier Salgado Cambiazo

ISBN: 978-94-6259-803-4
Studies of Dust and Gas in the Interstellar Medium of the Milky Way, Thesis, Leiden University
170 pages; illustrated, with bibliographic references and summary in Dutch
Printed by Ipskamp Drukkers, Enschede
Cover design Francisco Salgado

Studies of Dust and Gas in the Interstellar Medium of the Milky Way

Proefschrift

ter verkrijging van
de graad van Doctor aan de Universiteit Leiden,
op gezag van de Rector Magnificus prof. mr. C. J. J. M. Stolker,
volgens besluit van het College voor Promoties
te verdedigen op woensdag 2 september 2015
klokke 10:00 uur

door

Francisco Javier Salgado Cambiazo

Geboren te Santiago, Chili
in 1983

Promotiecommissie

Promotor	Prof. Dr. A. G. G. M. Tielens
Co-promotores	Dr. J. B. R. Oonk
Overige Leden	Prof. Dr. H. J. A. Röttgering Prof. Dr. B. R. Brandl Prof. Dr. C. M. Walmsley Prof. Dr. A. Abergel Prof. Dr. G. J. White

Contents

List of Figures viii

List of Tables ix

1 Introduction 11
- 1.1 The Interstellar Medium of the Milky Way . . . 11
- 1.2 Low Frequency Carbon Radio Recombination Lines . . . 12
  - 1.2.1 CRRL Observations . . . 14
  - 1.2.2 LOw Frequency ARray (LOFAR) . . . 15
  - 1.2.3 Carbon Radio Recombination Line models . . . 16
- 1.3 HII Regions and Photodissociation Regions . . . 17
- 1.4 PAH and Dust Grains . . . 19
- 1.5 SOFIA FORCAST . . . 22
- 1.6 This Thesis . . . 23
- 1.7 Future Outlook . . . 26

2 First Results from SOFIA/FORCAST: The Mid-Infrared view of the Compact HII Region W3(A) 27
- 2.1 Introduction . . . 28
- 2.2 Observations and data . . . 29
- 2.3 Results . . . 31
  - 2.3.1 Observational analysis of W3A . . . 31
  - 2.3.2 Dust Spectral Energy Distribution . . . 34
  - 2.3.3 Lyman alpha dust heating . . . 34
  - 2.3.4 Dust-to-gas ratio . . . 35

3 The Orion HII region and the Orion Bar in the Mid-Infrared 37
- 3.1 Introduction . . . 38
- 3.2 Observations and Data . . . 40
- 3.3 Analysis . . . 42
  - 3.3.1 An Overall View of the Orion Nebula . . . 42
  - 3.3.2 The Orion Bar . . . 43

3.3.3 Spectral Energy Distribution Fitting 47
3.4 Results 53
3.4.1 Geometry of the Orion Bar 53
3.4.2 The Swept-up Shell 55
3.4.3 Dust extinction 55
3.5 Discussion 57
3.5.1 The Dust Temperature and Lyα Heating 57
3.5.2 Properties of the Dust 58
3.5.3 Dust in HII Regions 60
3.5.4 Cooling Lines and Photoelectric Heating Efficiency . . . 62
3.6 Summary and Conclusions 65

4 Low Frequency Carbon Radio Recombination Lines I: Calculations of Departure Coefficients 67
4.1 Introduction 68
4.2 Theory 70
4.2.1 Level Population of Carbon Atoms under Non-LTE Conditions 71
4.2.2 Numerical Method 74
4.2.3 Rates Used in this Work 75
4.3 Results 81
4.3.1 Departure Coefficient for Carbon Atoms 81
4.3.2 Comparison with Previous Models 86
4.4 Summary and Conclusions 92
A List of Symbols 95
B Level population 97
B.1 Hydrogenic atoms 98
C Radial Matrices and Einstein A coefficients 100
D Radiative recombination cross-section 101
E Energy changing collision rates 103
F Collisional ionization 103

5 Low Frequency Carbon Radio Recombination Lines II: The Diffuse Interstellar Medium 105
5.1 Introduction 106
5.2 Theory 108
5.2.1 Radiative transfer of carbon radio recombination lines . 108
5.2.2 The far-infrared fine structure line of C^+ 110
5.2.3 Line profile of recombination lines 111
5.3 Method 113
5.4 Results 114
5.4.1 Line widths 114

5.4.2 Integrated line to continuum ratio . . . 117
5.4.3 CRRLs as diagnostic tools for the physical conditions of the ISM . . . 120
5.5 On the Observed Behavior of CRRLs . . . 124
5.5.1 General considerations . . . 124
5.5.2 Illustrative examples . . . 126
5.5.3 Discussion . . . 129
5.6 Summary and Conclusions . . . 130
A List of Symbols . . . 132
B Radiative Transfer . . . 134
B.1 Doppler and Lorentzian broadening . . . 137
B.2 Collisional/Stark broadening . . . 138
C Radiation broadening . . . 138
C.1 The FIR fine structure line of C^+ . . . 141

6 Samenvatting **143**

Samenvatting **143**
6.1 Het belang van het interstellaire medium . . . 143
6.2 Koolstof Radio Recombinatie Lijnen op lage frequenties . . . 146
6.3 LOw Frequency ARray (LOFAR) . . . 146
6.4 Het belang van PAKs en interstellair stof . . . 147
6.5 SOFIA FORCAST . . . 148
6.6 Dit Proefschrift . . . 149
6.7 De toekomst . . . 151

Curriculum Vitae **153**

Acknowledgements **155**

Bibliography **168**

List of Figures

1.1 The phases of the ISM 13
1.2 Comparison of LOFAR LBA with WSRT observation 18
1.3 Observations and models of CRRLs towards Cas A 19
1.4 Example of using CRRL models and observations to constrain the physical parameters of a cloud 20
1.5 A schematic of a PDR 21
1.6 Examples of dust emission 23
1.7 Atmospheric transmission 24

2.1 Color image of W3 main region 30
2.2 SEDs for W3(A) 31
2.3 Cross-cuts for the W3(A) region 33

3.1 False color image for the Orion HII region 44
3.2 FORCAST images 45
3.3 A comparison between the 19 μm PDR-subtracted emission (green) and Hα 46
3.4 Cross-cuts for the Orion Bar 47
3.5 Comparison between dust emission and cooling lines 48
3.6 Examples of the SEDs at four positions. 52
3.7 Comparison between ^{13}CO and PACS emission 52
3.8 Temperature and optical depth maps of the two dust components revealed by the SED modeling. 53
3.9 Total infrared luminosity from the blackbody fits 54
3.10 Temperature as a function of distance for different dust grain sizes 59
3.11 Photoelectric heating efficiency map 63
3.12 Photoelectric heating efficiency plots 64

4.1 R value as a function of electron temperature 74
4.2 Comparison of energy changing collision rates 77
4.3 b_n and $b_n\beta_n$ values (right) for hydrogen at $T_e = 10^4$ and 10^2 K. 83
4.4 Example of hydrogenic b_{nl} values 84
4.5 Departure coefficients for the $^2P_{3/2}$ parent ions as a function of n 86

4.6 Final departure coefficients for carbon atoms (b_n^{final}) as a function of n level 87
4.7 $b_n^{3/2}$ values for carbon atoms 88
4.8 $b_n\beta_n$ values for carbon atoms at different temperatures and densities 89
4.9 Level where the $b_n\beta_n$ values go to zero 90
4.10 Difference between emissivities for low nl lines at low densities 90
4.11 A comparison of the effect of different collision rates on the final b_n values 91
4.12 Comparison between our b_n values and the results from Hummer and Storey (1992) 92
4.13 Departure coefficients from Ponomarev and Sorochenko (1992) 93

5.1 t_n factor as a function of electron density 113
5.2 A comparison between the continuum radiation fields. 115
5.3 A comparison between different line broadening mechanisms . . 116
5.4 α and β line width transitions for diffuse regions as a function of frequency for different power law radiation fields 118
5.5 Line-to-continuum ratio of CRRL as a function of principal quantum number (n) 119
5.6 Ratio of the excitation to background temperature (T_X/T_{bg}) . . 119
5.7 Integrated line to continuum ratio normalized to the value at the level $n = 500$ 121
5.8 Example ratio diagnostic plots for different electron temperatures and densities. 122
5.9 Level where lines transition from emission to absorption (n_t) as a function of electron density (N_e) 123
5.10 Comparison between the integrated line to continuum $I(\alpha)/I(\beta)$ ratio as a function of frequency for different densities 124
5.11 Ratio of the line to continuum ratio, for $n = 700$, to the carbon FIR line as a function of density. 125
5.12 Summary of the constraints derived from CRRL observations and models for Cas A 128
5.13 Summary of the constraints derived from CRRL observations and models for Galactic plane regions 129

6.1 Fases van het ISM 144
6.2 Voorbeelden van emissie door stof 150
6.3 Atmosferische transmissie 151

List of Tables

1.1 Main characteristics of the phases of the ISM (Ferrière, 2001). . 13
1.2 Physical characteristics of HII regions (Kurtz, 2005). 20
1.3 Filters characteristics and resolution of FORCAST for the filters used in this work. 24

3.1 FORCAST and PACS angular resolution 48
3.2 Properties of the central stars (Martins et al., 2005) 49
3.3 Spatial emission peaks 49

4.1 List of Symbols 95

5.1 Selected values for C$n\alpha$ and C$n\beta$ lines for regions observed by Erickson et al. (1995). 127
5.2 List of Symbols 132
5.3 Coefficients for Equation 5.16. 139

Chapter 1

Introduction

1.1 The Interstellar Medium of the Milky Way

Most of the light we see with our eyes on a dark night is produced by stars. However, a fraction of approximately 10 to 15 % of the mass of the Milky Way is in the interstellar medium (ISM), i.e. material between the stars. Stars are born from the ashes of previous generations of stars in the dense molecular clouds of the ISM and, as stars evolve, stars also inject energy into the ISM in the form of radiation, winds and jets. At the end of their lives, stars release larges amount of material back into the ISM and massive stars also release copious amounts of kinetic energy in the form of supernovae explosions. The material released becomes the seed of new generations of stars. This interplay between stars and the interstellar medium shapes and drives the evolution of galaxies.

The interaction of stars and gas in galaxies leads to the formation of the different phases of the ISM and manifests itself as a rich and complex dynamical system. The phases of the ISM are generally described as composed by three main phases (McKee and Ostriker, 1977; Cox, 2005) together with transient (shorter lived) clouds. In Figure 1.1, we show a diagram describing the different phases of the ISM.

Massive stars (O and B stars) play an important role as they emit a large fraction of their luminosity at ultraviolet wavelengths. In particular, these stars emit at wavelengths shorter than the ionization potential of hydrogen and they ionize hydrogen in their surrounding volume producing HII regions. In the boundary between their natal molecular cloud and the ionized volume a photodissociation region (PDR) is formed. In this region non-ionizing stellar photons dissociate molecules and ionize atoms with low ionization potentials (e.g. C, S, Na) and heat the gas.

As most of the EUV photons created by massive stars are consumed by gas inside the HII regions, a large fraction of the ISM is in a neutral state. Actually, most of the neutral ISM is a PDR (Hollenbach and Tielens, 1999). This neutral gas is divided in two regimes that are often considered to be in pressure equilibrium (Savage and Sembach, 1996; Cox, 2005): the cold neutral medium (CNM), viz. discrete clouds with low filling factor ($\sim 1\%$), low temperatures (~ 100 K) and densities ~ 50 cm^{-3}; and the warm neutral medium

(WNM) with temperatures of $\sim 10^4$ K and densities of ~ 0.1 cm^{-3} with a larger filling factor ($\sim 30\%$). These neutral phases are embedded into a warm and a hot ionized gas with filling factors of 20% to 70%. The warm ionized gas corresponds to regions where hydrogen ionizing photons escape from HII regions, and the hot ionized medium corresponds to old supernova remnants (McKee and Ostriker, 1977; Spitzer, 1990; Wolfire et al., 2003). Due to gravity, material is clumped together into molecular clouds, the densest regions of the Galactic ISM, where new stars are formed. A summary of representative temperatures and densities of the phases of the ISM is given in Table 1.1 (adapted from Ferrière 2001).

In the CNM, hydrogen is neutral, but stellar photons with energies between 11.2 and 13.6 eV can ionize carbon atoms. The diffuse clouds that compose the CNM are heated by photoelectric effect on PAH and dust grains. The cooling of the gas is dominated by emission of the [CII] at 157 μm far-infrared structure line. There is a large resemblance between the CNM and PDRs, in other words, the CNM can be described as a low density PDR. The lifecycle of the ISM plays an important role in th evolution of galaxies as the repository of the nucleosynthetic products from stars and the birth of new generation of stars. This cycling of material is not well understood, largely because of the lack of suitable observational probes. The radiative interaction of stars with their environments in the dense PDR of region of massive star formation (HII regions and PDRs) requires sensitive observations at mid and far infrared wavelengths which contain key diagnostic lines. This wavelength region has only opened with the launch of Spitzer in 2003 and Herschel in 2009. SOFIA is continuing this IR revolution.

The CNM and WNM are generally studied using transition lines at UV and optical wavelengths and observations of the 21 cm hyperfine transition of neutral atomic hydrogen (e.g. Weaver and Williams 1973; Kalberla et al. 2005; Heiles and Troland 2003b). However, deriving physical properties from UV and optical lines is difficult, as these tracers are affected by dust extinction. Deriving physical parameters of the neutral structures of the ISM from the 21 cm line is challenging because separating the cold and warm components is difficult (e.g. Heiles and Troland 2003a). In this work, we explore the of the IR emission to probe HII regions and PDRs and of low frequency carbon radio recombination lines to study the properties of gas in the CNM as a first step to towards understanding the lifecycle of the ISM in the evolution of galaxies.

1.2 Low Frequency Carbon Radio Recombination Lines

The ionization potential of carbon is lower than that of hydrogen and carbon can be ionized in regions where hydrogen is largely neutral such as the CNM.

Table 1.1: Main characteristics of the phases of the ISM (Ferrière, 2001).

ISM Phase	T (K)	n (cm^{-3})	Hydrogen state
Molecular	10-20	100-10^6	Molecular
Cold neutral	50-100	20-50	Neutral atomic
Warm neutral	6000-10000	0.2-0.5	Neutral atomic
Warm ionized	8000	0.2-0.5	Ionized atomic
Hot ionized	10^6	~ 0.0065	Ionized atomic

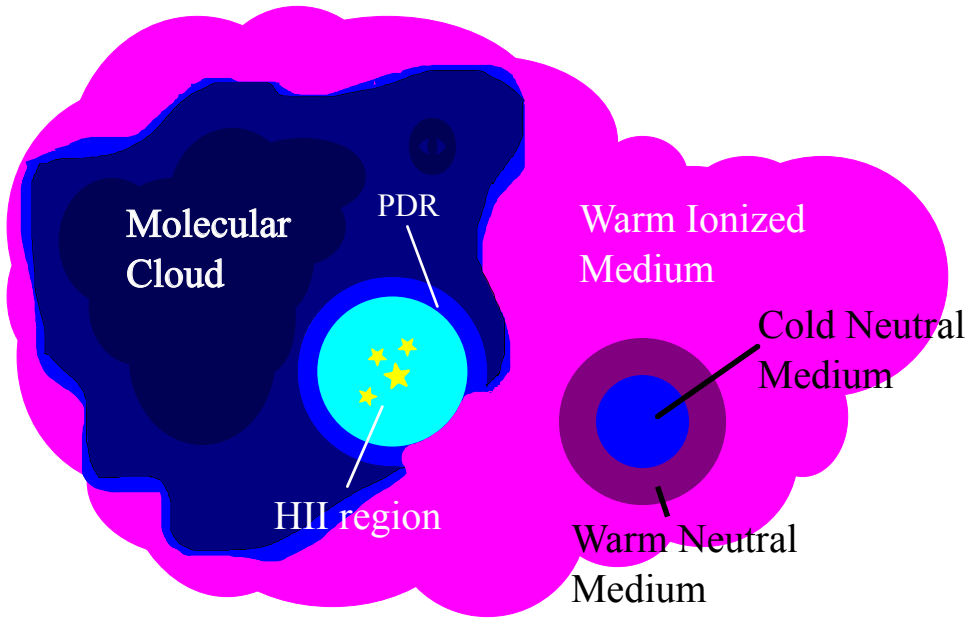

Figure 1.1: A schematic representation of a region in the interstellar medium of the Milky Way.

Lines produced by carbon can be used as probes of the physical properties of the ISM. In particular, transitions between high Rydberg states leads to the production of Carbon Radio Recombination Lines in the sub-millimeter to decameter range. At these long wavelengths, dust extinction is not important, in contrast to UV and optical carbon lines.

1.2.1 CRRL Observations

The first carbon recombination lines in the radio regime (5 GHz) were detected in emission towards NGC 2024 and IC 1795 (Palmer et al., 1967). Nowadays, these "high" frequency carbon recombination lines are known to be occur in PDRs associated with HII regions and have been detected towards other known HII regions (e.g.: Balick et al. 1974; Knapp et al. 1976a; Pankonin et al. 1977; Vallee 1987, 1989; Roelfsema and Goss 1991; Natta et al. 1994; Garay et al. 1998; Quireza et al. 2006) and reflection nebula (e.g.: Brown and Knapp 1974; Knapp et al. 1976b; Pankonin and Walmsley 1978b,a). Crutcher (1977) detected carbon recombination lines in emission towards ζ Ophiuchi and *o* Persei. In contrast to the lines detected by Palmer et al. (1967), the lines detected by Crutcher (1977) are associated with cold diffuse clouds.

The first low frequency (26.1 MHz) CRRL was detected in absorption towards the supernova remnant Cas A by Konovalenko and Sodin (1980) and it was wrongly attributed to a hyperfine structure line of ^{14}N (Konovalenko and Sodin, 1981). This first detection corresponds to a transition occurring between high quantum levels ($n = 631$). After this first detection, several other low and high frequency CRRLs have been observed towards Cas A (e.g. Ershov et al. 1984; Anantharamaiah 1985; Sorochenko and Walmsley 1991; Anantharamaiah et al. 1994). Recently, transitions involving levels as high as $n = 1009$ have been observed (Stepkin et al., 2007). This transitions correspond to the largest atoms found in space, with sizes of about 50 μm. Erickson et al. (1995) performed a survey of the Galactic plane (from Galactic longitude $l = 340^\circ$ to $l = 20^\circ$) at 76 MHz using the 64 m telescope at Parkes Observatory. With a large beam of 4° they detected lines in roughly 50 fields. Kantharia and Anantharamaiah (2001) presented observations at 34.5 MHz using the low-frequency dipole array (at Gauribidanur, India) with an angular resolution of $\sim 21' \times 25\,\mathrm{deg}$; and at 327 MHz using the Ooty Radio Telescope with two angular resolutions ($2^\circ \times 2^\circ$ and $2^\circ \times 6'$). Nine out of the 32 regions observed at 34.5 MHz were detected in absorption, while seven out of the twelve were detected in emission at 327 MHz with seven detections being common to both frequencies. Roshi et al. (2002) expanded the Galactic survey in search for recombination lines at 327 MHz using the Ooty Radio Telescope. As Kantharia and Anantharamaiah (2001) they used two angular resolutions ($2^\circ \times 2^\circ$ and $2^\circ \times 6'$) and concluded that diffuse C^+ regions show structure from $6'$ to 5° and structure over $\sim 6'$ owing to clumps.

The above mentioned studies show that CRRLs are widespread throughout the Galaxy; however, observations of low frequency CRRLs has been challenging because CRRLs are intrinsically faint with line to continuum ratios of about 10^{-4} to 10^{-3}. Even for the CRRLs detected towards Cas A, arguably the strongest CRRLs observed up to this date, the observed optical depth of

the line is $\sim 10^{-3}$. Furthermore, detailed interpretation of the results has been hampered by the velocity resolution of the instruments used to observe the lines, e.g. the line widths observed by Kantharia and Anantharamaiah (2001) are dominated by Galactic rotation. Therefore, to study low frequency CRRLs from the ISM, sensitive observations at high angular and velocity resolution are required.

1.2.2 LOw Frequency ARray (LOFAR)

The Low Frequency Array (LOFAR, van Haarlem et al. 2013) is an aperture synthesis array composed of phased array stations. The antennas in each station form a phased array, producing one or many station beams on the sky. Multi-beaming is a major advantage of the phased array concept. It is not only used to increase observational efficiency, but may be vital for calibration purposes. The phased array stations are combined into an aperture synthesis array. The Remote Stations are distributed over a large area in the Netherlands and Europe. There are two distinct antenna types: the Low Band Antenna (LBA) operates between 10 and 90 MHz and the High Band Antenna (HBA) between 110 and 250 MHz. The stations are distributed over an area about one hundred kilometers in diameter (located in the North-East of the Netherlands). Other stations are located in Germany, Sweden, the UK and France.

LOFAR is opening the low frequency sky to systematic studies of low frequencies carbon radio recombination lines due to its increased sensitivity and high angular resolution. Recent high angular resolution (beam size of $40''$) observations of CRRLs using LOFAR towards the line of sight of Cas A (Asgekar et al., 2013) have shown the structure of the clouds towards the supernova remnant. Moreover, the high spectral resolution of LOFAR allow us, for the first time, to separate the multiple velocity components towards Cas A (Oonk et al., 2015a; Salas, 2015) even at low frequencies. Furthermore, new detections towards Cyg A (Oonk et al., 2014) and the first extragalactic detection in the starburst galaxy M82 (Morabito et al., 2014a) demonstrate the high potential of LOFAR for CRRLs investigations.

Pilot studies have demonstrated that surveys of low frequency radio recombination lines of the galactic plane are within reach, providing a new and powerful probe of the diffuse ISM. These new observations have motivated us to reassess the recombination line theory, relax some of the approximations made by previous works and to expand the range of applicability of in terms of temperature, density and the importance of external radiation fields on the strength of the lines.

1.2.3 Carbon Radio Recombination Line models

The use of CRRLs as probes of the ISM requires detailed modeling to interpret the observations. After the first observations of carbon recombination lines at high frequencies(Palmer et al., 1967), it was proposed by Goldberg and Dupree (1967) that the observed properties were not compatible with local thermodynamic equilibrium. Instead, they determined that the level population was enhanced by dielectronic recombination. Zuckerman and Palmer (1968) suggested that the "anoumalous microwave recombination line" was due to carbon in the outer parts of HII regions. Later observations confirmed that the high frequency carbon recombination lines originated in HI regions surrounding the ionized gas of the HII region (i.e. a PDR). Studies of low temperature carbon lines towards PDRs were carried out by (Brocklehurst, 1973), Dupree (1974) and Hoang-Binh and Walmsley (1974).

The discovery of low frequency CRRLs observations by Konovalenko and Sodin (1981) demonstrated the presence of Rydberg Carbon atoms in space. These observations challenged the theory of carbon recombination lines and new models were required to interpret the observations. Later theoretical works by Watson et al. (1980); Walmsley and Watson (1982a) showed that, at low temperatures ($T_e \lesssim 100$ K), electrons can recombine into carbon ions by simultaneously exciting the ${}^2P_{1/2} - {}^2P_{3/2}$ fine structure line. Watson et al. (1980); Walmsley and Watson (1982a) modified the model from Brocklehurst (1970) for hydrogen recombination lines to include the dielectronic recombination process. There are two important assumptions in Brocklehurst (1970) model: the assumption of an statistical distribution of the angular momentum levels, and an asymptotic behavior of the level population towards local thermodynamic equilibrium. The first assumption is not valid if dielectronic processes need to be included. Therefore, in order to incorporate the dielectronic process into the model, a prescription is given by Walmsley and Watson (1982a) that takes into account the non-statistical distribution of angular momentum levels by considering the angular momentum changing collisions.

The dielectronic recombination process occurs to high n states and can explain the behavior of the high n CRRLs observed towards Cas A (Walmsley and Watson, 1982b). Ponomarev and Sorochenko (1992) suggested to compute the level population of the ${}^2P_{1/2} - {}^2P_{3/2}$ fine structure line self consistently. A new class of models was proposed by Payne et al. (1994), where the assumption of the level population tending to equilibrium at high quantum level was replaced by a complete depopulation of these high-n states.

Incorporating information from the [CII] line can provide additional information on the physical properties of the observed clouds, theoretical work in this direction was carried out by Natta et al. (1994); Sorochenko and Tsivilev (2000).

It is of importance to mention that all these previous theoretical works tried to explain the observations towards Cas A. In particular, the integrated optical depth as a function of quantum number. As we mention in the previous section, these observations were carried out with single dish telescopes with large beams and low velocity resolution and at high quantum number the quality of the observations is poor (see e.g. Payne et al. 1994).

However, new observations carried out by LOFAR have been able to separate the multiple components (see Figure 1.2). This new LOFAR observations have motivated the studies of CRRLs presented here. In this work we make use of increased computer power to solve the level population problem considering a much large number of levels than ever before. Furthermore, recent works (Vrinceanu et al., 2012) have updated the collisional rates values, providing more accurate results on the level population distribution and, consequently, to better models for the lines. In Figure 1.3, we exemplify this by showing a fit to the LOFAR Cas A data Oonk et al. (2015a). In Figure 1.4, we show how restrictions from CRRLs observations together with the [CII] at 158 μm can be effectively used to constraints the density and temperature of the intervening clouds.

1.3 HII Regions and Photodissociation Regions

Massive stars are formed in dense molecular clouds, the exact process to form massive stars is currently not well understood and two main mechanisms have been proposed: monolithic collapse and competitive accretion (e.g. McKee and Ostriker 2007; Zinnecker and Yorke 2007). Regardless of the mechanism, as a massive star turns on it releases a large amount of ultraviolet energy at wavelengths shorter than the ionization potential of hydrogen (13.6 eV, EUV photons) creating a bubble of ionized gas known as a HII region. The increase in temperature and pressure in the HII region leads to an expansion of the ionized volume, at this stages the HII region is referred to as ultra compact and compact. The expansion continues until the bubble bursts out and the gas inside the ionized bubble vents out into the ISM, reaching the state of a champagne flow (Tenorio-Tagle, 1979; Wood and Churchwell, 1989; Churchwell, 2002). We summarize the properties of HII regions at different evolutionary stages in Table 1.2 adapted from (Kurtz, 2005).

The expansion of the HII region leads to the creation of a photodissociation region (PDR), where far-ultraviolet (FUV) stellar photons can penetrate into the molecular cloud and dissociate molecular hydrogen. In addition, photons with energies larger than 11.2 eV can ionize carbon atoms. Due to high density and dust extinction, photons with longer wavelengths are absorbed deeper in the PDR leading to an "onion-like" ionization/molecular structure (Tielens and

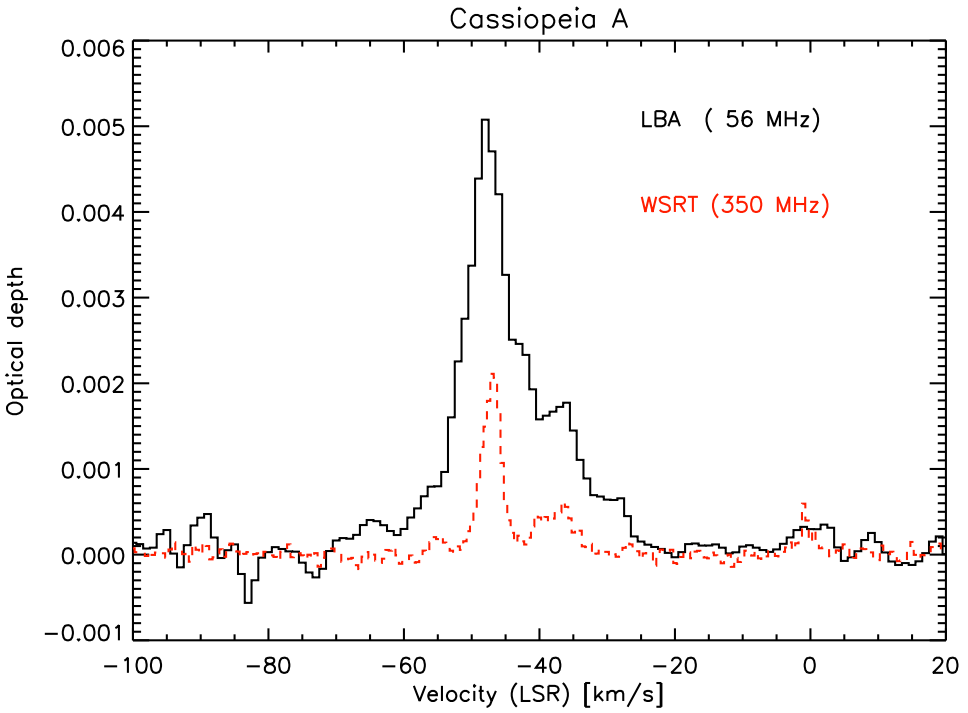

Figure 1.2: A comparison of LOFAR LBA spectra at 56 MHz and WSRT observations at 350 MHz, the high velocity resolution of LOFAR allow us to separate the cloud components even at low frequencies where line broadening from radiation dominates (Oonk et al., 2015a).

Hollenbach 1985; Hollenbach and Tielens 1999, Figure 1.5). In the inner regions of the PDR, H_2 and CO remain in their molecular form as the stellar photons reaching these zones are not energetic enough to dissociate these molecules.

The heating of PDRs is mainly produced by photoelectric effect (e.g. Bakes and Tielens 1994), viz. photons with wavelengths in the FUV regime ionize small grains and PAHs and the electrons ejected out of the grains heat the surrounding gas. The temperature of the gas is determined by the balance between the photoelectric heating and gas cooling. Cooling is dominated by emission of far-infrared fine structure lines [CII] at 157 μm and [OI] at 63 μm, with minor contribution to the cooling due to CO and H_2 emission.

Early studies using the IRAS satellite (Neugebauer et al., 1984) showed that at infrared wavelengths HII regions are strong emitters. This emission is produced by dust grains heated by radiation emitted by the central star. However, due to the low spatial resolution of IRAS ($\sim 4'$), mostly global energetic assessments could be done. More recent studies using higher resolution instru-

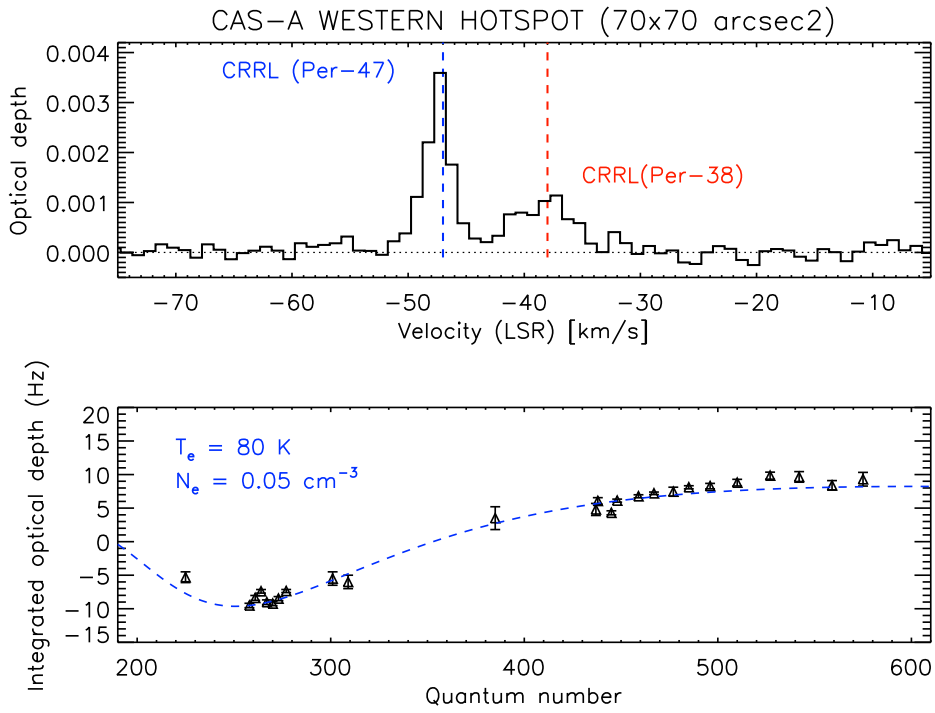

Figure 1.3: Upper panel: An spectra of the Cas A (Salas, 2015) at 355 MHz two components can be clearly seen at −47 and −38 km s^{-1}. Lower panel: a fit to a combined data set from the literature (Payne et al., 1989; Kantharia et al., 1998), WSRT, LOFAR observations of the CRRLs in the −47 km s^{-1} component towards Cas A.

ments with ISO (Peeters et al., 2002) and *Spitzer* (GLIMPSE and MIPSGAL survey, Benjamin et al. 2003; Churchwell et al. 2009; Carey et al. 2009) have greatly expanded our knowledge on the spatial distribution of dust in HII regions. Deharveng et al. (2010) showed that extended bright emission at 24 μm is spatially associated to ionized gas, as traced by 20 cm continuum emission. On the other hand, 8 μm emission is associated with the PDRs surrounding the ionized gas.

1.4 PAH and Dust Grains

Dust grains are an important component of the ISM. Mostly composed by two distinct chemically different species: carbonaceous and silicates, dust grains contribute to reddening and extinction at ultraviolet and optical wavelengths, absorbing stellar light and re-emitting it at longer wavelengths, thus dominat-

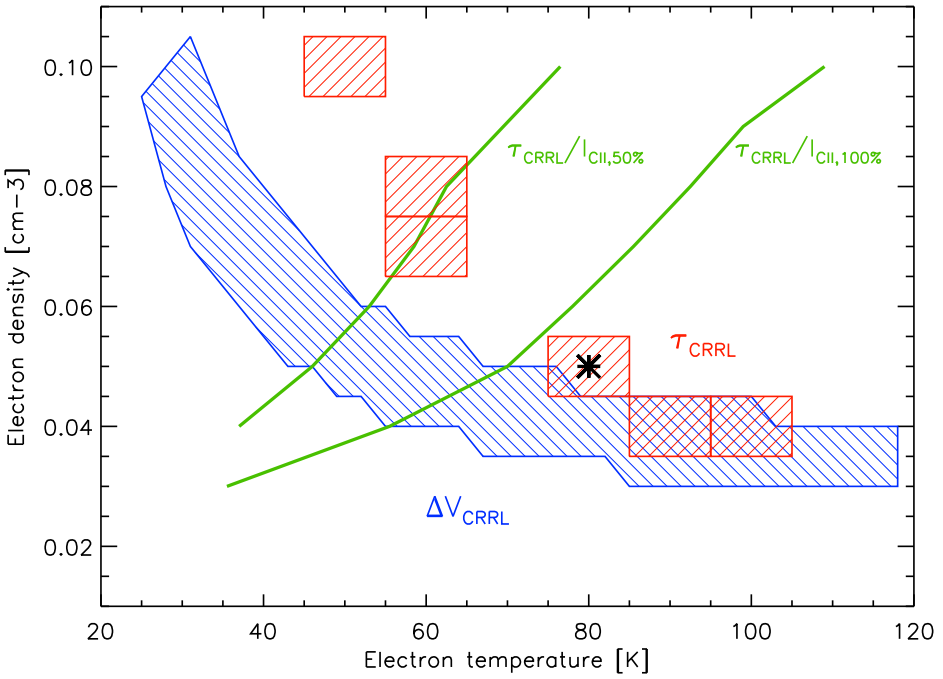

Figure 1.4: An example of the use of CRRLs together with [CII] line (green lines) and line width constraints (blue regions) towards Cas A (Oonk et al., 2015a). The star marks the model with the best fit, red boxes show other good fits to the data. The physical properties of the cloud can be well constrained.

Table 1.2: Physical characteristics of HII regions (Kurtz, 2005).

ISM Phase	n (cm^{-3})	size (pc)
Hyper Compact HII region	$\gtrsim 10^6$	0.03
Ultra Compact HII region	$\gtrsim 10^4$	~ 0.1
Compact HII region	$\sim 10^3$	~ 0.5
Classical HII regions	$\sim 10^2$	~ 10

ing the emission at infrared to sub-millimeter wavelengths. The luminosity of (ultra) luminous infrared galaxies [(U)LIRGs] and starburst galaxies is largely emitted through dust emission. Dust infrared emission can be a convenient tracer of star formation rate (e.g. Calzetti et al. 2007). Infrared emission due to dust in galaxies has been detected at redshifts as high as $z \approx 9$ (e.g. Watson et al. 2015) and is an important probe of the properties of galaxies at high

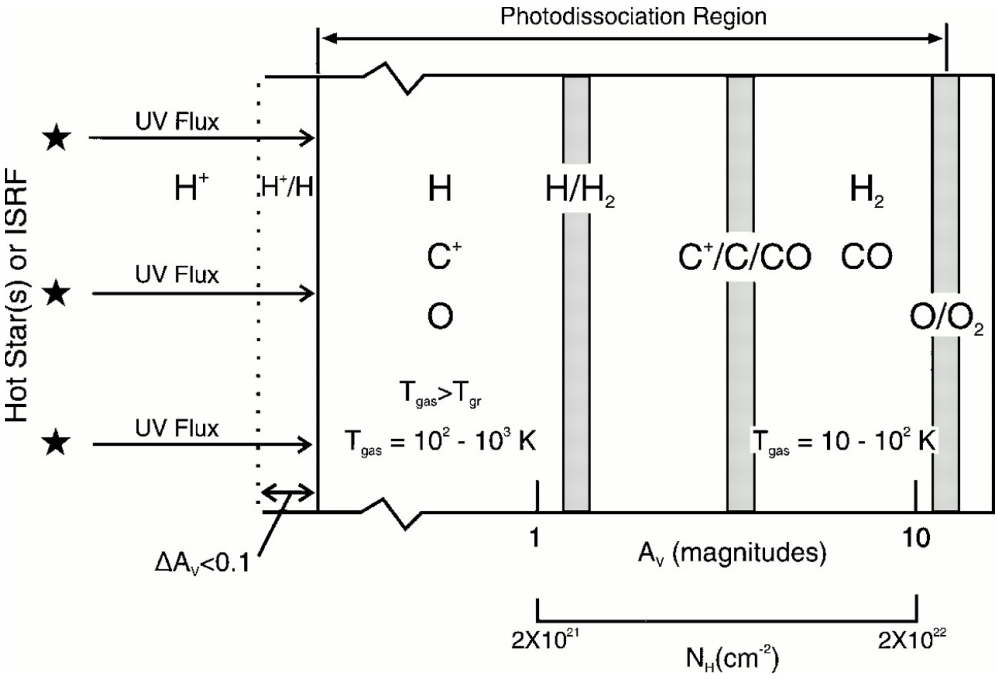

Figure 1.5: A schematic representation of a photodissociation region.

redshifts. At low temperature and large densities, molecules can form on the surface of dust grains driving the chemistry of the ISM. Moreover, in protoplanetary discs, dust grains are the building blocks of rocky planets such as Earth (e.g. Blum and Wurm 2008; Krijt et al. 2015).

Dust grains show a distribution in size ranging from small polycyclic aromatic hydrocarbons (PAH, large carbonaceous molecules formed by carbon rings) to micron size carbonaceous and silicate grains (Draine, 2003; Zubko et al., 2004). Extinction measurements show that the dust size distribution changes within the Galaxy (e.g. Cardelli et al. 1989). It has been shown that the size distribution of dust grains can be described by a power law $n(a) \propto a^{-3.5}$, with a the radius of a grain. This power law is usually referred to as the MRN distribution from Mathis et al. (1977) (e.g. Draine 2003). It is generally accepted that dust grains are formed by condensation in the wind of asymptotic giant branch (AGB) stars, Wolf-Rayet stars, novae and in the ejecta of supernovae (e.g. Draine 2009). However, the actual injection rates are very uncertain and it is usually believed that a large fraction of dust is produced in the ISM.

As dust grains interact with gas and radiation, the properties of dust change

and these changes are related to the environment. Therefore, it is important to understand how dust properties change. During their time in molecular clouds dust grains can grow through accretion of ice mantles and coagulation (Ossenkopf and Henning, 1994; Ormel et al., 2011). In contrast, dust grains can be easily destroyed in shocks by sputtering, releasing their constituent material back to gas phase. Other sources of dust destruction include vaporization when grains are exposed to strong radiation fields and shattering due to grain-grain collisions (Tielens et al., 1994; Jones et al., 1996).

In Figure 1.6, we show models for dust emission in two environments: the diffuse ISM and a dense PDRs. It can be seen that the light emitted by dust grains is mostly observed at wavelengths between 1 and 1000 μm. However, observations at these wavelengths are difficult from earth because the atmosphere of Earth blocks a large fraction of the light (upper panel in Figure 1.7).

1.5 SOFIA FORCAST

The Stratospheric Observatory for Infrared Astronomy (SOFIA) consists of a telescope of 2.7 m in diameter aboard a modified Boeing 747SP. By flying at high altitudes (12 to 14 km), it can observe above the water vapor layer of the atmosphere where the infrared atmospheric transmission is greatly increased (Figure 1.7). SOFIA started its observations in May 2010 and is planned to have a lifetime of 20 years. Details about SOFIA early observations and capabilities can be found in Young et al. (2012).

Among the first instruments on SOFIA is the Faint Object InfraRed Camera for the SOFIA Telescope (FORCAST, Herter et al. 2012). FORCAST is a two channel mid-infrared camera with a short wavelength detector (SWC) ranging from 5 to 25 μm and a long wavelength detector (LWC) covering from 25 to 40 μm. Images can be obtained using the detectors individually or simultaneously, by using a dichroic mirror. In addition, FORCAST also is capable of grism spectroscopy in the 5-50 μm range. The wavelength coverage of FORCAST is perfectly suited for studying dust emission in HII regions and PDRs as the peak of the dust SED is expected to be located at these wavelengths (cf. Figure 1.6). In addition, the relatively large field of view of the FORCAST camera ($\sim 3.2' \times 3.2'$) and the pixels scale ($0.768''$/pixel) makes the instrument well suited to observe extended regions in the Galaxy. Now that SOFIA is in operations, detailed spatially resolved (see Table 1.3) studies of dust emission from HII regions have come in reach. The studies of HII regions presented in this thesis are among the first that have made use of these new capabilities offered by SOFIA to characterize dusty HII regions.

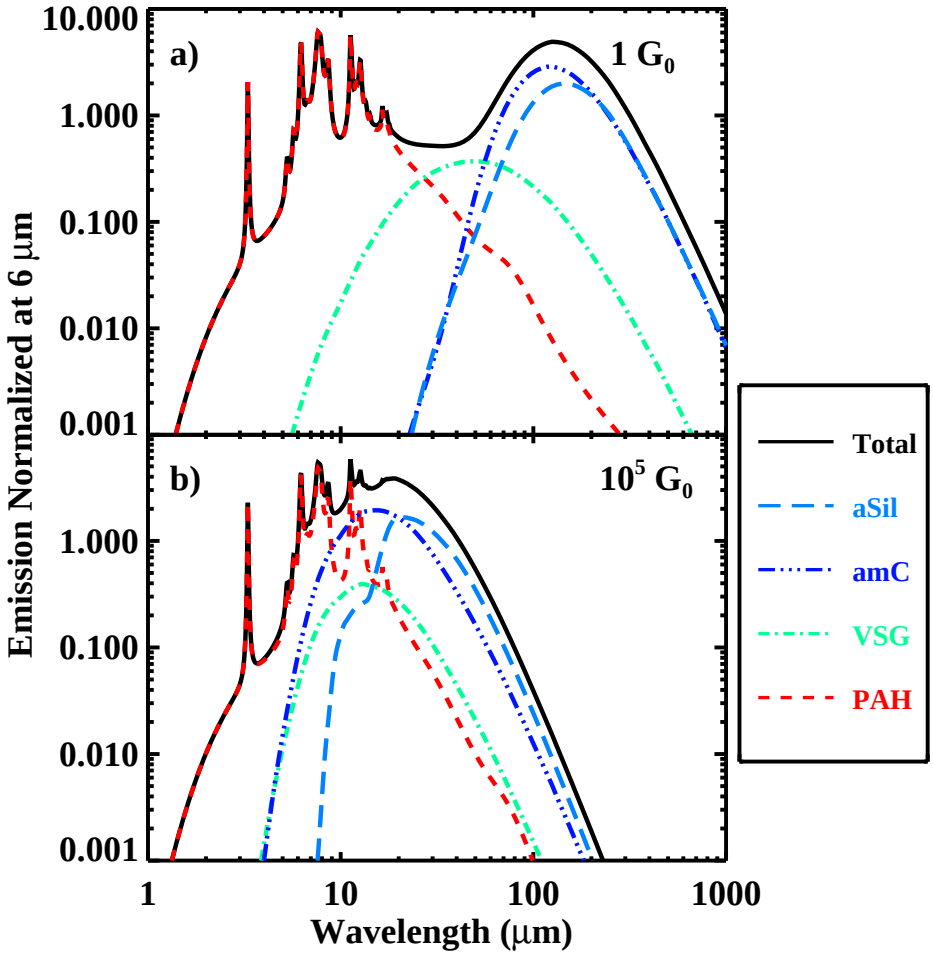

Figure 1.6: Dust emission produced by the Dustem code (Compiègne et al., 2011) in two cases: a) Under the FUV local radiation field (1 G_0 = 1.6 × 10^{-3} erg s^{-1} cm^{-2}), similar to the radiation field observed by the diffuse ISM. b) Under a radiation field larger than the local FUV radiation field (10^5 G_0), similar to the radiation field observed by a PDR close to a massive star. Red lines correspond to emission produced by PAHs, cyan lines by very small grains, light blue is emission produced by large carbonaceous grains and dark blue by silicates.

1.6 This Thesis

This Thesis can be considered to have two parts: in the first one we present a study of the dust properties in HII regions and their surrounding PDRs. We

Table 1.3: Filters characteristics and resolution of FORCAST for the filters used in this work.

Wavelength (μm)	$\Delta\lambda$ (μm)	FWHM ($''$)
6.4	0.14	2.9
6.6	0.24	3.0
7.7	0.47	2.7
19.7	5.5	2.9
31.5	5.7	3.4
37.1	3.3	3.6

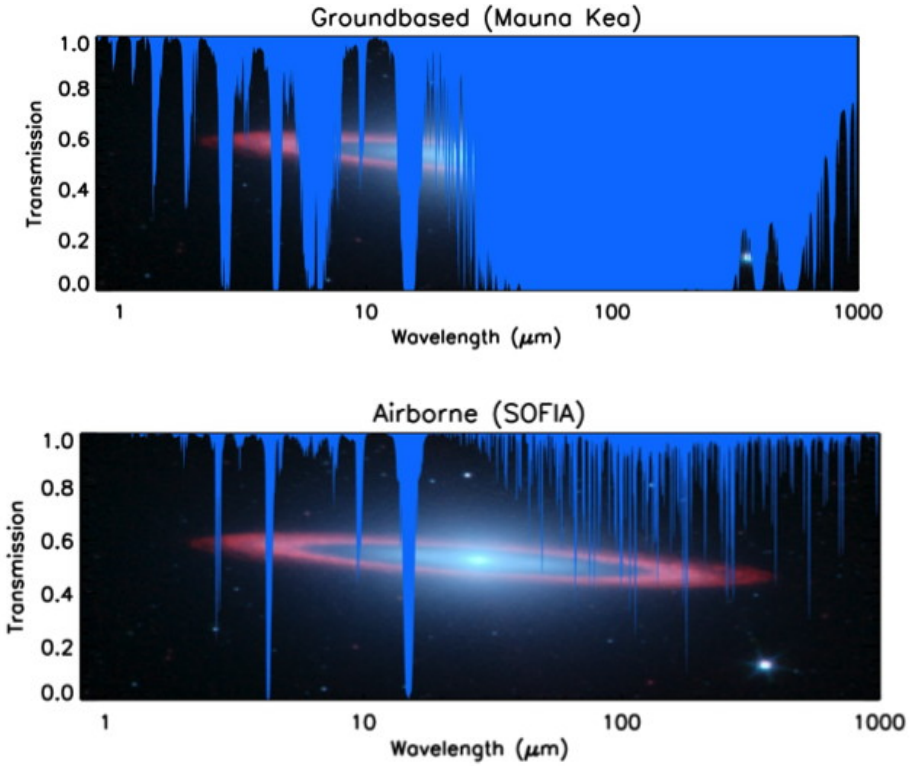

Figure 1.7: Comparison between the atmospheric transmission at Mauna Kea and that achieved by SOFIA. The atmospheric transmission is greatly increased at wavelengths larger than 20 μm at the altitudes that SOFIA is able to observe.

focus our studies on two compact HII regions: W3(A) and the Orion Nebula. The second part of this thesis presents theoretical studies of the properties of the cold neutral medium using carbon radio recombination lines.

In Chapter 2, the study towards W3(A) is presented. We used SOFIA/FORCAST photometry to characterize the dust emission in the region. The photometry is used to construct spectral energy distribution (SED) maps to study the dust abundance and temperature in this region. A strong spatial correlation between dust emission and ionized gas tracers is found. By using the properties of the star, a simple model is proposed with dust and gas well mixed within the ionized gas. The dust in the ionized gas must have different properties as compared to dust in the diffuse ISM in order to explain the size of the region.

A study of dust grains in the Orion Nebula is presented in Chapter 3. The Orion Nebula is one of the best studied star forming regions and a wealth of supporting data is available at all wavelengths. In this work, we show new observations performed by SOFIA with the FORCAST instrument. The SOFIA/FORCAST data is complemented with *Herschel*/PACS photometry. This allow us to characterize the complete infrared SED of the region including the far infrared tail of dust emission. We compare the FORCAST and PACS images with data from the literature and find that the PACS images trace a cold dust component located in the molecular cloud. The FORCAST data is found to be produced by warm dust in the HII region and by the background PDR. We characterize the dust properties in the PDR and the HII region and, as for W3(A), the dust properties must be different to those in the diffuse ISM. A comparison of dust emission and cooling lines is used to characterize the photoelectric heating efficiency in the Orion Bar PDR.

In Chapter 4, we construct models to determine the level population of atoms at low temperatures and densities. The focus of this study is to characterize the level population of carbon atoms under the (non-LTE) conditions of the diffuse ISM in terms of departure coefficients. Based on hydrogenic models from the literature, we expand the range of validity of approximations to the high quantum levels of the observed radio recombination line transitions. Among the physical properties that determine the level population, the most critical parameter to accurately model for the level population is the dielectronic recombination.

In Chapter 5, we used the level population models from Chapter 4 to model the line emission and absorption towards clouds with temperatures and densities of the CNM. We analyze the line widths properties and solve the radiative transfer equation assuming a model for the galactic synchrotron radiation field and the cosmic microwave background (CMB) emission. The models are used to describe methods for how to use CRRL observations to determine the physical properties more effectively and we provide illustrative examples using data from the literature. These models are currently being used to determine the physical conditions of diffuse atomic clouds observed with LOFAR.

1.7 Future Outlook

In coming years, new telescopes are expected to start operating. These new instruments will further increase our knowledge on the physics of the ISM and the studies presented in this thesis will be expanded.

As the Planck results (Planck Collaboration et al., 2011) as well as the observations presented in this thesis demonstrate, properties of dust in regions of massive star formation are very different from those of dust in the diffuse ISM. The launch of the James Webb Space Telescope (JWST) is expected to occur in October 2018 and will greatly expand this field. With a telescope of 6.5 m, JWST will carry the largest mirror ever launched into space. Among the instruments onboard JWST, the Mid-Infrared Instrument (MIRI) will be able to perform imaging and spectroscopical studies of dust in HII regions from 5 to 28 μm with high angular resolution and high sensitivity. The spectroscopic and photometric capabilities of JWST/MIRI can extend the study of HII regions in our galaxy to much fainter levels as well as to nearby galaxies and thus probe a much larger range of physical characteristics (density, metallicity, stellar cluster size, etc.) at unprecedented resolution. Such studies will be key to understand observations of massive star formation at redshifts of ~ 1.

As the first LOFAR studies demonstrate and the results of this thesis quantify, CRRLs provide a powerful probe of the physical conditions in the cold phases of the ISM. The Square Kilometer Array (SKA) will be the next generation of low frequency observatories and will greatly improve our studies on CRRLs. Being located in the southern hemisphere, SKA will be able to map the Galactic Center and the Magellanic Clouds in search for CRRLs. SKA will be perfectly suitable for Galactic studies of the large scale behavior of CRRLs as well as small scale (pinholes) and extragalactic studies (Morabito et al., 2014a).

Chapter 2

First Results from SOFIA/FORCAST: The Mid-Infrared view of the Compact HII Region W3(A)

Based on: Salgado, F. et al., 2012

Abstract

The massive star forming region W3 was observed with the faint object infrared camera for the SOFIA telescope (FORCAST) as part of the Short science program. The 6.4, 6.6, 7.7, 19.7, 24.2, 31.5 and 37.1 μm bandpasses were used to observe the emission of Polycyclic Aromatic Hydrocarbon (PAH) molecules, Very Small Grains and Big Grains. Optical depth and color temperature maps of W3A show that IRS2 has blown a bubble devoid of gas and dust of ∼0.05 pc radius. It is embedded in a shell of ionized gas, where dust is present that contributes 40% of the total emission at W3A at 24 μm. This dust component is mostly heated by far ultraviolet, rather than trapped Lyα photons. This shell is itself surrounded by a thin (∼0.01 pc) photodissociation region where PAHs show intense emission. The infrared spectral energy distribution (SED) of three different zones located at 8, 20 and 25″ from IRS2, show that the peak of the SED shifts towards longer wavelengths, when moving away from the star. Adopting the stellar radiation field for these three positions, DUSTEM model fits to these SEDs yield a dust-to-gas mass ratio in the ionized gas similar to that in the diffuse ISM. However, the ratio of the IR-to-UV opacity of the dust in the ionized shell is increased by a factor ≃3 compared to the diffuse ISM.

2.1 Introduction

At early stages of their lives, massive stars are deeply embedded in their native clouds. These stars process their environment with energetic radiation and stellar winds, creating HII regions and stellar wind driven bubbles (Weaver et al., 1977). Overpressure of these regions drives their expansion into the molecular cloud and the HII region changes from hypercompact to ultracompact to compact. Eventually, the ionized gas breaks out, creating a so-called *champagne flow* that disperses the molecular cloud. The interaction between massive stars and their natal cloud controls the star formation process by compressing gas clumps through shocks – triggering subsequent star formation –, photo-ionizing and photoevaporating envelopes around low mass protostars in the cluster – creating prominent globules, fingers, and proplyds – and dispersing gas in ionized and neutral gas flows. This evolution of the region is accompanied by a processing of the cloud material. Specifically, dust coagulates and this has major influence on the absorption properties (Ossenkopf and Henning, 1994; Ormel et al., 2011).

The radiation from the powering massive stars is absorbed by the surrounding gas and dust cloud. Only long wavelength (mid-IR to cm) emission from the ionized gas, dust grains, and molecules, and molecular emission can escape and be used to study the properties of the newly formed stars and the early evolution of the region. In the 3-20 μm region, strong and broad emission features at 3.3, 6.2, 7.7, 8.6 and 11.3 μm dominate the spectra (Peeters et al., 2002) due to Polycyclic Aromatic Hydrocarbons (PAHs) molecules (Tielens, 2008). These broad emission features are perched on a mid-IR continuum due to transiently heated very small grains (VSG) whose nature is not well understood. At longer wavelengths ($\sim$30 μm), emission by big grains (BG) – in radiative equilibrium with the radiation field – take over (Desert et al., 1990). Each of these emission components has been "calibrated" as a star formation rate indicators on regions of star formation in nearby galaxies (Calzetti et al., 2007) but these empirical validations have no general theoretical underpinning.

Here, we present mid-IR observations of the deeply embedded OB star cluster in the W3 main region obtained by FORCAST on SOFIA in order to understand the interrelationship of the different mid-IR emission components, their carriers and their evolution in regions of massive star formation. W3 main is a star formation region located towards the Perseus arm at a distance of 1.95 ± 0.04 kpc, accurately measured using maser kinematics (Xu et al., 2006; Hachisuka et al., 2006). Infrared and radio observations have detected a number of bright sources in the W3 main cloud Harris and Wynn-Williams (1976); Wynn-Williams et al. (1972); Tieftrunk et al. (1997). These objects span a range in evolutionary history with deeply embedded protostars, ultracompact & compact HII regions, all associated with a newly forming cluster containing

some 15 OB stars (Ojha et al., 2004; Bik et al., 2012). A large, embedded population of intermediate- to low-mass stars coexists with the OB stars (Megeath et al., 1996). In this paper we focus on W3A, a shell-like compact HII region, powered by IRS2, a 2-3 Myr old O6.5V star (Ojha et al., 2004; Bik et al., 2012) that provides a classic example of a wind driven bubble HII region in an early stage.

2.2 Observations and data

W3 main was observed by SOFIA during the Short Science flight series on December 4 and 8, 2010, at an altitude of ∼43000 feet. We acquired images at 6.4, 6.6, and 7.7 microns in single channel mode and 19.7, 24.2, 31.4, and 37.1 microns using the dichroic beamsplitter in dual channel mode. The field of view of the instrument is the same for all the images, $\sim 3.4' \times 3.2'$, and the pixel size is $0.768''$. The point spread function has a FWHM of $2.8''$ at wavelengths up to 20 μm and is diffraction limited at the longer wavelengths filters (Herter et al., 2012). We used a chop throw of $\sim 5'$ and a chop frequency of ∼5 Hz. The integration time for each chop pair was ∼30 s. The data were processed and calibrated using the pipeline described in Herter et al. (2012). The processed images were aligned and averaged using an iterative sigma rejection algorithm to produce images with effective integration times of 150 s for 6.4 and 6.6 μm, 270 s for 7.7 μm, 240 s for 19.7 μm, 150 s for 24.2 and 31.4 μm, and 330 s for 37 μm. The scale size and orientation of the resulting images have been checked against Spitzer IRAC images (Ruch et al., 2007) and agree well. The estimated 3σ uncertainty in the calibration due to variations in flat field, water vapor burden, and altitude is approximately ±20%. A false color image of the whole W3 main region is shown in Figure 2.1 and a zoom in on W3A is presented in Figure 2.2a.

The FORCAST photometry was checked against the W3-IRS5 spectrum obtained by the Short Wavelength Spectrometer (SWS) on board of the Infrared Space Observatory (ISO) (Boogert et al., 2008). W3 IRS5 is a point source in our images and is isolated even within the large SWS beam. At all wavelengths, the two agree to within the absolute calibration error of 20%. W3A was also observed with SWS/ISO (Peeters et al., 2002). We integrated the emission over the FORCAST filters in the relevant apertures of the SWS spectrum, and found an excellent agreement in flux (∼20%) at all wavelengths except for the 6.4 μm band where the FORCAST flux is a factor 1.9 larger. Given that SWS calibration of extended sources is quite challenging, we deem this agreement excellent. Strong [SIII] and [NeIII] lines are present in the SWS spectrum, but the flux contribution of these lines to the FORCAST 19.7, 31.5 and 37.1 bandpasses is less than 6%. We show cross cuts towards the North in the

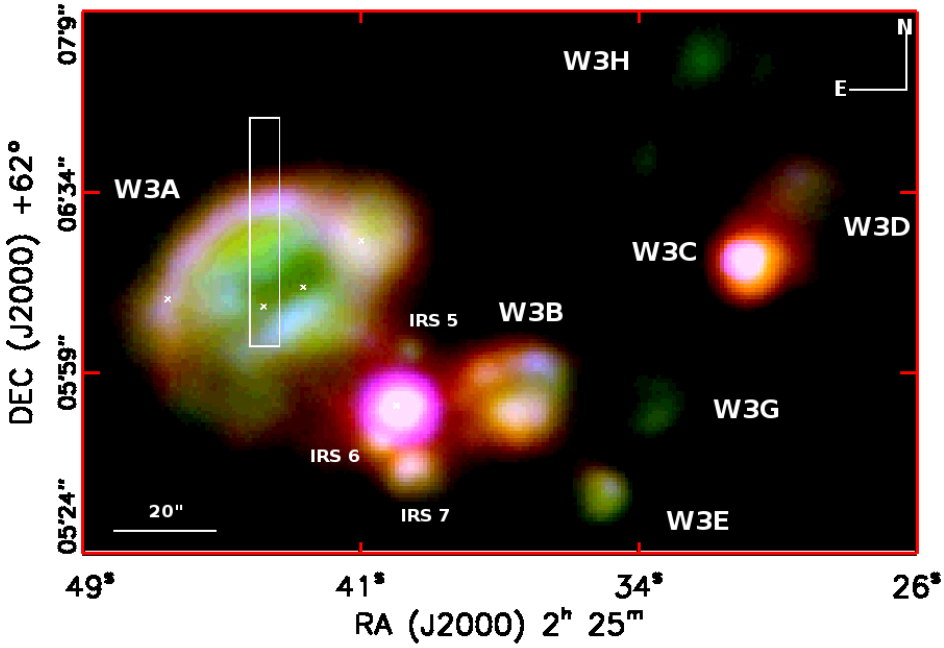

Figure 2.1: Color image of W3 main region, colors are: blue 7.7 μm, green 19.7 μm, and red 37.1 μm. Sources have been identified following Wynn-Williams et al. (1972) and Tieftrunk et al. (1997). The location of the four embedded OB stars in W3A are indicated by crosses and are IRS2c, IRS2, IRS2a, and IRS2b (left to right). The rectangular box indicates the direction of the cross cut for which the photometry is shown in Figure 2.3.

different FORCAST images in Figure 2.3.

W3A was also observed with ISOCAM-CVF. We use the Highly Processed Data Products (HPDP) from the ISO archive (Boulanger et al., 2005). Comparison shows that the FORCAST fluxes, $F_{6.4}$ and $F_{7.7}$, are dominated by the PAH 6.2 μm and 7.7 μm features and the $F_{6.6}$ traces the underlying plateau (Peeters et al., 2002). By subtracting the $F_{6.6}$ contribution from the $F_{6.4}$ and $F_{7.7}$ bandpasses, we derive the "pure" PAH emission.

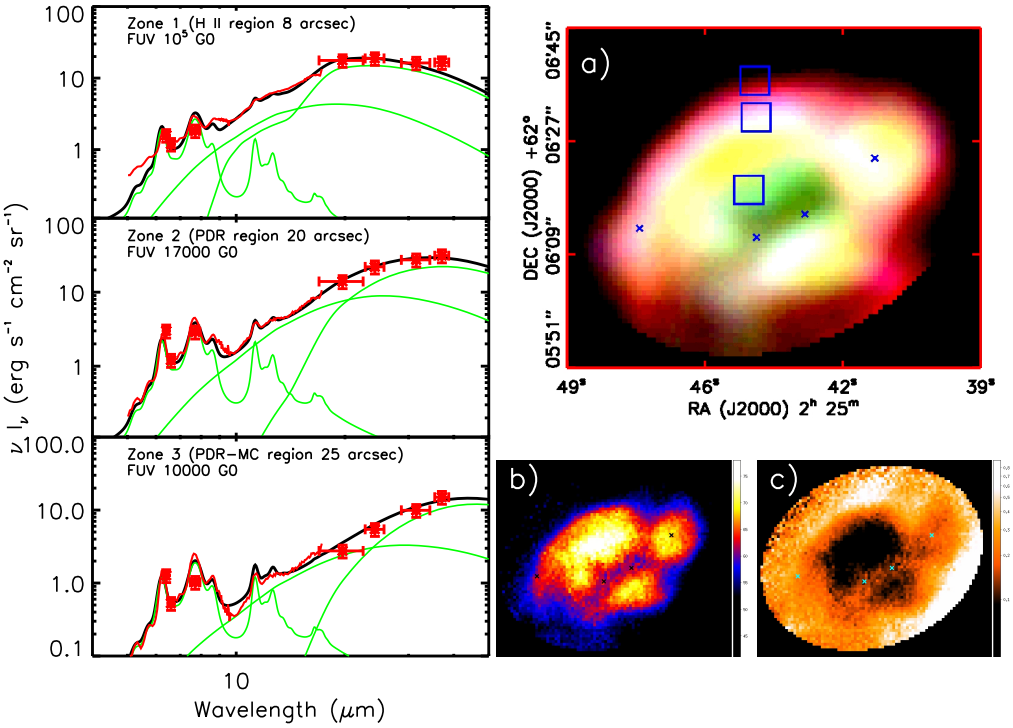

Figure 2.2: *Left*: Spectral Energy Distributions derived from the FORCAST observations (red crosses) and ISOCAM-CVF spectra (red line) in the three positions marked with squares in 2a. For a clearer comparison, the contributions from the ionized gas emission lines have been subtracted from the CVF spectra. Best fit DUSTEM models are shown as black lines. The green lines show the separate contributions from PAH molecules, Very Small Grains, and Big Grains (peaking left to right). *Right*: a) False color image of the W3A compact HII region. The three squares indicate three positions where spectral energy distributions have been obtained, and crosses mark the position of IRS2c, IRS2, IRS2a and IRS2b from left to right. b) Color temperature map, the peak in emission is located at the north of IRS2 (section 3.1). c) Optical depth map at 37.1 μm.

2.3 Results

2.3.1 Observational analysis of W3A

Figure 2.1 shows a false color image of W3 main, combining three mid-infrared bands tracing the PAHs and warm dust. All the well-known, bright infrared and radio sources are visible in the map, including the deeply embedded protostars associated with W3 IRS5, the ultracompact HII regions W3B, W3C, and W3E,

and the compact HII regions, W3A, W3B, W3D, and W3H. In all, some 10 regions powered by bright O or early B stars are discernible in the mid-infrared. The W3 OB cluster of sources is embedded in low-level PAH emission in the deep 8 μm IRAC images. However, rather than UV photons leaking out of the confines of the (ultra)compact sources, this emission may be powered by distributed B stars in a more extended cluster, postulated on the basis of the extended [CII] 157 μm emission (Howe et al., 1991).

In the radio, the compact HII region, W3A, shows a clear shell-like structure to the north (Wynn-Williams et al., 1972; Tieftrunk et al., 1997). At mid-IR wavelengths, W3A shows a very similar structure (Fig. 2.2) and the $F_{19.4}$, $F_{24.2}$ brightness distribution tracks the radio emission well (cf. Figure 2.3). W3A seem to be a classic example of a wind-driven bubble expanding and sweeping up the surrounding cloud material (Weaver et al., 1977). The radio emission and the $F_{19.4}$ and $F_{24.2}$ warm dust emission originate from the swept up dense ionized gas. This shell is surrounded by a dense PDR (at $\sim$20$''$ from IRS 2) traced by the PAH emission (Figure 2.3). The sharpness and the large relative variations of the PAH emission implies that the PDR is very thin ($\sim$1$''$; 0.01 pc) and unresolved. The shell-like structure of this region produces strong limb-brightening and the residual $F_{19.4}$, $F_{24.2}$ emission inside the cavity and the PAH emission seen within the ionized zone reflect this geometry. The inner cavity is presumably filled with hot gas and devoid of dust. However, there is no evidence for X-ray emission from the gas (Hofner et al., 2002) possibly due to the effect of mass loading from embedded clumps (Redman et al., 1998). We deem the alternative model – "leakage" of the hot gas into the surroundings (Harper-Clark and Murray, 2009) – less likely in view of the thin, dense shell enwrapping the ionized shell in the IR images.

We used the $F_{31.5}$ to $F_{37.1}$ flux ratio to derive color dust temperatures (T_{Dust}) and optical depths at 37 μm (τ_{37}), assuming a modified black body for the dust ($\kappa_d \sim \nu^{\beta}$ with $\beta = 1.8$; Planck Collaboration et al. 2014). Total dust column density maps have been derived from τ_{37} using the extinction curve taken from Draine (2003) with $R_V = 4$ (Fig. 2.2). Results are summarized in Table 1. For $R_V = 3.1$ (5), the column density decreases (increases) by a factor of 0.92 (1.1). Color temperatures and optical depths derived using different filter combinations show substantially the same global structure but the absolute values increase by 20% ($F_{24.2}$-$F_{37.1}$) and 30% ($F_{19.4}$-$F_{24.2}$). We prefer the $F_{31.5}$-$F_{37.1}$ color combination because this emission is expected to originate from the same dust population (i.e. BG; cf., Figure 2.2). We note that T_{Dust} peaks at the ionized gas shell rather than at the IRS2 position, which likely reflects an increase in the relative importance of emission by the cold-dust in the PDR as compared to the warm-dust in the ionized-shell for sightlines traversing the cavity (see section 2.3.3).

The 6.2 and 7.7 μm PAH emission and the 19-24 μm emission observed

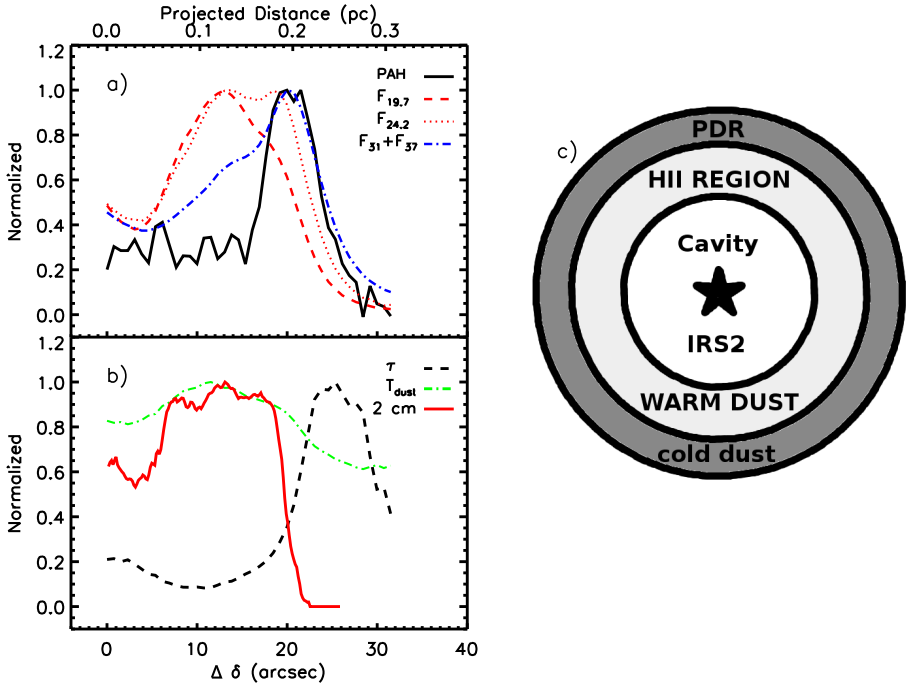

Figure 2.3: a) Cross cuts along the rectangle in Figure 2.1 as a function of projected distance from IRS2. All values have been normalized to the maximum along the cross cut. $F_{6.4}^{line} + F_{7.7}^{line}$ (black); $F_{19.7}$, $F_{24.2}$ (red); $F_{31.5} + F_{37.1}$ (blue). b) Derived color temperature and optical depth at 37μm(see text for details), along with the 2 cm emission from Tieftrunk et al. (1997). c) Schematic plot of W3A, the relative emission from the PDR increases as line of sights are further away from IRS2.

in W3A are associated with the neutral PDR and ionized gas, respectively. It is well established that the PAH emission in compact HII regions peaks in the PDR (Tielens et al., 1993; Berné et al., 2009). The Spitzer/MIPSGAL & GLIMPSE surveys have shown that many HII regions present bright MIPS 24 μm emission associated with the ionized gas and are surrounded by a shell of bright 8 μm PAH emission (Anderson et al., 2011; Carey et al., 2009). With this in mind, we recognize that the star W3 IRS2b is also surrounded by a shell of PAH emission (Figure 2.2) while bright 19 & 24 μm emission is present in the ionized gas. We thus surmise that this star is still embedded in its own HII region, separate from W3A. Perusal of JHK images of W3A (Bik et al., 2012) also suggests that the emission from IRS2b is separate from that of the main HII region. IRS2 has already "swallowed" the HII region associated with

IRS2a and IRS2c and likely the region around IRS2b is next on the menu. We consider that the ridge of bright emission towards the south of IRS2a is still a remnant of the earlier, isolated HII regions phase of this star.

From the FORCAST data, the region associated with IRS2b (O8V) has a $6-40$ μm luminosity of 1×10^5 $L_\odot$ in good agreement with the estimate based on near-IR photometry and spectroscopy (Bik et al., 2012). The whole W3A region has a $6-40$ μm luminosity of 4.1×10^5 $L_\odot$. Subtracting IRS2b, the observed $6-40$ μm luminosity of W3A is $\sim 3 \times 10^5$ $L_\odot$. Based on the spectral type of Bik et al. (2012), and using Martins et al. (2005), we estimate that IRS2 (O6.5V), IRS2a (O8.5V), and IRS2c (B0.5V) emit 1.6×10^5 $L_\odot$, 6.6×10^4 $L_\odot$, and 4×10^4 $L_\odot$, respectively. The total luminosity of the stars associated with W3A is thus $\sim 3 \times 10^5$ $L_\odot$. We note that the FORCAST-derived luminosity is just a lower limit to the total infrared luminosity, because far-IR photometry is lacking. Nevertheless, it seems that the luminosity of the known OB stars is sufficient to explain the observations and no major contribution from embedded YSOs is required, consistent with Ojha et al. (2004). The $6-40$ μm luminosity associated with the ionized gas shell is 1.1×10^5 $L_\odot$. Hence, we estimate that the (radial) UV (absorption) optical depth of the dust in the ionized gas is, $\tau_{UV} = -\ln(L_{6-40}/L_\star) \simeq 1$.

2.3.2 Dust Spectral Energy Distribution

2.3.3 Lyman alpha dust heating

The dust temperature peaks on the ionized gas shell and this is very reminiscent of Lyα heating. From the radio observations (Tieftrunk et al., 1997), we derive the Lyα luminosity of $3.2 \times 10^4 L_\odot$ or only 30% of the observed $6-40$ μm luminosity associated with the ionized gas shell. In general, the contribution of trapped Lyα photons to the dust heating (Γ_α) relative to the stellar radiation ($\Gamma_\star$), is approximately given by $\Gamma_\alpha/\Gamma_\star = (r/R_S)^2 \times 1/\tau_{UV}$ (Tielens, 2005) with r the distance from the star (0.12 pc), R_S the Strömgren radius of the region (0.2 pc) and $\tau_{UV} \sim 1$ the radial optical depth of the dust (see above). In the middle of the ionized gas shell, Lyα heating contributes $\sim$25% of the dust heating.

We used Cloudy version 10.00 (Ferland et al., 1998) to model the W3A T_{Dust} distribution and study the heating due to trapped Lyα photons. Assuming an O6 star with a luminosity of $2 \times 10^5 L_\odot$, and a shell density of 5000 cm^{-3}, the model shows that only for $\tau_{UV} \lesssim 0.2$ (a factor of 5 less than observed) dust heating is dominated by Lyα and the temperature distribution tracks the density structure. Hence, both the observed luminosity and the observed optical depth imply that stellar radiation dominates the temperature distribution. We attribute the rather constant dust temperature in the ionized shell to the

morphology of the region. Specifically, the absence of a rise of the dust temperature towards the central star reflects the presence of an inner dust-free cavity. The geometry of a dust-free cavity, surrounded by a dusty ionized gas shell and PDR (Figure 2.3b), will tend to give a rather constant color temperature with projected distance from the star, because the observed SED is a superposition of all emission components (ionized shell & PDR) along the line of sight.

2.3.4 Dust-to-gas ratio

The H-nuclei column density was calculated from the radio (Tieftrunk et al., 1997), assuming a shell-like geometry, to be $N_H = 7.8 \times 10^{21}$ cm^{-2}. The dust column density derived with DUSTEM results then in a dust-to-gas mass ratio of 0.012, close to the diffuse ISM value. If we adopt the UV optical depth derived from the observed $6 - 40$ μm dust luminosity in the ionized gas and allow for the geometry, and adopt the Draine (2003) $R_V = 4.0$ dust model, we arrive at a dust-to-gas mass ratio which is higher, 0.035. While this difference seems small, we consider it significant. To phrase this differently, adopting dust properties appropriate for the diffuse ISM, the radial absorption optical depth by dust in the ionized gas would be $\simeq$4 and only $\simeq$0.02 of the number of ionizing photons emitted by the central star would be used to ionize the gas (Petrosian et al., 1972). This would imply an enormous ionizing photon luminosity that is incompatible with the observed properties of the ionizing stars in this HII region and the observed IR luminosity of the dust. This is a well-known issue, dating back to the earliest IR studies of HII regions (Tielens and de Jong, 1979), and it seems that the dust properties in the ionized gas have to be different from those in the diffuse ISM. This difference may reflect an increase of dust size and concomitant decrease in the UV extinction cross section during the preceding molecular cloud core phase driven by coagulation (Ossenkopf and Henning, 1994; Ormel et al., 2011).

Chapter 3

The Orion HII region and the Orion Bar in the Mid-Infrared

Based on: Salgado, F. et al. 2015

Abstract

We present mid-infrared photometry of the Orion Bar obtained with FORCAST aboard SOFIA at 6.4, 6.6, 7.7, 19.7, 31.5 and 37.1 μm. By complementing this observations with archival FORCAST and Herschel*/PACS images we are able to construct a complete infrared spectral energy distribution of the Huygens region in the Orion nebula. The FORCAST images show a complex structure and, in order to disentangle the different components of dust, we compare the infrared images with gas tracers. We find that PACS maps trace the molecular cloud, while the mid-infrared FORCAST data trace the photodissociation region (PDR) and HII region. Analysis of the energetics of the region reveal that the PDR extends for 0.28 pc along the line-of-sight and that the Bar is inclined at an angle of 4°. The infrared and submillimeter images reveal that the Orion Bar represents a swept up shell with a thickness of 0.1 pc, bounded on one side by the ionization front and on the other side, likely, by a shock front. The mass of the swept up shell implies a shock velocity of $\simeq 3$ km/s and an age of $\simeq 10^5$ yr for the HII region. We analyze the dust spatial distribution and dust properties in the ionized gas and the PDR. Our analysis shows that the UV and infrared dust opacities in the HII region and the PDR differ from that in the interstellar medium (ISM), being a factor 5 to 10 lower than the diffuse interstellar medium. In the ionized gas, Lyα photons are a major source of dust heating at distances larger than $\simeq 0.06$ pc from θ^1 Ori C, the main ionizing star. Dust temperatures can be explained if the size of the grains is between 0.1 to 1 μm. We attribute the differences in the properties of the dust to coagulation during the cold core phase before the formation of the stars. We derive the photo-electric heating efficiency of the atomic gas in the Orion Bar from the measured far-infrared fine-structure lines and the observed infrared continuum emission. The photo-electric efficiency increases with depth into the PDR. The results are in good qualitative agreement with models. The quantitative differences may indicate a decreased PAH abundance in this region.*

3.1 Introduction

Dust grains are an important constituent of the interstellar medium (ISM) of galaxies. From young stellar objects (YSOs) to active galactic nuclei (AGN), most of the objects in the Universe show the presence of dust either in emission or absorption. Moreover, dust plays a key role in star and planet formation, molecule formation due to surface chemical reactions and heating of the gas due to the photoelectric effect. In addition, dust emission provides a convenient tracer of star formation in galaxies (e.g. Calzetti et al. 2007, 2010).

There is a consensus that dust grains are mainly composed of two chemically different type of species: silicates and carbonaceous materials (Zubko et al., 2004; Draine and Li, 2007). The former being the most abundant in mass for large grains, and the latter being the dominant species for smaller grains. At the lower end of the size distribution of grains, large molecules known as polycyclic aromatic hydrocarbons (PAH), formed by carbon rings, produce emission in characteristic infrared bands from 3 to 20 μm (Tielens, 2008). While the general properties of the dust grains in the diffuse ISM have been well studied, dust grain properties are expected to change with the environment (Henning, 2010). In particular, according to extinction measurements towards different lines of sight in the Galaxy (Cardelli et al., 1989), it is well established that properties of dust change in the Galaxy. Several studies such as Stepnik et al. (2003) have also demonstrated variations in the dust size distribution and in the abundance usually measured as the gas to dust ratio. Finally, recently, the Planck survey has identified systematic variations in the submillimeter characteristics of interstellar dust, pointing towards the importance of dust evolution in the ISM (Planck Collaboration et al., 2014).

The extreme environments of regions of massive star formation may, in particular, be very conducive to dust processing. The study of dust around massive star forming regions has been of major interest since the beginning of modern infrared and radio studies. In recent years, the study of dust in HII regions has increased; mostly driven by the increase of observations at infrared wavelengths due to *Spitzer*, *Herschel* and most recently the Space Observatory for Infrared Astronomy (SOFIA). Deharveng et al. (2010), Anderson et al. (2012), Paladini et al. (2012) and Pellegrini et al. (2009) have studied the properties of dust in large evolved HII regions using combined datasets from *Spitzer*, *Herschel* and APEX. While Arab et al. (2012) and Salgado et al. (2012) have revealed the importance of dust variations in individual HII regions. Most of the data covered the far-infrared/sub-mm, as – until recently – *Spitzer*/MIPS was the only instrument but with limited angular resolution ($6''$) at mid-infrared wavelengths. Now that SOFIA is in operations, moderate spatial resolution (3–$3.6''$, depending on the wavelength) studies of dust emission from HII regions have come in reach. First results have been published on dusty HII regions

Salgado et al. (2012); Hirsch et al. (2012); Lau et al. (2013, 2014). Here, we analyze data from the Faint Object infraRed Camera for the SOFIA Telescope (FORCAST) of the prototypical HII region, Orion (M42), from Shuping et al. (2012) more deeply to determine the characteristics of dust associated with the ionized gas and in the neutral PhotoDissociation Region (PDR).

The Orion Nebula (M42, NGC1976) is the closest (414 pc, Menten et al. 2007) and the most extensively studied region of massive star formation in the Galaxy. The overall structure of the Orion nebula has been well studied at visible wavelengths (O'dell, 2001; O'Dell et al., 2008; O'Dell and Harris, 2010). In the center of the nebula, four young massive stars known as the Trapezium have photoionized the surrounding gas creating an HII region; the global ionization structure is dominated by the most massive of the four stars, θ^1 Ori C (spectral type ∼O7-O5V, Stahl et al. 2008; Kraus et al. 2007). The HII region is partially confined in a concave structure open towards the line of sight of the observer. A thin (0.05 pc) and dense ($\sim 10^5$ cm^{-3}) PDR is located between the background molecular cloud and the ionized gas. Due to the difference in pressure between the PDR and the ionized gas, material flows towards θ^1 Ori C (O'dell and Bally, 1999; O'dell, 2001). At approximately $2'$ southeast of the Trapezium the ionization front changes into an almost edge-on geometry producing the Orion Bar feature, the prototypical PDR (Tielens et al., 1993; Hollenbach and Tielens, 1997). While several HII/PDR/molecular clouds have been studied, Orion is still a cornerstone in understanding the interaction of newly formed massive stars with the surrounding gas and dust.

Previous ground based studies of Orion in the mid-infrared regime have focused on the active star forming core, including the BN/KL object, and the region close to the Trapezium (Shuping et al., 2004; Robberto et al., 2005; Smith et al., 2005). These studies show a rich and complex structure, with diffuse extended emission, arcs, streaks and emission associated with proplyds. In addition, ground-based and space-based studies on the spatial variations of the unidentified infrared (UIR) bands – generally attributed to Polycyclic Aromatic Hydrocarbon molecules – have been reported by Cesarsky et al. (2000); Kassis et al. (2006); Galliano et al. (2008); Haraguchi et al. (2012). Recently, Arab et al. (2012) studied the far-infrared emission of Orion using *Herschel*/PACS and SPIRE photometry. They compared *Spitzer* and *Herschel* data and found a shift in distance between the Orion Bar as seen by *Herschel* and the IRAC 8 μm emission. Here, we will combine this data with the mid-infrared observations of the Orion HII region obtained by the FORCAST instrument (Herter et al., 2012) on board of Stratospheric Observatory for Infrared Astronomy (SOFIA).

In Section 3.2, we provide a description of the new FORCAST observations, as well as a summary for optical, infrared and submillimeter data from the literature used here. In Section 3.3, we give a description of the FORCAST images by comparing them with gas tracers. Together with *Herschel*/PACS

far-infrared photometry, we construct spectral energy distributions (SED). The SEDs are further analyzed by using a two component modified blackbody model. In Section 3.4, the parameters derived from the SED fit are used to study the geometry of the Orion Bar and the properties of the dust grains in the ionized gas and the photodissociation region (PDR). In Section 3.5, we provide an explanation for the observed temperature of the dust in the ionized gas, as well as for the dust properties observed in Orion. We compare our results with previous works from the literature putting our results in the broader context of HII region evolution. Finally, in Section 3.6, we summarize our work and provide the conclusions.

3.2 Observations and Data

Two sets of observations were obtained by FORCAST on board of SOFIA during the Short Science flight series: the first one is centered in the Trapezium stars and has been presented in Shuping et al. (2012), with a field of view (FOV) of roughly $3' \times 3'$ the images cover most of the HII region in the center of Huygens nebula (Figure 3.1). The second set of images are centered in the Orion Bar with a similar FOV (Figure 3.1). The observations were made using FORCAST (Herter et al., 2012) on the 2.5 m telescope aboard SOFIA. FORCAST is a 256×256 pixel dual-channel, wide-field mid-infrared camera sensitive from 5 to 40 μm with a plate scale of $0.768''$/pixel and field of view of $3.4 \times 3.2'$. The two channels consist of a short wavelength camera (SWC) operating from 5 to 25 μm and a long wavelength camera (LWC) operating from 28 to 40 μm. An internal dichroic beam-splitter enables simultaneous observation from both long and short wavelength cameras. A series of band pass filters are used to image at selected wavelengths.

The Orion Bar data was taken over three flights: 01-Dec-2010, 04-Dec-2010 and 08-Dec-2010 with FORCAST. Dichroic mode was used to simultaneously observe in a number of filters: 19.7/31.4, 19.7/37.1, 7.7/37.1, 6.6/37.1, and 11.3/37.1. Direct (single channel) mode was also employed for filters: 6.4, 6.6, 7.7, 11.3 and 37.1 microns. A southern region of the Orion Bar was also observed in the dichroic mode with the 19.7/31.4 and 19.7/37.1 pairs. Data were reduced and calibrated as discussed in Herter et al. (2013).

A small rotation is seen in our Orion Bar centered data for the 7.7 and the 31.7 μm images, when comparing to the Trapezium centered images. Since no obvious point sources are detected in most of our images, another procedure must be performed to correct for this effect. At each wavelength the images are rotated in discrete steps of 0.1° from -4° to 4° and, by using a normalized cross-correlation estimator, a best expected rotation angle is obtained. The process was performed for all of our images, but only for the 7.7 and 31.7 μm images

is the rotation significant (2°). We checked the astrometry of our data after the correction is applied by comparing the 7.7 μm to the 8 μm *Spitzer*/IRAC image and the agreement is good to within about 1″. Finally, the images were combined by averaging the flux in the region of overlap and scaling the full images accordingly.

We checked the relative flux calibration of the FORCAST images by comparing them with ISOCAM-LWS spectra (Cesarsky et al., 2000). The agreement is good in all bands. Using the ISOCAM-LWS spectra we estimate the contribution from the [S III] 18.7 line to the 19.7 flux to be less than 10 % at the ISOCAM-LWS positions.

Images from the PACS instrument (Poglitsch et al., 2010) on board of the *Herschel Space Observatory* (Pilbratt et al., 2010) at 70 μm and 160 μm were obtained by Abergel et al. (2010) as a part of the "Evolution of interstellar dust" key program and have been presented in Arab et al. (2012). Centered at the Orion Bar and with a FOV of about 14×15′ the images overlap with our FORCAST images. Including the *Herschel*/PACS images allows us to analyze the full dust spectral energy distribution (SED) at infrared wavelengths. The spatial resolution of the images is 5.6″ and 11.3″ at 70 μm and 160 μm, respectively.

Spectral cubes of infrared cooling lines [O I] at 63 μm 145 μm and [C II] at 157 μm were observed by PACS and were published by Bernard-Salas et al. (2012). The spatial resolution of this data changes with wavelength being 4.5″ at 63 μm 10″ at 145 μm and 11″ at 157 μm. The FOV is smaller than our FORCAST images overlapping only in the Orion Bar.

Since the mid-infrared and far-infrared emission probes the dust emission, we complement our dataset with low-resolution (10 Å FWHM) optical spectroscopy from the Postdam MultiAperture Spectrograph (PMAS) in the PPAK mode at the 3.5m telescope in Calar Alto Observatory (Sánchez et al., 2007). The data set consists of ∼8000 spectra in the 3700-7000 Å range, centered in the Trapezium stars and covering 5′×5′. Although the data was taken under non-photometric conditions, the spatial resolution is good enough for a spatial comparison with our infrared data. The astrometry was cross calibrated by comparing the data with Hubble Space Telescope images observed with WFPC.

We extracted the integrated flux and peak emission for some spectral lines at each pixel position, thus we created 2-D maps for the most important lines that trace gas physical properties such as Hα, Hβ, [S II]λ6716,6731, [O II]λ3727,3729, [O III]λ4363, [O III]λ4959,5007, and the [O I] at 6300Å. In our analysis, we studied the spatial distribution of [O I] as a tracer of the ionization front, we neglect possible contamination due to sky emission.

Rotational transition lines of ^{13}CO and C^{18}O in the $J = 3 \rightarrow 2$ transition were observed by the James Clerck Maxwell Telescope (JCMT) using HAARP/ACSIS, published by Buckle et al. (2012). The resolution is close to

15″ and the field of view (FOV) overlaps with our dataset.

Simón-Díaz et al. (2006) studied the spectra of eight stars including θ^1 Ori C. They determined a $T_{eff} = 39000 \pm 1000$ K and a log $g = 4.1$ corresponding to an O5.5V-O6V star in the scale of Martins et al. (2005). By interpolating the values of Table 1 in Martins et al. (2005), we derived a stellar luminosity $L = 2.23 \times 10^5$ $L_\odot$ and number of ionizing photons $N_{ion} = 1.06 \times 10^{49}$ s^{-1}. The second most massive star is θ^1 Ori D a B0.5V star Simón-Díaz et al. (2006), but with an effective temperature more similar to an O9 star. The star θ^1 Ori A is a B0.5 star. Using the values for the stars we obtain a total FUV luminosity in the range $1.4 - 2.7 \times 10^5$ $L_\odot$. The properties of the Trapezium stars are summarized in Table 3.2.

3.3 Analysis

3.3.1 An Overall View of the Orion Nebula

The Orion Nebula is one of the most studied massive star forming regions. At optical wavelengths, the gas in the Orion Nebula shows a complex structure (e.g. Doi et al. 2004) In addition to stars, diffuse emission, the ionization front, as well as proplyds and jets have been thoroughly studied. As can be seen in Figures 3.1 and 3.2, the FORCAST mid-infrared images show an intricate morphology that changes with wavelength. In particular, the 6.4, 6.6 and 7.7 μm images (PAH images) show the Orion Bar, the Trapezium stars and the Ney-Allen nebula. In the 19 μm band, in addition, the Herbig-Haro object HH203, is clearly visible and there is also emission associated with the stars, θ^2 Ori A and θ^2 Ori B. The BN/KL object (North of the Trapezium), the brightest region in the FORCAST images, is saturated in the *Herschel*/PACS bands.

Close to the Trapezium stars and towards the South-West there is bright extended emission in all PAH and mid-infrared images, this emission seems co-spatial with the peak in emission in radio and Hα images (Dicker et al., 2009). South-East of the Trapezium, extended emission and substructure is seen as "filaments", arcs, and "ripples" towards the Orion Bar in all the FORCAST images. We note that this spatial structure is not correlated with the optical extinction maps derived from Hα/Hβ maps (O'Dell and Yusef-Zadeh, 2000; Sánchez et al., 2007), which is consistent with the idea that most of the extinction towards the region is produced by a foreground cloud. Instead, these structures are thought to be perturbations in the surface of the background PDR (Shuping et al., 2012).

The high resolution and large FOV of the FORCAST images together with the large amount of observations from the literature allow us to directly compare the spatial distribution of dust emission with different gas tracers. However, a

close comparison between the IR and optical maps is hampered by the presence of emission associated with the PDR and HH203/204 jets penetrating into the ionized volume. Comparison of the 19.7 and 7.7 μm maps reveals similarity for some spatial structures which we interpret as being associated with the PDR. Nevertheless, several regions bright in 19.7 μm emission do not show up in the 7.7 μm image. Hence, we consider that this part of the 19.7 μm emission is associated with dust in the ionized gas rather than in the background PDR. To bring this out, we have subtracted the 7.7 μm map from the 19.7 μm map scaled to the intensity ratio in the Orion Bar PDR, the result is shown in Figure 3.3. Perusing the velocity dependent Hα maps (Doi et al., 2004), we recognize a resemblance to several structural features in the subtracted 19.7 μm emission with the Hα emission at 8 km s^{-1} (with respect to LSR, Doi et al. 2004) particularly directly North of the Bar. However, not surprisingly, there is no one-to-one correspondence as gas and dust emission processes differ in their density and temperature dependence. Moreover, we also recognize that decoupling of gas and dust seems to be a common phenomena in blister HII regions (Ochsendorf et al., 2014b) and a one-to-one correspondence is not expected.

At longer wavelengths, the PACS images show the Orion Bar as a bright feature, but the brightest emission is associated with the Orion molecular cloud (OMC-1). Note that, unlike the PAH and mid-infrared emission, the region close to the Trapezium stars does not show strong, associated, far-infrared emission in the PACS bands. By comparing the far-infrared with the optical images, the only similarities are found towards the ionization fronts in the direction of the Orion Bar and Orion S.

To further analyze the spatial distribution of the emission, we extracted cross-cuts starting from θ^1 Ori C to deep behind the Orion Bar at the position shown in Figure 3.1. The extracted profiles are shown in Figure 3.4. A general trend is that the dust emission is bright close to the Trapezium and drops with distance up to 0.19 pc where the Orion Bar is prominent (see Section 3.3.2). A closer look reveals the presence of small structures in all the FORCAST bands at 10″, 30″ and 80″, these structures are more prominent at 19.7 μm.

3.3.2 The Orion Bar

All images show a prominent structure to the South-West associated with the well known ionization front, the Orion Bar (Figures 3.1 and 3.2). Yet, there are subtle variations in the maps. Specifically, the position of the peak emission changes with wavelength (Table 3.3). Indeed, comparison of the Hα, [O I] 6300Å, PAHs, H_2 and ^{13}CO emission reveal the layered structure expected for an edge-on PDR (Figure 3.4; Tielens et al. 1993). The dust emission show a similar stratified structure, with shorter wavelengths peaking closer to the

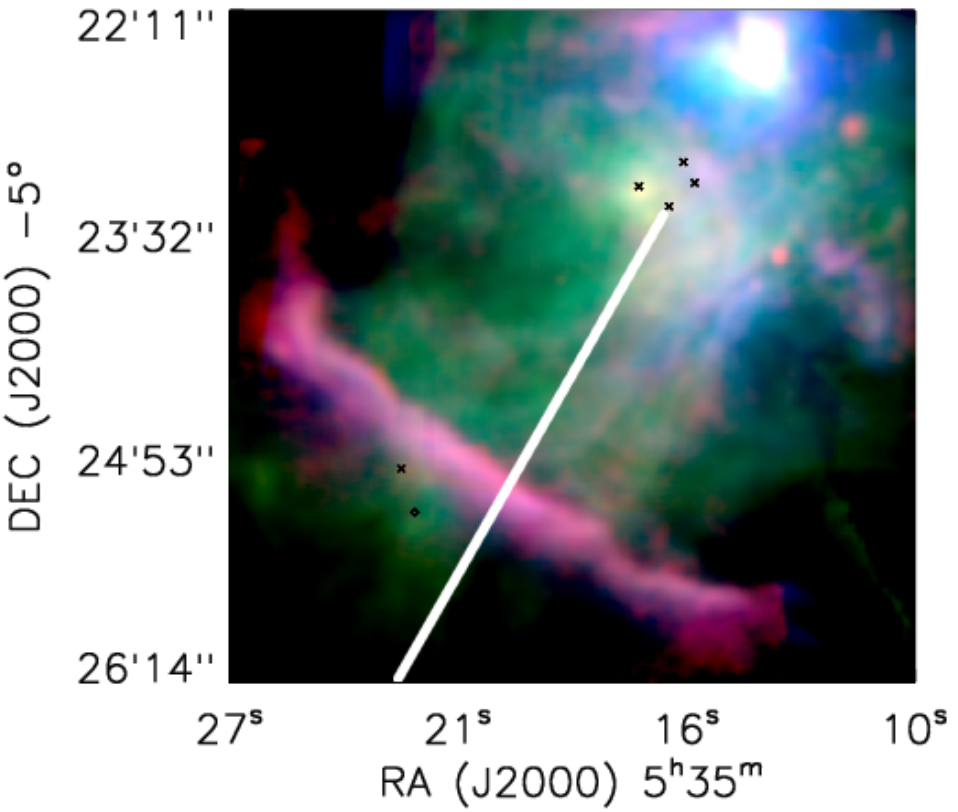

Figure 3.1: False color image for the FORCAST central region (blue 7.7, green 19.7, red 37.1). The Trapezium stars are marked with crosses. The Orion Bar is prominent in the Southeast while the BN/KL region dominates the Northwest (see text for details). The white line show the cross-cut shown in Figure 3.4.

Trapezium stars as compared with longer wavelength images, consistent with heating by the Trapezium stars of an edge-on slab (Werner et al., 1976; Tielens et al., 1993; Arab et al., 2012). The ionization front, as traced by the [O I] 6300 Å profile, show a sharp rise and a "wing-like" decay, but the peak is located closer to θ^1 Ori C at 113″ (0.23 pc). The Hα peak emission is located even closer to θ^1 Ori C at 109″ (0.22 pc). The PAH, 31 μm and 37 μm images show profiles with a sharp rise and a peak at 118″ (0.24 pc). The 19.7 μm image shows, in addition, a separate peak associated with the HII region but there is no clear counterpart in any other ionized optical line. At longer wavelengths, the 70 μm also show a sharp rise at the bar position but the peak is broader than at mid-infrared wavelengths. This broadening trend continues in the 160 μm

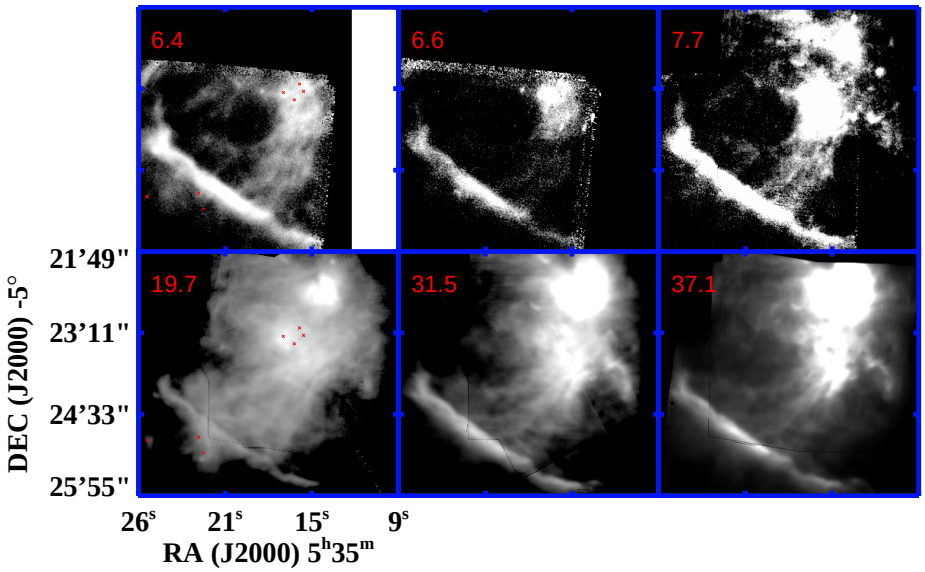

Figure 3.2: The complete data set of FORCAST images at 6.4, 6.6, 7.7, 19.7, 31.5 and 37.1 μm. Red crosses correspond to the Trapezium stars and θ^2 Ori A and θ^2 Ori B. The diamond marks the location of HH 203/204.

data. The 160 μm and ^{13}CO show a broader "gaussian-like" profile with peaks at 135″ (0.27 pc) and 138″ (0.28 pc), respectively. At 450 μm, the peak of the emission has shifted inwards and occurs at the ^{13}CO peak[1]. The ground-based 850 μm data, on the other hand, shows an emission peak that encompasses both the mid-infrared and the 450 μm peak (Figure 3.4). The "shoulder" seen in the 850 μm images at distances less than 0.2 pc is, most likely, free-free emission produced in the ionized gas.

Assuming a constant PDR density of 10^5 cm^{-3} (Simon et al., 1997), we can quantify the location of the different emission peaks in terms of the total column density. We locate the surface of the PDR with the emission peak of the PAH features, at 117.5″ from θ^1 Ori C (see Table 3.3). The mid-infrared dust continuum peaks slightly deeper in to the PDR. The 160 μm emission shows a rather broad peak, running from 120″ to 140″, while the sub-millimeter emission peaks at about 140″. For comparison, the ^{13}CO peak is located at a column density of $N_{\rm H} = 12.7 \times 10^{21}$ cm^{-2}, while the peak in

[1]Some negative values were found in the 450 μm image we added a constant to the data.

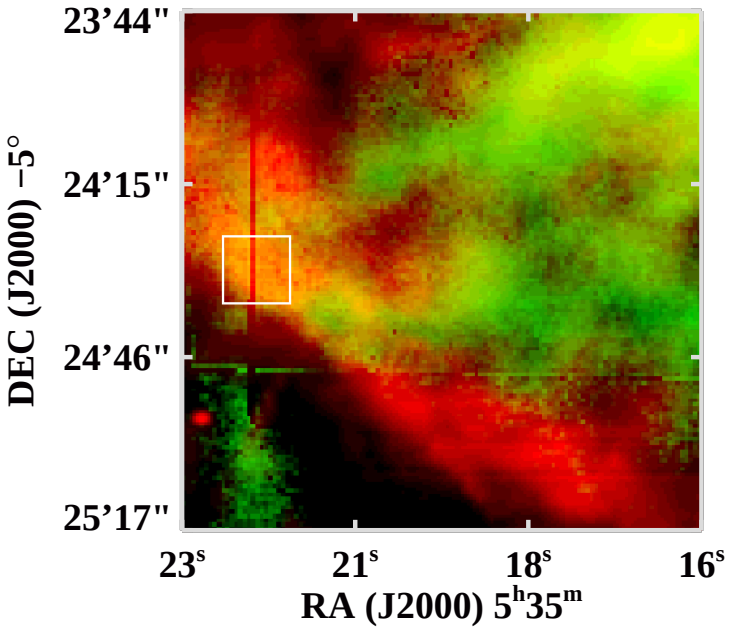

Figure 3.3: A comparison between the 19 μm PDR-subtracted emission (green) and Hα at 8 km/s from (Doi et al., 2004) (red). While there is no one-to-one correspondence between the two images, some features are co-spacial. The white box marks one of the regions where there is correspondence between dust and gas emission.

H_2 emission is located at 20″ from the ionization front, roughly 0.04 pc or at a depth $N_{\rm H} = 7.74 \times 10^{21}$ cm^{-2}. At a distance of 200″ (0.4 pc), the emission in all the bands has dropped to less than 20% of the peak emission at the Bar. The sub-millimeter data conclusively show that the Orion Bar is limited in extent in to the molecular cloud to $\simeq 140''$ or a total column of $N_{\rm H} = 13.9 \times 10^{22}$ cm^{-2}. The Orion Bar is a shell bounded on one side by the ionization front and on the other side (likely) by the shock front running into the molecular cloud.

In neutral regions the cooling is dominated by three forbidden transitions lines: [O I] at 63 μm [C II] at 157 μm and [O I] at 145 μm. The [O I] 63 μm and the [C II] 157 μm line peaks are located at a distance of 125″ (0.25 pc) corresponding to a column density of $N_{\rm H} = 4.65 \times 10^{21}$ cm^{-2}. This is slightly deeper in the Orion Bar than the PAH and mid-infrared emission peaks (Figure 3.4). We also note that clumps seen in the [O I] and [C II] IR lines by Bernard-Salas et al. (2012) are also evident in mid-infrared continuum emission. The [O I] and [C II] structures are, however, located somewhat deeper than clumps

in the dust and PAH emission maps (Figure 3.5).

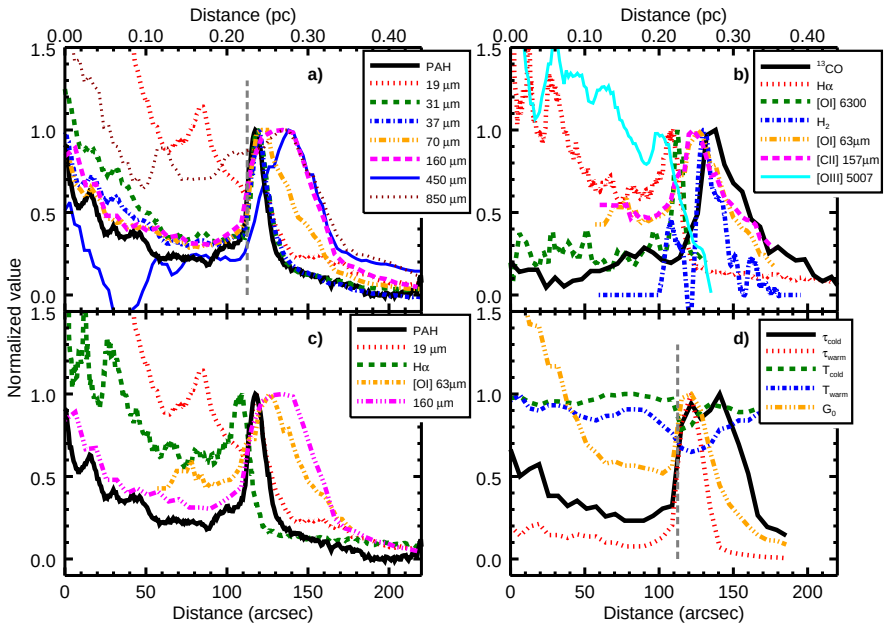

Figure 3.4: Cross cuts of the Orion Bar in different tracers. This diverse data set unveils the onion-skin nature of the PDR. The SOFIA/FORCAST data traces warm dust and PAHs. Optical Hα traces ionized gas while the [O I] at 6300 Å locate the ionization front (shown as a gray-dashed line in the other panels). Molecular gas in the PDR is traced by the ^{13}CO J=3-2 line (Buckle et al., 2012) and the H_2 1-0 S(1) (van der Werf et al., 1996). The extent of the cold dust in the Orion Bar is revealed by the 450 μm and 850 μm JCMT SCUBA data (Johnstone and Bally, 1999).

3.3.3 Spectral Energy Distribution Fitting

The SOFIA/FORCAST data provide, for the first time, full spectral coverage of the SED of the dust emission in the Orion Bar with high angular resolution. In fact, the FORCAST filters are well matched to the peak of the SED, which shifts from about 20 μm to 70 μm over this region. In order to analyze the SED of our images, the FORCAST and the PACS 70 μm images were convolved to the PACS 160 μm resolution assuming a Gaussian PSF and using the values in Table 3.1 for the FWHM. The images were regridded to a common pixel scale of 6.4″, the native resolution of PACS at 160 μm. Figure 3.6 shows SEDs at a few selected positions. The SED peak changes with position from around

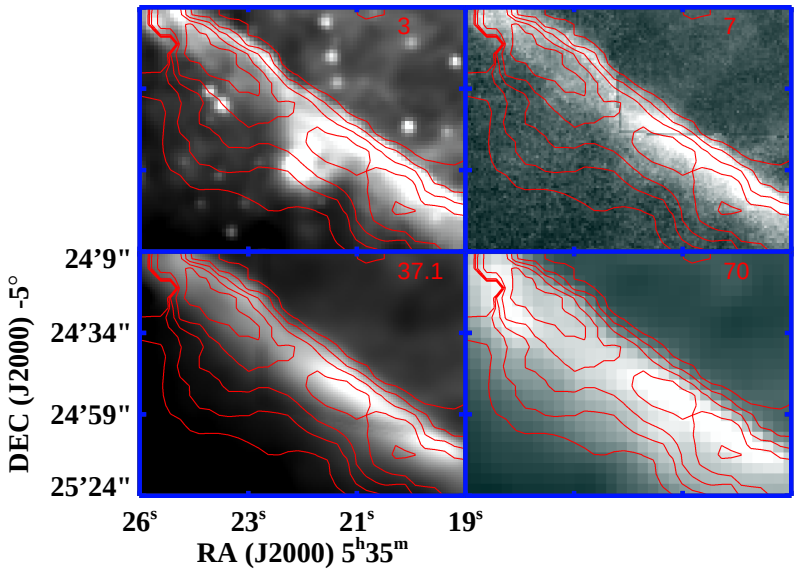

Figure 3.5: *Upper Left Spitzer*/IRAC 3 μm image at the Orion Bar. *Upper Right* FORCAST 7.7 μm image at the Orion Bar. *Lower Left* FORCAST 37.1 μm image at the Orion Bar. *Lower Right* PACS 70 μm image at the Orion Bar. The red contours are the [O I] 63 μm integrated emission, the peak of the line emission is located deeper into the PDR as compared to the dust tracers.

30 μm close to the Trapezium and moving to 80 μm behind the Orion Bar.

Table 3.1: FORCAST and PACS angular resolution

Wavelength (μm)	FWHM ($''$)
6.4	2.9
6.6	3.0
7.7	2.7
19.7	2.9
31.5	3.4
37.1	3.6
70	5.6
160	11.3

The SEDs are very broad and show evidence for two separate components;

Table 3.2: Properties of the central stars (Martins et al., 2005)

Star	Spectral Type	Ionizing photon flux	Total Luminosity log(L/L⊙)	FUV Luminosity log(L/L⊙)
θ^1 Ori A	B0.5V	47.36	4.52	4.61
θ^1 Ori B	B1V	47.06	4.42	—
θ^1 Ori C	O4V-O6V	48.96	5.68-5.31	5.26 (O5.5)
θ^1 Ori D	B0.5V	47.36	4.52	4.61

Table 3.3: Spatial emission peaks

Wavelength/Line (μm)	Distance[1] ($''$)	N_H[5] ($\times 10^{21}$cm^{-2})	Comment
6.4	117.5 ± 0.8[2]	0	PDR surface
6.6	117.5 ± 0.8	0	
7.7	117.5 ± 0.8	0	
19.7	118 ± 0.8	0.31	
31.5	119.5 ± 0.8	1.24	
37.1	120 ± 0.8	1.55	
70	125 ± 3	4.65	
160	135 ± 6	10.8	
450	138 ± 6	12.7	
850	138 ± 6	12.7	
[O I]$_{63}$	125 ± 10	4.65	
[C II]$_{157}$	125 ± 10	4.65	
[O I]$_{6300}$	112.5 ± 3	...	Ionization front
H_α[3]	109 ± 0.2	...	Ionization Bar
H_2[4]	130	7.74	Peak of the 1-0 S(1)
^{13}CO(3-2)[6]	138 ± 6	12.7	Peak of low-J ^{13}CO

particularly beyond the Orion Bar. Indeed, modified blackbody fits to the SEDs at each pixel position with a spectral index $\beta = 1.8$ are not satisfactory. Modified blackbody fits with variable β (between 0 and 3) yield better results in terms of the reduced χ^2. However, the β values are too low ($\beta < 0.5$), far from standard values.

The IR emission observed in the maps results from contribution of grains located within the HII region, in the PDR and in the molecular cloud. When comparing the PACS 160 μm emission with the ^{13}CO data, it is clear that there is a component associated with the Orion molecular cloud (see Figure 3.7). The mid-infrared emission observed by SOFIA/FORCAST and far-infrared emission

from *Herschel*/PACS 70 μm are tracing different components of the dust. This can clearly be seen at positions close to the Orion Bar where the combination of two modified-blackbody function are needed to obtain a good description of the data (see Figure 3.6 for examples of the SEDs and fits). Therefore, we fitted all the data with two modified blackbody components assuming optically thin emission using: $I_\lambda = \tau_{warm} \times B_\lambda(T_{warm}) \times (\lambda/\lambda_0)^{-\beta} + \tau_{cold} \times B_\lambda(T_{cold})(\lambda/\lambda_0)^{-\beta}$, where warm corresponds to $T_{warm} > 70\ K$ and cold to where $T_{cold} < 70\ K$. In order to limit the number of free parameters, we have fixed the exponent of the modified blackbody for both components ($\beta = 1.8$). The constants, τ_{warm} and τ_{cold}, are the optical depth at a given reference wavelength (we adopt $\lambda_0 = 100\ \mu$m).

Dust grains can be either in equilibrium with the radiation field or stochastically heated by photons depending on the size of the grain and the strength of the radiation field. In Orion, due to the strength of the radiation field ($\sim 1 \times 10^5\ G_0$, Section 3.4.1), the emission of dust particles is produced by dust particles in radiative equilibrium with the radiation field, irrespective of their size (except for PAHs). Indeed, small (carbonaceous) dust particles of $\gtrsim 10$ Å in size ($\gtrsim$ 120 C atoms) are expected to be in equilibrium with the radiation field (Draine and Li, 2001, 2007). The steep increase in density (and extinction) at the Orion Bar produces a clear broadening of the SEDs. While large grains remain in equilibrium with the (lower) radiation field, small grains are stochastically heated. Therefore, deeper in the Orion Bar PDR, the warm component is produced by small grains stochastically heated.

Figure 3.8 shows the temperature and optical depth maps for both components at the positions where our fit is reasonably good (reduced $\chi^2 < 3$). Clearly, PACS 160 μm trace a cold dust component, while the FORCAST mid-infrared images trace a warm dust component. The contribution to the PACS 70 μm emission is a combination of both the warm and the cold component (see also Figure 9). The cold dust component reveals a temperature in the 38-44 K range to the East and South-East of the Trapezium. At the Orion Bar the temperature decreases to values of about 33 K. Towards Orion S and Orion BN/KL the temperature is also low. Unfortunately, towards Orion BN/KL the PACS images are saturated and the fit results are not reliable. In terms of the overall structure, the warm component shows a spatial correlation with the ionized gas emission and is fairly uniform (Figure 3.8). An increase in τ_{warm} is seen towards Orion S, the Orion Bar and the BN/KL object. Variations in temperature for the warm component are large, ranging from 70 K at the Orion Bar to values larger than 100 K in the ionized gas. Close to θ^1 Ori D, the temperature of the Ney-Allen nebula reaches values of 120 K. A high temperature (110 K), as compared to its surrounding area, is seen towards the Herbig-Haro object HH 203. The peak in τ_{warm} is located at the same distance as the PAH/mid-infrared peak (120″), while the cold dust component show two peaks at 120″ and 140″.

Perusal of the optical depths maps reveals that the cold component is strongly concentrated towards the Orion Molecular Cloud Core OMC-1, and besides the BN/KL region we also recognize Orion S, but the Orion Bar does not figure prominently. In contrast, the Orion Bar is very evident in the optical depth map of the warm component. The temperature map provides a complementary view: The cold component reaches a particularly low temperature in the cold molecular cloud core – as evident in the temperature map of the cold component – as expected from the high column density associated with this feature. We also note that the highest temperatures for the cold component are present in the ionized gas towards the West of the Trapezium and also within a small pocket near θ^2 Ori A. This same area around θ^2 Ori A and HH 203 sticks out as particularly warm in the warm component map. At first sight surprisingly, the Orion Bar shows up in the temperature map of the warm component as a relatively cold feature compared to the much warm material associated with the ionized gas. This reinforces the discussion in Section 3.3.1 that much of the mid-IR emission towards the North of the Orion Bar is associated with dust in the ionized gas. We also note the increased presence of the warm dust component beyond the extent of the Orion Bar traced in the submillimeter, which we attribute to dust associated with a thin layer of ionized gas that is quite evident in the optical and IR spectroscopic data (Rubin et al., 2011; Boersma et al., 2012).

The total dust emission was estimated by integrating the flux from the modified-blackbody fits. We can also assess the contribution from the cold and warm component to the overall IR emission. In the ionized zone, towards the Trapezium stars, the total luminosity is dominated by the warm component, being a factor of seven larger than the cold component on average. In the HII region, the ratio decreases with distance up to $115''$ – the Orion Bar – where it suddenly increases. Beyond the surface of the Orion Bar, the ratio decreases again, reaching a minimum of 0.6 at $\sim 150''$. The further increase beyond this minimum (towards the Southeast) is not associated with the bar as outlined by the sub-millimeter emission.

As mentioned in Section 3.3.1, the infrared emission is dominated by the BN/KL object, a region around the Trapezium and the Orion Bar PDR. We focus on the Trapezium region and the Bar, as the BN/KL object is not covered in all of our images. We extracted the total luminosity in the region shown in Figure 3.9: one in a rectangular aperture of $158 \times 20''$ (0.32×0.04 pc^2) at the Orion Bar. The total luminosity at the surface of the Orion Bar is 9.5×10^3 L$_\odot$.

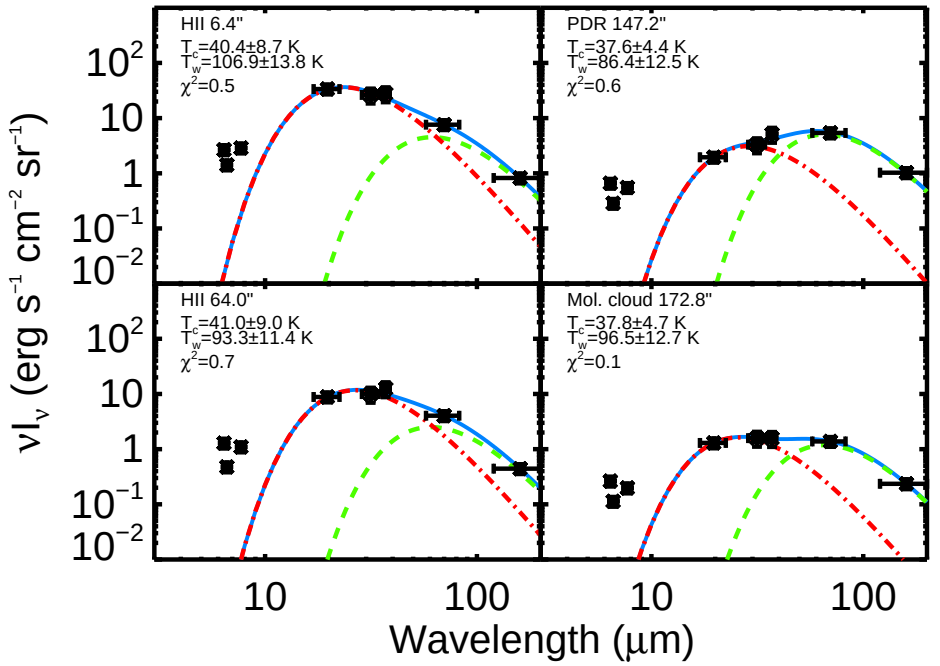

Figure 3.6: Examples of the SEDs at four positions. The results of the modified blackbody fits are also plotted.

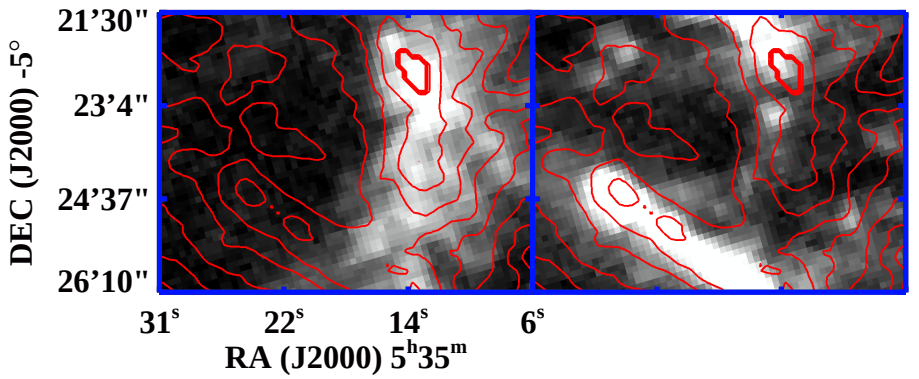

Figure 3.7: ^{13}CO data at two velocity components corresponding to OMC (left) and Orion Bar (right), the red contours are the PACS 160 μm emission.

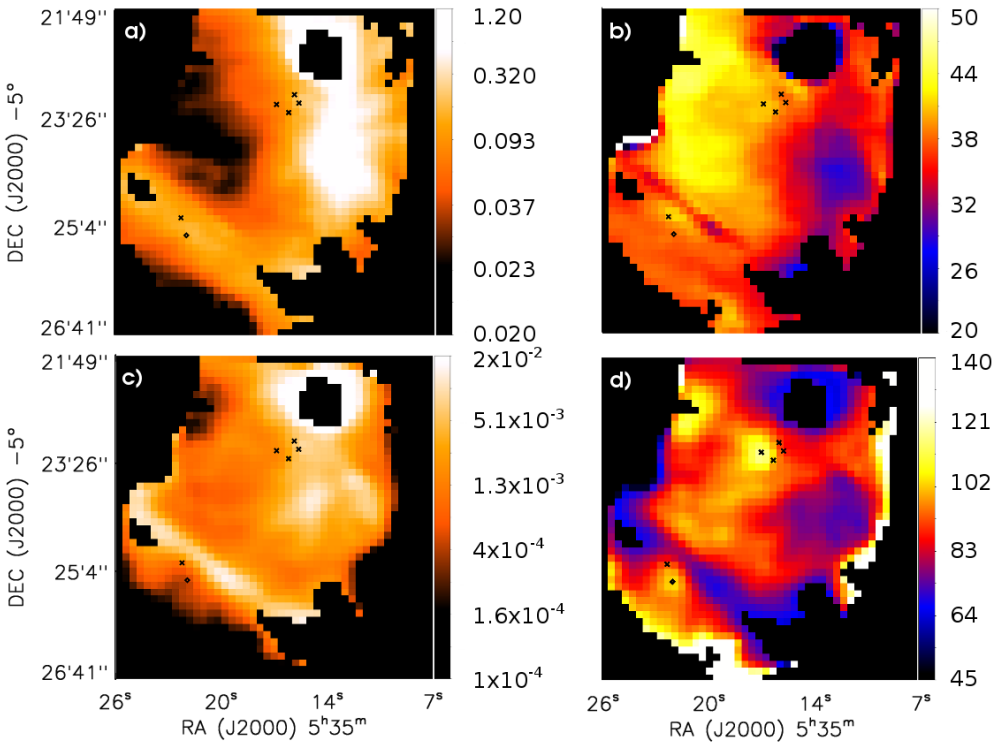

Figure 3.8: Temperature and optical depth maps of the two dust components revealed by the SED modeling. a) Optical depth,τ_{cold}, for the cold component. b) Temperature map for the cold component. c) Optical depth, τ_{warm}, for the warm component. d) Temperature map for the warm component.

3.4 Results

3.4.1 Geometry of the Orion Bar

The observed total infrared emission is a measure for the amount of stellar energy intercepted by the Orion Bar PDR and we can use this value to determine the geometric dimensions of the Bar. We will use the emission traced by the warm dust component to estimate the energy absorbed by the dust in the Orion Bar region ($L_{IR} = 9.5 \times 10^3$ L$_\odot$). We can derive a value for the absorbing area at the surface of the PDR, i.e.: $A_{abs} = L_{IR}/\left(L_\star/4\pi\ d^2\right)$. The minimum stellar luminosity of 1.4×10^5 L$_\odot$ corresponds to the often adopted G_0 of 5×10^4 (Tielens and Hollenbach, 1985), while the twice higher luminosity of the Trapezium cluster (Section 3.2) results in G_0 that is double this value. In contrast, Marconi et al. (1998) derived a G_0 of 2.6×10^4 from the fluorescent, near-IR OI lines, originating in the ionization front. Adopting this latter value,

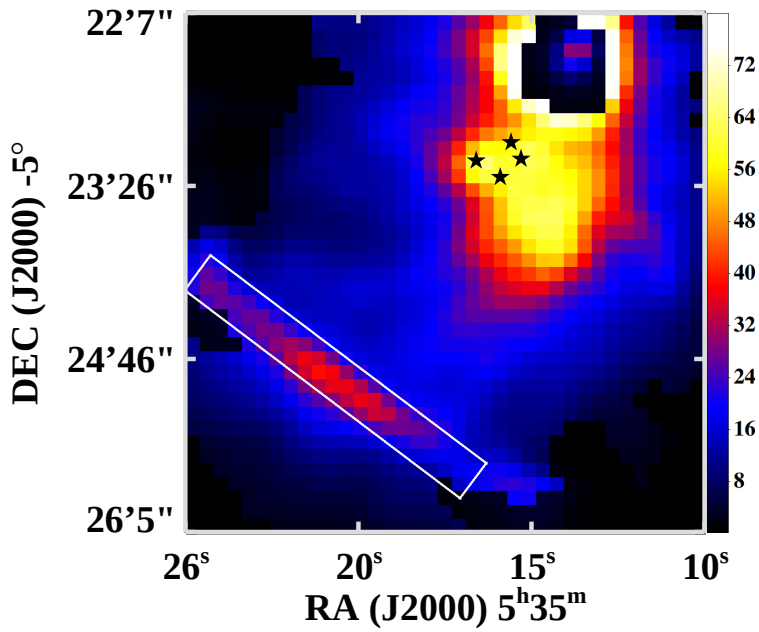

Figure 3.9: Total infrared luminosity from the blackbody fits, we extracted the luminosity in the aperture marked in white.

the absorbing area is 0.09 pc^2. Adopting a rectangular geometry and using the measured size of the Orion Bar (0.32 pc) as the other side of the rectangle, we obtain a transverse size of $l_{LOS} = 0.28$ pc.

The line of sight extent can also be derived from observed atomic or molecular column densities in the Orion Bar PDR, adopting a gas density. The observed C^+ and $C^{18}O$ column densities transformed to total H column densities using standard gas phase abundance ratios ($X(C^+) = 1.5{\times}10^{-4}$ and $X(C^{18}O) = 1 \times 10^{-7}$; Cardelli et al. 1996; Tielens 2005) are 7×10^{22} and 1.3×10^{23} cm^{-2}, respectively (Hogerheijde et al., 1995; Ossenkopf et al., 2013). The density in the PDR has been obtained from modeling molecular emission lines of 10^5 cm^{-3} (Simon et al., 1997). Slightly lower densities have been obtained from an analysis of the PDR cooling lines and from the observed stratification of the Bar adopting standard dust properties (Tielens et al., 1993) but we deem those more uncertain. Adopting the C^+-derived H-column density as appropriate for the atomic zone in the PDR, and a density of 1×10^5 cm^{-3}, we derive a length-scale of 0.23 pc for the line of sight. For comparison, deriving the EM associated with the ionization bar from the observed Hα intensity (Figure 4 in Wen and O’dell 1995) and the density derived from the [S II] lines (2.5×10^3,

Sánchez et al. 2007), we also arrive to a line of sight extent of the (ionized) bar of 0.3 pc. Note, though, that there is a large column density of foreground ionized gas in the same direction.

In summary, adopting the Marconi et al. (1998) value for G_0 measured in the ionization front, we arrive at $l_{LOS} = 0.28$ pc. This then implies that the actual distance from the Trapezium stars to the Orion Bar is $0.33 - 0.45$ pc – depending on the adopted luminosity – rather than the projected distance of 0.23 pc. Finally, from the observed width of the [O I] 6300 Å structure (0.02 pc) – much larger than the expected width of an ionization front (10^{-3} pc Tielens 2005) –, and the derived length scale of the Orion Bar, we arrive at an inclination of the Orion Bar of 4° with respect to the line of sight.

3.4.2 The Swept-up Shell

In Section 3.3.2, we identified the extent of the Orion Bar on the sky as the location of the shock front, some 0.1 pc from the ionization front. Most of the gas in this swept-up shell will be molecular and in pressure equilibrium with the atomic gas ($n = 10^5$ cm^{-1}, $T = 500$ K; Simon et al. (1997); Allers et al. (2005)) in the PDR. Adopting a temperature of 50 K for the molecular gas, we then arrive at a density of 10^6 cm^{-3}. The radial column density of the bar is then $N_{\rm H} \simeq 3 \times 10^{23}$ cm^{-2} and the total mass of swept-up material is 6×10^3 M$_\odot$. As the mass of ionized gas is very small ($\simeq 10$ M$_\odot$, we can infer an average density of 3×10^4 cm^{-3} before the star turned on; a typical density for a massive molecular cloud core (e.g.: Rathborne et al. 2006; Liu et al. 2014). Comparing this density with that of the ionized gas, we arrive at a shock velocity of $v_s \simeq \sqrt{n_o/n_e}\, C_s \simeq 3$ km s^{-1} with $C_s \approx 10$km s^{-1}, the sound velocity in the ionized gas (Tielens, 2005). Coupled with the location of the shell, we infer an age of 10^5 yr for θ^1 Ori C and the formation of the HII region. This should be considered an upper limit as the shock may have decelerated with time.

3.4.3 Dust extinction

In this Section, we determine the dust opacity in the ionized gas and PDR from the observations. The results show that the UV and IR opacities are about an order of magnitude less than for the diffuse ISM. In Section 3.5.3 we look at the implications.

3.4.3.1 The IR extinction in the HII region

We can estimate the IR extinction properties of the gas in the ionized gas by comparing our fits with the radio emission measure from Dicker et al. (2009)

and the electron density. From the warm dust maps, we have selected a region where the higher temperature and morphology indicates that it is associated with the ionized gas (white square in Figure 3.3). At this position, the measured 19.7 μm optical depths is 0.025 ± 0.003, while the emission measure – estimated from the published emission measure map of Dicker et al. (2009) is $7 \pm 0.5 \times 10^6$ cm^{-6} pc. With the measured electron densities (2500 ± 500 cm^{-3}), we arrive at a column density of $8 \pm 2 \times 10^{21}$ cm^{-2}. This then translates into a 19.7 μm dust opacities of $3.1 \pm 0.9 \times 10^{-24}$ cm^2/H-atom. This value is a factor of about 10 less than the measurements by Chiar and Tielens (2006) towards Cygn OB 2 and about a factor 4 less than in typical models for interstellar dust (1.3 to 1.6 $\times 10^{-23}$ cm^2/H-atom; Draine 2003).

3.4.3.2 The UV extinction in the HII region

In the HII region, dust grains and hydrogen compete for the absorption of stellar radiation but Lyman α will be (locally) absorbed by the dust. As in our previous study (Salgado et al., 2012), we can estimate the UV extinction produced by dust in the ionized region. The total IR luminosity associated with the ionization bar is measured to be 2.6×10^3 L$_\odot$ by integrating our modified-blackbody fits in this part of the HII region. From the emission measure image presented by Dicker et al. (2009), we estimate an average EM of 6×10^6 cm^{-6} pc, which corresponds to a Lyman α luminosity of 1.8×10^3 L$_\odot$. Hence, the dust heating due to absorption of star light is small in the ionized bar (800 L$_\odot$). From the geometry derived in section 3.3.2, we estimate that the fraction of the stellar luminosity available corresponds to $A_{abs}/4\pi d^2$. We use $A_{abs} = 0.09$ pc^2 which goes with an actual distance of 0.45 pc and a luminosity of 2.7×10^5 L$_\odot$ to arrive at the dust UV optical depth, τ_{UV}, of 8×10^{-2}. With the width of this region (0.05 pc) and a density of 2.5×10^3 cm^{-3} (Wen and O'dell, 1995), this results in a UV dust opacity of 2×10^{-22} cm^2/H-atom. These values can be compared to the calculated UV opacity of dust in the diffuse ISM, which – for an R_V of 5.5 – ranges from 1 to 1.5×10^{-21} cm^2/H-atom over the wavelength range of $2200 - 912$ Å (Weingartner and Draine, 2001; Draine, 2003). Similar values are actually obtained for sight-lines in the diffuse ISM characterized by $R_V = 3.1$. Hence, the UV opacity of dust in the Orion HII region is a factor of $\simeq 5$ less than in the diffuse ISM.

3.4.3.3 IR Extinction in the PDR

The 19.7 μm optical depth of the warm dust in the Orion Bar PDR is measured to be 0.2 (Figure 3.8). Taking the H-column density derived from the CII observations (7×10^{22} cm^2; Ossenkopf et al. (2013); see Section 3.4.1),

we arrive at a 19.7 μm extinction per H-atom of 2.9×10^{-24} cm^2/H-atom. These values are a factor 10 less than the values measured towards Cyg OB2 (3.7×10^{-23} cm^2/H-atom Chiar and Tielens 2006) and a factor 5 less than the models from Draine (2003) (1.3 to 1.6×10^{-23} cm^2/H-atom, depending on the value for R_V).

3.4.3.4 The Penetration of UV Photons in the PDR

Since PAHs are excited by FUV photons, the decrease in PAH emission traces the dust grain extinction through the PDR. The emission of PAHs at a distance d is given by:

$$F_{PAH}(d) = F_{PAH}(peak) \times e^{-\tau_{UV}(radial)}, \tag{3.1}$$

with $\tau_{UV}\,(radial) = N_d^T \times \sigma_{UV}$ the radial optical depth. The PAH emission decreases by a factor of 8 over a length of $30''$ (0.06 pc) from the peak emission. With a density of 10^5 cm^{-3}, this translates into a UV opacity of 1.6×10^{-22} cm^2/H-atom. Hence, as for the dust in the ionized gas, the dust in the PDR is characterized by a UV opacity which is about a factor 10 less than for dust in the diffuse ISM.

3.5 Discussion

3.5.1 The Dust Temperature and Lyα Heating

It has been long suspected that trapped Lyα photons can be a major source of dust heating in HII regions (e.g. Wright 1973; Garay et al. 1993; Smith et al. 1999). As the discussion in Section 3.4.3.2 demonstrates, Lyα photons are very important for the heating of dust in the Orion Nebula. Here, we will compare the derived temperatures of the warm dust component. The total heating of the dust depends on the distance to the central star, the radial extinction of UV photons towards the star and the number of trapped Lyα photons. These two sources of heating lead to a different distance dependence for the temperature. Because of resonant scattering, Lyα photons are absorbed on the spot and the contribution to the heating rate is,

$$\Gamma_{\mathrm{Ly}\alpha} = n_e n_H f \alpha_H^{(2)} h\nu_\alpha / n_d, \tag{3.2}$$

with n_e the electron density, n_H the hydrogen density, n_d the dust density, $h\nu_\alpha$ the energy of the Lyα photon (10.2 eV), $f = 0.7$ is fraction of recombination to levels higher than 2 that lead to emission of a Lyα photon, and $\alpha_H^{(2)}$ is the recombination coefficient of Hydrogen (case B). In addition, there is the direct

stellar radiation,

$$\Gamma_d\,(a,r) = \pi a^2 \frac{L_\star(\mathrm{UV})}{4\pi r^2} e^{-\tau_{radial}} Q_{abs}(\mathrm{UV}) + \Gamma_{\mathrm{Ly}\alpha} \tag{3.3}$$

where τ_{radial} is the UV optical depth from the star to a point r and a is the radius of a spherical grain. The dust temperature can be obtained by equating the heating with the wavelength integrated emission of a dust grain. The emission can be approximated well by:

$$\Gamma_{em} = 4\pi a^2 Q_0 \sigma T_d^6, \tag{3.4}$$

where σ is the Stefan-Boltzmann constant and for the constant Q_0 we adopt the properties of silicates [$Q_0 = 1.25 \times 10^{-5}(a/0.1\,\mu\mathrm{m})^{0.06}$, Tielens 2005]. The dust temperature is then given by:

$$T_d^6 = \frac{Q_{abs}(\mathrm{UV}) G_0}{4 Q_0 \sigma} \left[\frac{3 h\nu_\alpha f}{\tau_d \overline{h\nu}} + \left(\frac{R_s}{r} \right)^2 \right], \tag{3.5}$$

where $\overline{h\nu}$ is the average photon energy per ionizing photon ($L_\star/N_{ion} \simeq 49$ eV, for the parameters of θ^1 Ori C), $R_s = 0.23$ pc is the Strömgren radius and $\tau_d = 0.08$ is the dust optical depth. We have adopted $G_0 = 2.6 \times 10^4$ (Section 3.4.1), $Q_{abs}(\mathrm{UV}) \approx 1$. We emphasized that all these parameters – except for the detailed absorption/emission properties of the dust – are directly derived from observations. Note that the calculated dust temperature depends on the ratio of the UV absorption to the IR emission cross section. While we have derived a much reduced dust opacities in Section 3.4.3, the ratio of the two is actually similar to what we have adopted here.

The results are compared to the observed temperature in Figure 3.10. The calculated temperatures show the expected characteristic of Lyman α heating; i.e., constant dust temperature throughout the ionized gas. Heating by the photons from the central star does not start to dominate the dust temperature until $r \lesssim 0.25\ R_s$. We note that if we exclude Lyman α heating, the geometric dilution of the radiation field leads to a noticeable decrease in the dust temperature throughout the region. This is not present in the data again illustrating the importance of Lyman α heating of the dust. The absence of an upturn in the observed temperature at small radii likely reflects the absence of dust close to θ^1 Ori C as the stellar wind may have created a dust free cavity. Finally, in order to reproduce the observed temperatures, dust grains with sizes between $0.1 - 1\ \mu$m are required. This value is somewhat large compared to the dust in the diffuse ISM. We discuss this further in Section 3.5.2.

3.5.2 Properties of the Dust

We have determined opacities in the UV and IR – in units of cm^2/H-atom – both for dust in the ionization bar and in the PDR (c.f., Section 3.4.3). As

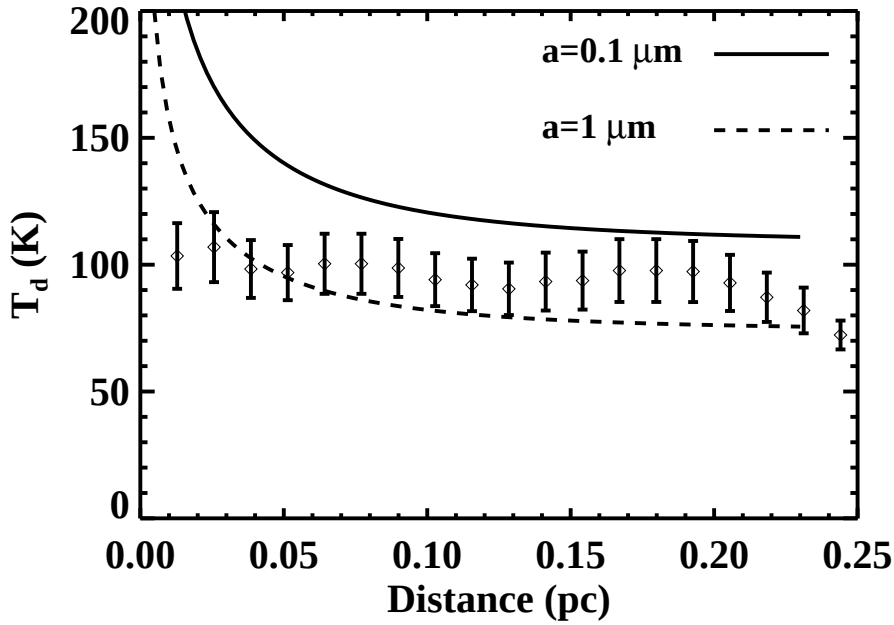

Figure 3.10: Temperature as a function of distance for different dust grain size: 0.1 μm (solid line) and 1 μm (dashed line). Symbols represent derived dust temperatures of the warm component.

emphasized before, the derived UV and IR opacities are reduced by a factor $5 - 10$ as compared to dust in the diffuse ISM. We attribute this decreased opacity to the effects of coagulation. Theoretical studies show that coagulation can greatly reduce the extinction per unit mass both in the UV and the IR, if the grains can grow to very large sizes (Ossenkopf and Henning, 1994; Ormel et al., 2011). Detailed models show that a factor of 10 reduction in the opacity is reached after a time, $t \simeq 100\,\tau_0$ where τ_0 is the collision timescale at the onset of coagulation,

$$\tau_0 \;=\; (n_d \Delta v \sigma_d)^{-1} \;\simeq\; 8.5 \times 10^4 \left(\frac{a_0}{0.1\,\mu\mathrm{m}}\right)^{1/2} \left(\frac{n}{10^5\,\mathrm{cm}^{-3}}\right)^{-3/4} \left(\frac{T}{10\,\mathrm{K}}\right)^{-1/4} \tag{3.6}$$

with n_d, Δv and σ_d are the number density, relative velocity and cross section of the grains (Ormel et al., 2009). In the right-hand-side of this equation, an initially normal dust-to-gas ratio was adopted and a_0, n, and T are the size of the monomer, gas density, and temperature, respectively. At this point ($t \simeq 100\,\tau_0$), the calculated porosity of the aggregates is $\simeq 0.3$ and the aggre-

gate size is ~ 10 μm. From this timescale, we infer that the large grain size must reflect coagulation before the formation of θ^1 Ori C, the HII region, and the PDR; i.e., during the cold dark cloud phase of Orion A. During this phase, coagulation is much assisted by the presence of ice mantles. However, when the dust temperature reaches some 75 K, the ice will sublimate on a timescale of 10^4 yr, but we surmise that ice sublimation associated with such gentle thermal processing will not affect the structure of the dust aggregates. Once the dust leaves the shielded environment of the PDR and enters the HII region, further processing may occur. Sputtering will have little effect at $T = 10^4$ K but grain-grain collisions, even at $\simeq 5$ m s^{-1}, may lead to fragmentation (Wada et al., 2013; Krijt et al., 2015). Our results suggest, though, that this processing takes place on a timescale long compared to the evolution of the HII region. Large dust grains seem to be a common characteristic of dense cloud cores as evidenced from near-infrared scattered light images (e.g.: Pagani et al. 2010; Steinacker et al. 2010). Likewise, analysis of the IR emission from the HII region, IC 434, also inferred the presence of large dust aggregates in the champagne flow from the dark cloud, L1630 Ochsendorf et al. (2014a).

3.5.3 Dust in HII Regions

There has been a long history of infrared studies of dust in HII regions (e.g.: Ney et al. 1973; Harper 1974). Here, we will place our analysis of the Orion HII region in context with a recent study of the W3(A) HII region and the results from the GLIMPSE survey.

In a previous study, Salgado et al. (2012) analyzed the dust emission in W3(A) using the same mid-infrared FORCAST filters. Like Orion, W3(A) is a young, compact HII region and is powered by a similar ionizing star. The ionized gas emission in the Orion nebula, as traced by Hα, is high close to the Trapezium stars then it slowly decreases up to 0.18 pc where it sharply increases, while at larger distances it sharply decreases again (Figure 3.4). Analysis of the optical emission morphology and spectra of the HII region reveals that the ionized gas is distributed in a thin shell (0.02 pc) bounded at the outside by the ionization front (Wen and O'dell, 1995). The ionized gas (as traced by free-free emission at 2 cm) in W3(A) has a similar structure, but the ionized gas shell is much thicker ($\simeq 0.1$ pc).

When comparing the dust emission of Orion with W3(A) we also see some similarities in the spatial distribution. In Orion, the 19 μm emission shows a component coinciding with the Orion Bar and one that is associated with dust in the ionized gas (Figure 3.3; Section 3.3.2). The other IR dust/PAH tracers only peak up in the Orion Bar PDR. For W3(A), the 19.7 μm emission traces dust well mixed in with the ionized gas shell. As for Orion, at other wavelengths, the dust (and PAH) emission clearly peak in the PDR surrounding the ionized

shell. Hence, for both regions, the 19.7 μm flux originates from dust mixed in with the ionized gas. We note that unlike Orion, the 19.7 μm map of W3(A) does not show a secondary peak at the PDR (Salgado et al., 2012). In the PDR the dust is exclusively heated by stellar photons and this difference in 19.7 μm morphology merely reflects the smaller scale size and concomitantly higher dust temperature for Orion as compared to W3(A).

The heating of the dust is however different for these two HII regions. In Orion, resonantly scattered Lyman α photons contribute some 2/3 of the dust heating in the ionized gas; the remainder is due to absorption of stellar FUV photons. In contrast, for W3(A), dust heating is dominated by stellar photons with only a minor contribution from Lyman α. Our analysis shows that this reflects the very low optical depth of dust in the ionized gas in Orion ($\tau_{UV} \simeq 0.08$). For W3(A), the UV optical depth was measured to be $\simeq 1$ and consequently stellar heating is much more important (cf., Equation 3.2). To phrase it differently, irrespective of the dust properties, all the Lyman α energy will eventually wind up in the dust. In contrast, the absorption of stellar photons depends strongly on the dust opacity per H-atom and, for these two regions, the derived UV dust opacities (per H-atom) differ by almost a factor 100.

This difference in dust opacity per H-atom must reflect a difference in evolution between these two regions. Both stars formed in dense cores where coagulation had likely reached a steady state. Both HII regions are also very young: W3(A) is slightly larger but Orion is already optically visible. Morphologically speaking, for W3(A), the shell structure likely betrays the importance of radiation pressure on the ionized gas and the dust, although we recognize that theoretical models predict a much shallower rise in the shell density than observed (Draine, 2011). In contrast, for Orion, the HII region has broken out of the molecular cloud and has created a champagne flow (Güdel et al., 2008) and the dust is dragged along (Ochsendorf et al., 2014a). The difference in dust properties might therefore originate in or relate to the champagne flow phase in the evolution of compact HII regions that W3(A) has not yet entered in. Possibly it therefore reflects a size-sorting of the dust due to radiation pressure during the blister phase (Ochsendorf and Tielens, 2015).

The Spitzer/GLIMPSE survey has revealed some 6000 bubble HII regions in the Milky Way. These are invariably characterized by 24 μm emission associated with dust inside the bubble while emission at 8 μm and at far-infrared wavelength traces the PDR surrounding the HII region (Churchwell et al., 2006, 2007; Deharveng et al., 2010). The morphology of the compact HII regions, Orion and W3(A), is very similar where dust in the ionized gas is visible at 19.7 μm while the PDR is traced in the PAH and colder dust emission. As the spectral energy distribution of the dust in the ionized gas peaks around 20 μm in all cases, the dust must have very similar temperatures, suggesting

that Lyman α heating may dominate dust heating in HII regions in general. Alternatively, the 24 μm emission in these bubbles may trace a dust wave where the radiation pressure of the stellar light stops onrushing dust in a champagne flow and forces it in an arc-like structure around the star (Ochsendorf et al., 2014a,b). As the stellar properties are very similar, the dust wave may form at very similar distances, resulting in very similar temperatures.

3.5.4 Cooling Lines and Photoelectric Heating Efficiency

In dense PDRs, gas cooling is dominated by emission of forbidden transition lines of [O I] at 63 μm and [C II] at 157 μm (Hollenbach and Tielens, 1999). Observations of the gas cooling lines in the Orion Bar have been discussed extensively by Bernard-Salas et al. (2012). Here we reanalyzed the data, including the mid-infrared contribution to the SED and the total IR emission of this region. In PDRs, the dominant heating process is due to the photoelectric effect in PAHs and small grains (de Jong et al., 1980; Bakes and Tielens, 1994). The efficiency of the process can be measured directly from the ratio between the main gas cooling lines and the total energy absorbed by PAHs and dust grains.

We used the PACS [O I] at 63 and 145 μm, and the [C II] at 157 μm lines to determine the photoelectric heating efficiency, i.e. the ratio between $[\mathrm{O\ I}]_{63}+[\mathrm{C\ II}]_{157}+[\mathrm{O\ I}]_{145}$ and the total IR emission derived from the blackbody fits (Section 3.3.3). Typical flux values for the lines are 7×10^{-2} and 6×10^{-3} ergs s^{-1} cm^{-2} sr^{-1} for the [O I] at 63 μm and 145 μm, respectively. For the [C II] line, a typical value is 8×10^{-3} ergs s^{-1} cm^{-2} sr^{-1}. In the Orion Bar, we find an efficiency of 2×10^{-3} which increases further into the PDR and can reach values as high as 7×10^{-3} (see Figure 3.11). The values found here are similar to those derived from Table 3 in Herrmann et al. (1997) and for M17 (Meixner et al., 1992). In this analysis, we assume that the far-infrared dust continuum emission is a good measure for the UV flux locally absorbed. That is a good assumption at the surface of the PDR, where FUV photons dominate. However, deeper in, the stellar UV flux is attenuated and absorption of mid-infrared photons produced by warm dust in the surface layers of the PDR become an important dust heating source. The effect of this is that the actual increase of the heating efficiency (defined as gas heating over absorbed FUV flux, Tielens and Hollenbach, 1985) increases even more than the factor 2 indicated above. This increase in the heating efficiency with depth in to the PDR is a standard feature of photo-electric heating models. As the UV field decreases, the PAHs and very small dust grains become less positively charged and the heating efficiency increases (Bakes and Tielens, 1994).

In Figure 3.12, we show the photoelectric efficiency as a function of the ionization parameter, $\gamma = G_0\sqrt{T}/n_e$ along a line perpendicular to the Orion

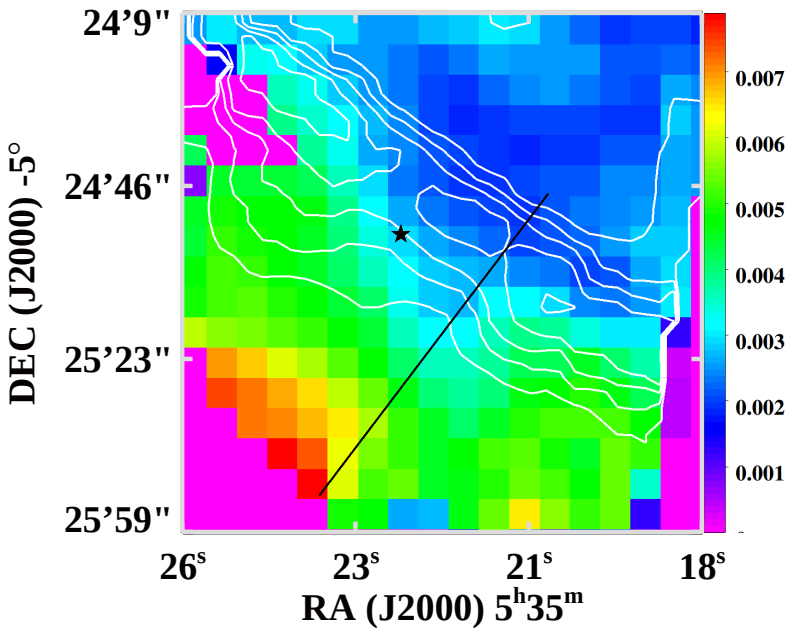

Figure 3.11: Photoelectric heating efficiency map, the star marks the position of θ^2 Ori A and the line corresponds to the crosscut for regions in Figure 3.12. The crosscut extends from the surface of the PDR to deep in the molecular cloud, with a position angle of 143° measured counter-clockwise from north. Overlaid in white is the contour map of [O I], the main cooling line. The photoelectric heating efficiency increases with distance from the trapezium stars.

Bar surface, which avoids – as best as possible – the clumps present in the region. In this analysis, we assume that the region is homogeneous in temperature ($T = 500$ Parmar et al. 1991; Allers et al. 2005) and an electron density ($n_e = X_e n_H$) with an electron abundance equal to the gas phase carbon abundance ($X_e = 1.5 \times 10^{-4}$; Cardelli et al. 1996) and $n_H = 10^5$ cm^{-3} (Simon et al., 1997). The variation in the ionization parameter is then largely due to variation in the penetrating UV field, which we approximate by the incident radiation field ($G_0 = 2.6 \times 10^4$ in Habing units, Section 3.4.1) extincted by $\tau_{UV} = 8(d/30'')$ (Section 3.4.3.4). The figure illustrates well that as the ionization parameter increases, the heating efficiency decreases. A similar trend was also noted by Okada et al. (2013) in their analysis of a sample of 6 PDRs. However, as their data set is very inhomogeneous and the ionization parameters are difficult to determine in an absolute sense, the trend is less clear. In this study, we focus on a single region where variations in the ionization parameter

are driven by the drop of the radiation field and a clear trend is revealed. We do note though that the absolute scale of the ionization parameter does depend on the adopted temperature and density. It is reasonable to assume that the region is in pressure equilibrium and hence the ionization parameter would scale as $G_0/\sqrt{T}$. We have indicated points beyond the peak of the H_2 emission where this variation in temperature would become relevant as red in Figure 3.12. The ionization parameter at these locations might have been underestimated by up to a factor $\simeq 2.5$ (i.e., $\sqrt{T_{H_2}/T_{CO}} = \sqrt{500/75}$).

We recognize the general increase in the heating efficiency as predicted by model studies (Bakes and Tielens, 1994; Weingartner and Draine, 2001). However, the observed heating efficiency differs from that expected from models. The theoretical models were developed for the diffuse ISM where observed heating efficiencies are higher (Wolfire et al., 1995; Hollenbach and Tielens, 1999). This difference in heating efficiency may just reflect a difference in dust properties; i.e., a lower abundance of PAHs and very small grains in the Orion Bar PDR (Section 3.5.2).

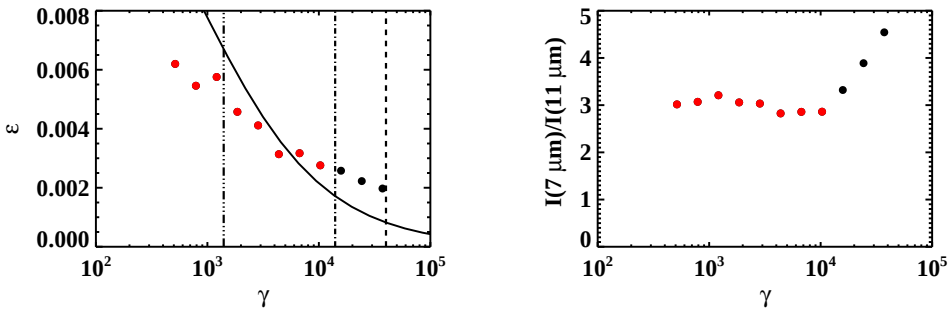

Figure 3.12: Photoelectric heating efficiency as a function of ionization parameter ($G_0\sqrt{T}/n_e$) along the cross cut through the Orion Bar (Figure 3.11). The dashed line marks the position of the ionization front, the dot-dashed line the position of H_2 peak and the dot-dot-dashed the end of swept up gas; the solid line is the model for photoelectric heating from Bakes and Tielens (1994) scaled sown by a factor of 3. G_0 was estimated from the incident radiation field attenuated in the Bar. The temperature ($T = 500$ K) and electron density ($n_e = 15$ cm^{-3}) were assumed to be constant (see text for details). Black dots refer to warm ($T \simeq 500$ K) gas traced by the pure rotational lines of H_2. The red dots are cooler molecular gas ($T \simeq 50 - 100$ K) traced by CO.

The photoelectric heating efficiency is expected to be linked to the degree of ionization of the PAHs and very small grains. For PAHs, the degree of ionization can be traced by the ratio between the 7.7 μm and the 11.3 μm

features as the 7.7 μm feature is emitted by ionized PAH and the 11.3 μm by neutral PAHs (DeFrees et al., 1993; Langhoff, 1996; Allamandola et al., 1999). Following Galliano et al. (2008), we used the ISOCAM-CVF data to get values for the ionized to neutral ratio of PAHs (Figure 3.12). As expected, there is a clear increase in the fraction of PAH cations from the H_2 peak to the front of the PDR, in good agreement with the trend found by Galliano et al. (2008). However, we notice that the PAH ratio reaches a plateau starting at the H_2 peak until the end of the dense bar (which we associate with the swept up shell). Perhaps, this reflects the influence of anions deep in the PDR.

As noted in Section 3.3.2, both the cooling line and the dust emission display a clumpy distribution. We also see variations of the photoelectric heating efficiency parallel to the Orion Bar surface. However, the clumpy structure apparent in the cooling line maps is not seen in the photoelectric heating map (Figure 3.11). It seems that the increased density associated with clumps does not translate in an increased photoelectric heating efficiency. These observations illustrate that further detailed studies of the cooling lines and dust emission coupled with density probes (such as molecular tracers) are needed to probe the relationship between gas cooling and the PAH/dust components responsible for the heating.

3.6 Summary and Conclusions

We analyzed the infrared emission in the Orion star forming region in six bands observed with the FORCAST instrument on board of SOFIA. We complemented the dataset with public published photometry and spectroscopy ranging from optical to far-infrared wavelengths. The FORCAST images show a complex structure and we recognize emission arising in the Orion Bar PDR, the BN/KL object and the Ney-Allen nebula. Our analysis shows that the *Herschel*/PACS far-infrared emission is associated with the cold molecular cloud. The mid-infrared emission is not spatially correlated with the far-infrared emission and must be produced in the PDR and, partially, in the HII region.

We constructed SEDs after convolving the FORCAST images to the PACS 160 μm resolution. By fitting the SEDs with two modified blackbodies, we derived dust temperatures and column densities for dust associated with the molecular cloud and the PDR/HII region. Most of the dust mass is in the cold dust component which is associated with the background cold and dense molecular cloud. The luminosity, on the other hand, is dominated by the warm dust component associated with the PDR/HII region. We obtained the total infrared luminosity by integrating our blackbody fits over wavelength between 1 and 1000 μm. The results of the fits were used to obtain the geometry of the Orion Bar PDR. We measured a depth along the line of sight of 0.28 pc and

an inclination angle of 4°.

We have determined that the Orion Bar extends from the ionization front located at 0.23 pc from θ^1 Ori C up to the shock front located at about 0.1 pc from the ionization front. The amount of mass swept by the expansion of the HII region is 6×10^3 $M_\odot$ and we estimate an age of $\simeq 10^5$ yr for the HII region and θ^1 Ori C.

By comparing the 19.7 μm image with ionized gas radio emission we have determined the opacity (extinction per hydrogen atom) in the HII region to be a factor of 5 lower than models for the diffuse interstellar medium. In addition, we have computed the UV opacity in the ionized gas by comparing the infrared emission and radio estimates. As for the infrared opacity, the UV opacity value is a factor of 5 lower than that of the diffuse ISM.

We measured infrared opacity in the PDR by comparing the optical depth and the density. The value obtained by this method is a factor of 5 less than models for the diffuse ISM. By measuring the penetration of UV photons in the PDR, as traced by the PAH emission, we derived an UV opacity a factor of 10 less than that of the ISM.

Our analysis shows that Lyα heating is important in Orion at distances $r > 0.25R_s$. The dust temperature profile can be explained by the presence of large grains (between 0.1-1 μm).

The lower opacities as compared to ISM values and the Lyα heating behavior depend on the size of the dust grains. The observed values for the opacities and dust temperature in the ionized gas can be explained by the presence of large grains. We attribute the increase in size of the grains to dust coagulation during the molecular cloud phase previous to the birth of the ionizing stars.

We measure the photoelectric heating in the Orion Bar from the observed fine-structure cooling lines and the IR continuum emission. The observations reveal that the photo-electric efficiency decreases towards the surface of the PDR. Theoretical models attribute this to a charging-up of the PAHs and very small grains. We estimate values for the ionization parameter as a function of depth in the Orion Bar PDR. The derived heating efficiency as a function of ionization parameter agrees qualitatively well with the models but is less by about a factor 5. As the models were derived for the diffuse ISM, this quantitative difference may merely reflect a difference in PAH abundance.

Chapter 4

Low Frequency Carbon Radio Recombination Lines I: Calculations of Departure Coefficients

Based on: Salgado, F. et al., 2015

Abstract

In the first paper of this series, we study the level population problem of recombining carbon ions. We focus our study on high quantum numbers anticipating observations of Carbon Radio Recombination Lines to be carried out by the LOw Frequency ARray (LOFAR). We solve the level population equation including angular momentum levels with updated collision rates up to high principal quantum numbers. We derive departure coefficients by solving the level population equation in the hydrogenic approximation and including low temperature dielectronic recombination effects. Our results in the hydrogenic approximation agree well with those of previous works. When comparing our results including dielectronic recombination we find differences mainly due to differences in the collision rates. A comparison with observations is discussed in an accompanying article, as radiative transfer effects need to be considered.

4.1 Introduction

The interplay of stars and their surrounding gas leads to the presence of distinct phases in the interstellar medium (ISM) of galaxies (e.g. Field et al. 1969; McKee and Ostriker 1977). Diffuse atomic clouds (the Cold Neutral Medium, CNM) have densities of about 50 cm^{-3} and temperatures of about 80 K, where atomic hydrogen is largely neutral but carbon is singly ionized by photons with energies between 11.2 eV and 13.6 eV. The warmer ($\sim$ 8000 K) and more tenuous ($\sim$ 0.5 cm^{-3}) intercloud phase is heated and ionized by FUV and EUV photons escaping from HII regions (Wolfire et al., 2003), usually referred to as the Warm Neutral medium (WNM) and Warm Ionized Medium (WIM). The phases of the ISM are often globally considered to be in thermal equilibrium and in pressure balance (Savage and Sembach, 1996; Cox, 2005). However, the observed large turbulent width and presence of gas at thermally unstable, intermediate temperatures attests to the importance of heating by kinetic energy input. In addition, the ISM also hosts molecular clouds, where hydrogen is in the form of H_2 and self-gravity plays an important role. All of these phases are directly tied to key questions on the origin and evolution of the ISM, including the energetics of the CNM, WNM and the WIM; the evolutionary relationship of atomic and molecular gas; the relationship of these ISM phases with newly formed stars; and the conversion of their radiative and kinetic power into thermal and turbulent energy of the ISM (e.g. Cox 2005; Elmegreen and Scalo 2004; Scalo and Elmegreen 2004; McKee and Ostriker 2007).

The neutral phases of the ISM have been studied using optical and UV observations of atomic lines. These observations can provide the physical conditions but are limited to pinpoint experiments towards bright background sources and are hampered by dust extinction (Snow and McCall, 2006). At radio wavelengths, dust extinction is not important and observations of the 21 cm hyperfine transition of neutral atomic hydrogen have been used to study the neutral phases (e.g. Weaver and Williams 1973; Kalberla et al. 2005; Heiles and Troland 2003b). On a global scale, these observations have revealed the prevalence of the two phase structure in the interstellar medium of cold clouds embedded in a warm intercloud medium but they have also pointed out challenges to this theoretical view (Kulkarni and Heiles, 1987; Kalberla and Kerp, 2009). It has been notoriously challenging to determine the physical characteristics (density, temperature) of the neutral structures in the ISM as separating the cold and warm components is challenging (e.g. Heiles and Troland 2003a). In this context, Carbon radio recombination lines (CRRLs) provide a promising tracer of the neutral phases of the ISM (e.g. Peters et al. 2011; Oonk et al. 2015b).

Carbon has a lower ionization potential (11.2 eV) than hydrogen (13.6 eV)

and can be ionized by radiation fields in regions where hydrogen is largely neutral. Recombination of carbon ions with electrons to high Rydberg states will lead to CRRLs in the sub-millimeter to decameter wavelength range. Carbon radio recombination lines have been observed in the interstellar medium of our Galaxy towards two types of clouds: diffuse clouds (e.g.: Konovalenko and Sodin 1981; Erickson et al. 1995; Roshi et al. 2002; Stepkin et al. 2007; Oonk et al. 2014) and photodissociation regions (PDRs), the boundaries of HII regions and their parent molecular clouds (e.g.: Natta et al. 1994; Wyrowski et al. 1997; Quireza et al. 2006). The first low frequency (26.1 MHz) carbon radio recombination line was detected in absorption towards the supernova remnant Cas A by Konovalenko and Sodin (1980) (wrongly attributed to a hyperfine structure line of ^{14}N, Konovalenko and Sodin 1981). This line corresponds to a transition occurring at high quantum levels ($n = 631$). Recently, Stepkin et al. (2007) detected CRRLs in the range 25.5–26.5 MHz towards Cas A, corresponding to transitions involving levels as large as $n = 1009$.

Observations of low frequency carbon recombination lines can be used to probe the physical properties of the diffuse interstellar medium. However, detailed modeling is required to interpret the observations. Watson et al. (1980); Walmsley and Watson (1982a) showed that, at low temperatures ($T_e \lesssim 100$ K), electrons can recombine into carbon ions by simultaneously exciting the $^2P_{1/2} - {}^2P_{3/2}$ fine structure line, a process known as dielectronic recombination. Such recombination process occurs to high n states, and can explain the behavior of the high n CRRLs observed towards Cas A. Walmsley and Watson (1982a) modified the code from Brocklehurst and Salem (1977) to include dielectronic recombination. Payne et al. (1994) modified the code to consider transitions up to 10000 levels. All of these results assume a statistical distribution of the angular momentum levels, an assumption that is not valid at intermediate levels for low temperatures. Moreover, the lower the temperature, the higher the n-level for which that assumption is not valid.

The increased sensitivity, spatial resolution, and bandwidth of the Low Frequency ARray (LOFAR, van Haarlem et al. 2013) is opening the low frequency sky to systematic studies of high quantum number radio recombination lines. The recent detection of high level carbon radio recombination lines using LOFAR towards the line of sight of Cas A (Asgekar et al., 2013), Cyg A (Oonk et al., 2014), and the first extragalactic detection in the starburst galaxy M82 (Morabito et al., 2014a) illustrate the potential of LOFAR for such studies. Moreover, pilot studies have demonstrated that surveys of low frequency radio recombination lines of the galactic plane are within reach, providing a new and powerful probe of the diffuse interstellar medium. These new observations have motivated us to reassess some of the approximations made by previous works and to expand the range of applicability of recombination line theory in terms of physical parameters. In addition, increased computer power allows us to

solve the level population problem considering a much larger number of levels than ever before. Furthermore, updated collisional rates are now available (Vrinceanu et al., 2012), providing more accurate results. Finally, it can be expected that the Square Kilometer Array, SKA, will further revolutionize our understanding of the low frequency universe with even higher sensitivity and angular resolution (Oonk et al., 2015b).

In this work, we present the method to calculate the level population of recombining ions and provide some exemplary results applicable to low temperature diffuse clouds in the ISM. In Section 5, we will present results specifically geared towards radio recombination line studies of the diffuse interstellar medium. In Section 4.2, we introduce the problem of level populations of atoms and the methods to solve this problem for hydrogen and hydrogenic carbon atoms. We also present the rates used in this work to solve the level population problem. In Section 4.3, we discuss our results focusing on hydrogen and carbon atoms. We compare our results in terms of the departure coefficients with previous results from the literature. In Section 4.4, we summarize our results and provide the conclusions of the present work.

4.2 Theory

A large fraction of our understanding of the physical processes in the Universe comes from observations of atomic lines in astrophysical plasmas. In order to interpret the observations, accurate models for the level population of atoms are needed as the strength (or depth) of an emission (absorption) line depends on the level populations of atoms. Here, we summarize the basic ingredients needed to build level population models and provide a basic description of the level population problem. We begin our discussion by describing the line emission and absorption coefficients (j_ν and k_ν, respectively), which are given by (Shaver, 1975; Gordon and Sorochenko, 2009):

$$j_\nu = \frac{h\nu}{4\pi} A_{n'n} N_{n'} \phi(\nu), \tag{4.1}$$

$$k_\nu = \frac{h\nu}{4\pi} \left(N_n B_{nn'} - N_{n'} B_{n'n} \right) \phi(\nu), \tag{4.2}$$

where h is the Planck constant, $N_{n'}$ is the level population of a given upper level (n') and N_n is the level population of the lower level (n); $\phi(\nu)$ is the line profile, ν is the frequency of the transition and $A_{n'n}$, $B_{n'n}(B_{nn'})$ are the Einstein coefficients for spontaneous and stimulated emission (absorption) [1], respectively.

[1] We provide the formulation to obtain the values for the rates in Appendix C.

Under local thermodynamic equilibrium (LTE) conditions, level populations are given by the Saha-Boltzmann equation (e.g. Brocklehurst 1971):

$$N_{nl}(LTE) \quad = \quad N_e N_{ion} \left(\frac{h^2}{2\pi m_e k T_e} \right)^{3/2} \frac{\omega_{nl}}{2\omega_i} e^{\chi_n}, \chi_n = \frac{hcRyZ^2}{n^2 kT_e}, \quad (4.3)$$

where T_e is the electron temperature, N_e is the electron density in the nebula, N_{ion} is the ion density, m_e is the electron mass, k is the Boltzmann constant, h is the Planck constant, c is the speed of light and Ry is the Rydberg constant; ω_{nl} is the statistical weight of the level n and angular quantum momentum level l [$\omega_{nl} = 2(2l+1)$, for hydrogen], and ω_i is the statistical weight of the parent ion. The factor $\left(h^2/2\pi m_e k T_e\right)^{1/2}$ is the thermal de Broglie wavelength, $\Lambda(T_e)$, of the free electron [2]. In the most general case, lines are formed under non-LTE conditions and the level population equation must be solved in order to properly model the line properties as a function of quantum level (n).

Following e.g. Seaton (1959a) and Brocklehurst (1970), we present the results of our modeling in terms of the departure coefficients (b_{nl}), defined by:

$$b_{nl} = \frac{N_{nl}}{N_{nl}(LTE)}, \quad (4.4)$$

and b_n values are computed by taking the weighted sum of the b_{nl} values:

$$b_n = \sum_{l=0}^{n-1} \left(\frac{2l+1}{n^2} \right) b_{nl}, \quad (4.5)$$

note that, at a given n, the b_{nl} values for large l levels influence the final b_n value the most due to the statistical weight factor. At low frequencies stimulated emission is important (Goldberg, 1966) and we introduce the correction factor for stimulated emission as defined by Brocklehurst and Seaton (1972):

$$\beta_{n,n'} = \frac{1 - (b_{n'}/b_n)\exp(-h\nu/kT_e)}{1 - \exp(-h\nu/kT_e)}, \quad (4.6)$$

unless otherwise stated the β_n presented here correspond to α transitions ($n' = n+1 \rightarrow n$). The description of the level population in terms of departure coefficients is convenient as it reduces the level population problem to a more easily handled problem as we will show in Section 4.2.1.

4.2.1 Level Population of Carbon Atoms under Non-LTE Conditions

The observations of high n carbon recombination lines in the ISM motivated Watson et al. (1980) to study the effect on the level population of dielectronic

[2] $\Lambda(T_e)^3 \approx 4.14133 \times 10^{-16}\ T_e^{-1.5}$ cm^3.

recombination [3] and its inverse process (autoionization) in low temperature ($T_e \lesssim 100$ K) gas. Watson et al. (1980) used l-changing collision rates [4] from Jacobs and Davis (1978) and concluded that for levels $n \approx 250 - 300$, dielectronic recombination of carbon ions can be of importance. In a later work, Walmsley and Watson (1982a) used collision rates from Dickinson (1981) and estimated a value for which autoionization becomes more important than angular momentum changing rates. The change in collision rates led them to conclude that the influence of dielectronic recombination on the b_n values is important at levels $n \gtrsim 300$. Clearly, the results are sensitive to the choice of the angular momentum changing rates. Here, we will explicitly consider l-sublevels when solving the level population equation.

The dielectronic recombination and autoionization processes affect only the C+ ions in the $^2P_{3/2}$ state, therefore we treat the level population for the two ion cores in the $^2P_{1/2}$ separately in the evaluation of the level population (Walmsley and Watson, 1982a). The equations for carbon atoms recombining to the $^2P_{3/2}$ ion core population have to include terms describing dielectronic recombination (α^d_{nl}) and autoionization (A^a_{nl}), viz.:

$$b_{nl}\left[\sum_{n'<n}\sum_{l'=l\pm1} A_{nln'l'} + \sum_{n'\neq n}(B_{nln'l'}I_\nu + C_{nln'l'}) + \sum_{l'=l\pm1} C_{nlnl'} + A^a_{nl} + C_{nl,i}\right] =$$
$$\sum_{n'>n}\sum_{l'=l\pm1} b_{n'l'}\frac{\omega_{n'l'}}{\omega_{nl}}e^{\Delta\chi_{n'n}}A_{n'l'nl} + \sum_{n'\neq n}\sum_{l'=l\pm1} b_{n'l'}\frac{\omega_{n'l'}}{\omega_{nl}}e^{\Delta\chi_{n'n}}(B_{n'l'nl}I_\nu + C_{n'l'nl}) +$$
$$+\sum_{l'=l\pm1} b_{nl'}\left(\frac{\omega_{nl'}}{\omega_{nl}}\right)C_{nl'nl} + \frac{N_eN^+_{3/2}}{N_{nl}(LTE)}(\alpha_{nl} + C_{i,nl}) + \frac{N_eN^+_{1/2}}{N_{nl}(LTE)}\alpha^d_{nl}. \quad (4.7)$$

The left hand side of Equation 4.7 describes all the processes that take an electron out of the nl-level, and the right hand side the processes that add an electron to the nl level; $A_{nln'l'}$ is the coefficient for spontaneous emission, $B_{nln'l'}$ is the coefficient for stimulated emission or absorption induced by a radiation field I_ν; $C_{nln'l'}$ is the cross section for energy changing collisions (i.e. transitions with $n \neq n'$), $C_{nlnl'}$ is the coefficient for l-changing collisions; $C_{nl,i}$ ($C_{i,nl}$) is the coefficient for collisional ionization (3-body recombination) and α_{nl} is the coefficient for radiative recombination. A description of the coefficients entering in Equation 4.7 is given in Section 4.2.3 and in further detail in the Appendix. The level population equation is solved by finding the values for the departure coefficients. The level population for carbon ions recombining to the

[3] Recombination to a high n state accompanied by the simultaneous excitation of the $^2P_{1/2}$ C+ electron to the $^2P_{1/2}$ state.

[4] We use the term l-changing collision rates to refer to collisions rate that induce a transition from state nl to $nl \pm 1$

$^2P_{1/2}$ level is hydrogenic and we solve for the departure coefficients ($b_{nl}^{1/2}$) using Equation 4.7, but ignoring the coefficients for dielectronic recombination and autoionization.

After computing the $b_{nl}^{1/2}$ and $b_{nl}^{3/2}$, we compute the departure coefficients ($b_n^{1/2}$ and $b_n^{3/2}$) for both parent ion populations by summing over all l-states (Equation 4.5). The final departure coefficients for carbon are obtained by computing the weighted average of both ion cores:

$$b_n^{final} = \frac{b_n^{1/2} + b_n^{3/2}\left[N_{3/2}^+/N_{1/2}^+\right]}{1+\left[N_{3/2}^+/N_{1/2}^+\right]}. \tag{4.8}$$

Note that, in order to obtain the final departure coefficients, the relative population of the parent ion cores is needed. Here, we assume that the population ratio of the two ion cores $N_{3/2}^+$ to $N_{1/2}^+$ is determined by collisions with electrons and hydrogen atoms. This ratio can be obtained using (Ponomarev and Sorochenko, 1992; Payne et al., 1994):

$$R = \frac{N_{3/2}^+/N_{1/2}^+}{N_{3/2}^+(LTE)/N_{1/2}^+(LTE)} \tag{4.9}$$

$$= \frac{N_e\gamma_e + N_H\gamma_H}{N_e\gamma_e + N_H\gamma_H + A_{3/2,1/2}}, \tag{4.10}$$

where $\gamma_e = 4.51\times10^{-6}\ T_e^{-1/2}$ cm^{-3} s^{-1} is the de-excitation rate due to collisions with electrons, $\gamma_H = 5.8\times10^{-10}\ T_e^{0.02}$ cm^{-3} s^{-1} is the de-excitation rate due to collisions with hydrogen atoms (Payne et al., 1994) [5], $N_{\rm H}$ is the atomic hydrogen density and $A_{3/2,1/2} = 2.4\times10^{-6}$ s^{-1} is the spontaneous radiative decay rate of the core. In this work, we have ignored collisions with molecular hydrogen, which should be included for high density PDRs. Collisional rates for H_2 excitation of C^+ have been calculated by Flower (1988). In the cases of interest here, the value of R is dominated by collisions with atomic hydrogen. We recognize that the definition of R given in Equation 4.9 is related to the critical density (N_{cr}) of a two level system by $R = 1/(1+N_{cr}/N_X)$ where N_X is the density of the collisional partner (electron or hydrogen). The LTE ratio of the ion core is given by the statistical weights of the levels and the temperature

[5]Payne et al. (1994) used rates from Tielens and Hollenbach (1985), based on Launay and Roueff (1977) for collisions with hydrogen atoms and Hayes and Nussbaumer (1984) for collisions with electrons. Newer rates are available for collisions with electrons (Wilson and Bell, 2002) and hydrogen atoms (Barinovs et al., 2005), but the difference in values is negligible.

(T_e) of the gas:

$$\frac{N^+_{3/2}(LTE)}{N^+_{1/2}(LTE)} = \frac{g_{3/2}}{g_{1/2}} e^{-\Delta E/kT_e}, \tag{4.11}$$

where $g_{3/2} = 4,\ g_{1/2} = 2$ are the statistical weights of the fine structure levels and $\Delta E = 92$ K is the energy difference of the fine structure transition. The LTE level population ratio as a function of temperature is shown in Figure 4.1, illustrating the strong dependence on temperature of this value. At densities below the critical density (≈ 300 cm^{-3} for collisions with H), the fine structure levels fall out of LTE and the value for R becomes very small (Figure 4.1). Note that R is not very sensitive to the temperature.

With the definition of R given above, the final departure coefficient can be written as (Ponomarev and Sorochenko, 1992):

$$b_n^{final} = \frac{b_n^{1/2} + b_n^{3/2} R \left[N^+_{3/2}/N^+_{1/2}\right]_{LTE}}{1 + R \left[N^+_{3/2}/N^+_{1/2}\right]_{LTE}}. \tag{4.12}$$

The final departure coefficient is the value that we are interested in to describe CRRLs.

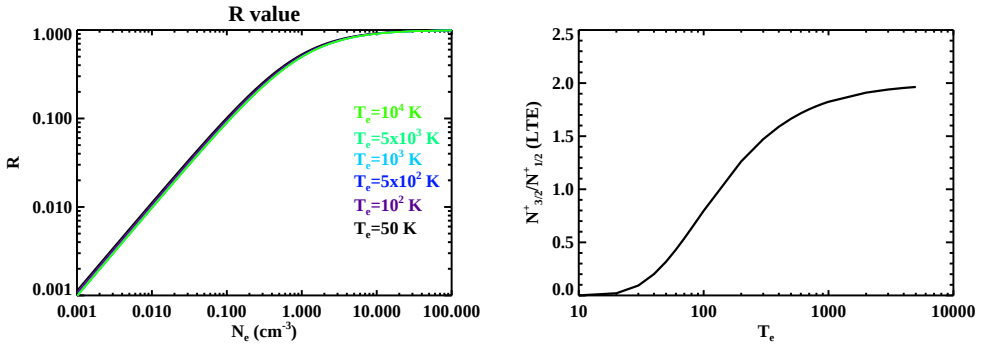

Figure 4.1: Left panel: R value as a function of electron temperature, in a range of densities. The R value is nearly independent of temperature, and for $N_e > 10$ cm^{-3}, $R \approx 1$. Right panel: ion "LTE" ratios as a function of T_e, independent of density.

4.2.2 Numerical Method

Having described how to derive the b_n^{final}, now we focus on the problem of obtaining the departure coefficients for both ion cores from the level population

equation. We use the same procedure to obtain the departure coefficients for both parent ion cores, as the only difference in the level population equation for the $^2P_{3/2}$ and the $^2P_{1/2}$ cores is the inclusion of dielectronic recombination and autoionization processes. We will refer as b_{nl} and b_n without making a distinction between the $^2P_{3/2}$ and $^2P_{1/2}$ in this subsection.

We follow the methods described in Brocklehurst (1971) and improved in Hummer and Storey (1987) to solve the level population equation in an iterative manner. First, we solve the level population equation by assuming that the l sublevels are in statistical equilibrium, i.e. $b_n = b_{nl}$ for all l sublevels. We refer to this approach as the n-method (see Appendix B). Second, we used the previously computed values to determine the coefficients on the right hand side of Equation 4.7 that contain terms with $n' \neq n$. Thus, the level population equation for a given n is a tridiagonal equation on the l sublevels involving terms of the type $l \pm 1$. This tridiagonal equation is solved for the b_{nl} values (further details are given in Appendix B). The second step of this procedure is repeated until the difference between the computed departure coefficients is less than 1%.

We consider a fixed maximum number of levels, n_{max}, equal to 9900. We make no explicit assumptions on the asymptotic behavior of the b_n for larger values of n. Therefore, no fitting or extrapolation is required for large n. The adopted value for n_{max} is large enough for the asymptotic limit – $b_n \to 1$ for $n > n_{max}$ – to hold even at the lowest densities considered here. For the nl-method, we need to consider all l sublevels up to a high level ($n \sim 1000$). For levels higher than this critical n level (n_{crit}), we assume that the l sublevels are in statistical equilibrium. In our calculations $n_{crit} = 1500$, regardless of the density.

4.2.3 Rates Used in this Work

In this section, we provide a brief description of the rates used in solving the level populations. Further details and the mathematical formulations for each rate are given in Appendices C, D, E and F. Accurate values for the rates are critical to obtain meaningful departure coefficients when solving the level population equation (Equation 4.7). Radiative rates are known to high accuracy ($< 1\%$) as they can be computed from first principles. On the other hand, collision rates at low temperatures are more uncertain ($\sim 20\%$, Vriens and Smeets 1980).

4.2.3.1 Einstein A and B coefficient

The Einstein coefficients for spontaneous and stimulated transitions can be derived from first principles. We used the recursion formula described in Storey

and Hummer (1991) to obtain the values for the Einstein $A_{nln'l'}$ coefficients. To solve the n method (our first step in solving the level population equation) we require the values for $A_{nn'}$, which can be easily obtained by summing the $A_{nln'l'}$:

$$A_{nn'} = \frac{1}{n^2}\sum_{l'=0}^{n-1}\sum_{l=l'\pm1}(2l+1)A_{nln'l'}. \tag{4.13}$$

The mathematical formulation to obtain values for spontaneous transitions is detailed in Appendix C.

The coefficients for stimulated emission and absorption ($B_{nn'}$) are related to the $A_{nn'}$ coefficients by:

$$B_{nn'} = \frac{c^2}{2h\nu^3}A_{nn'}, \tag{4.14}$$

$$B_{n'n} = \left(\frac{n}{n'}\right)^2 B_{nn'}. \tag{4.15}$$

4.2.3.2 Energy changing collision rates

In general, energy changing collisions are dominated by the interactions of electrons with the atom. The interaction of an electron with an atom can induce transitions of the type:

$$X_{nl} + e^- \rightleftarrows X_{n'l'} + e^-, \tag{4.16}$$

with $n' \neq n$ changing the distribution of electrons in an atom population. Hummer and Storey (1987) used the formulation of Percival and Richards (1978). The collision rates derived by Percival and Richards (1978) are essentially the same as Gee et al. (1976). However, the collision rates from Gee et al. (1976) are not valid for the low temperatures of interest here. Instead, we use collision rates from Vriens and Smeets (1980). We note that at high T_e and for high n levels, the Bethe (Born) approximation holds and values of the rates from Vriens and Smeets (1980) differ by less than 20% when compared to those from Gee et al. (1976). The good agreement between the two rates is expected since the results from Vriens and Smeets (1980) are based on Gee et al. (1976). On the other hand, at low T_e and for low n levels values the two rates differ by several orders of magnitude and, indeed, the Gee et al. (1976) values are too high to be physically realistic. A comparison of the rates for different values of T_e and $n \rightarrow n + \Delta n$ transitions is shown in Figure 4.2. We explore the effects of using Vriens and Smeets (1980) rates on the b_n values in Section 4.3.2.

The inverse rates are obtained from detailed balance:

$$C_{n'n} = \left(\frac{n}{n'}\right)^2 e^{\chi_n - \chi_{n'}} C_{nn'}. \tag{4.17}$$

In order to solve the nl-method, rates of the type $C_{nln'l'}$ with $n \neq n'$ are needed. Here, the approach of Hummer and Storey (1987) is followed and the collision rates are normalized by the oscillator strength of the transitions (Equation 5 in Hummer and Storey 1987). Only transitions with $\Delta l = 1$ were included as these dominate the collision process (Hummer and Storey, 1987),.

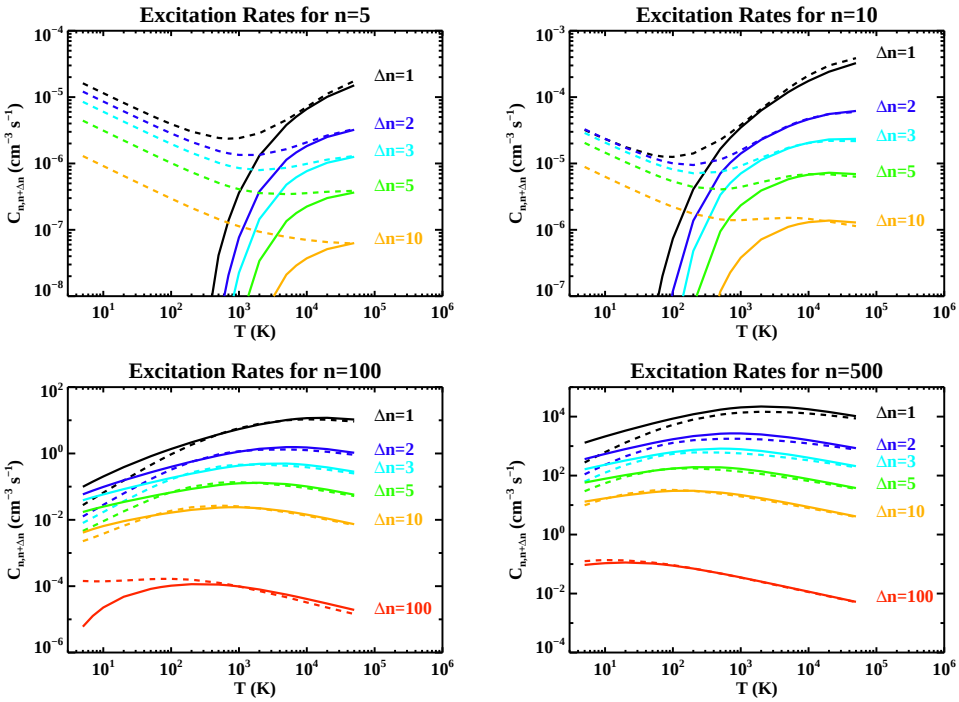

Figure 4.2: Comparison of energy changing collision rates. The dashed lines correspond to the Gee et al. (1976) rates while the solid lines are from Vriens and Smeets (1980). Large differences between Gee et al. (1976) and Vriens and Smeets (1980) can be seen at low T_e and at low n levels. As is well known, transitions with $\Delta n = 1$ dominate. The difference between $\Delta n > 1$ and $\Delta n = 1$ rates is less at lower T_e.

4.2.3.3 Angular momentum changing collision rates

For low n levels, the l level population has to be explicitly calculated. Moreover, for the dielectronic recombination process, the angular momentum changing collisions set the value for which the dielectronic recombination process is important, and transitions of the type:

$$X_{nl} + \mathrm{C}^{+} \rightleftarrows X_{nl\pm1} + \mathrm{C}^{+} \tag{4.18}$$

must be considered. In general, collisions with ions are more important than collisions with electrons. Here, for simplicity, we adopt that C^+ is the dominant cation.

Hummer and Storey (1987) used l-changing collision rates from Pengelly and Seaton (1964) which are computed iteratively for a given n level starting at $l = 0$ or $l = n - 1$. However, as pointed out by Hummer and Storey (1987) and Brocklehurst (1971), the values for the l-changing rates obtained by starting the iterations at $l = 0$ differ from those obtained when starting at $l = n-1$. Moreover, averaging the l-changing rates obtained by the two different initial conditions leads to an oscillatory behavior of the rates that depends on l (Brocklehurst, 1970). Hummer and Storey (1987) circumvented this problem by normalizing the value of the rates by the oscillator strength (Equation 4 in Hummer and Storey 1987). In addition, at high n levels and high densities the values for $C_{nln'l'}$ can become negative (Equation 43 in Pengelly and Seaton 1964). This poses a problem when studying the level population of carbon atoms at the high n levels of interest in the present work[6]. The more recent study of Vrinceanu et al. (2012) provides a general formulation to obtain the value of l-changing transition rates. These new rates use a better approximation for the cut-off radius of the probability of the transition. Furthermore, the rates from Vrinceanu et al. (2012) are well behaved over a large range of temperature and densities and they do not exhibit the oscillatory behavior with l sublevel shown by the Pengelly and Seaton (1964) rates. Therefore, we use the Vrinceanu et al. (2012) rates in this work. Vrinceanu et al. (2012) derived the following expression, valid for $n > 10$ and $n\sqrt{T_e} < 2.4 \times 10^4$ K$^{1/2}$:

$$C_{nl\rightarrow nl+1} = 24\sqrt{\pi}a_0^3\pi cRyn^4\sqrt{\left(\frac{hcRy}{kT_e}\right)\left(\frac{\mu}{m_e}\right)}\left[1-\left(\frac{l}{n}\right)^2\left(\frac{2l+3}{2l+1}\right)\right].$$

where a_0 is the bohr radius and μ is the reduced mass of the system. Values for the inverse process are obtained by using detailed balance:

$$C_{nl+1\rightarrow nl} = \frac{(2l+1)}{(2l+3)}C_{nl\rightarrow nl+1}. \tag{4.19}$$

We note that the l-changing collision rates obtained by using the formula from Vrinceanu et al. (2012) can differ by orders of magnitude with those using Pengelly and Seaton (1964) formulation. We discuss the effect on the final b_n values in Section 4.3.2, where we compare our results with those of Storey and Hummer (1995).

[6]We note that this was not a problem for Hummer and Storey (1987), since they assumed an statistical distribution of the l levels for high n.

4.2.3.4 Radiative Recombination

Radiative ionization occurs when an excited atom absorbs a photon with enough energy to ionize the excited electron. The process can be represented as follows:

$$X_{nl} + h\nu \rightleftarrows X^+ + e^-, \tag{4.20}$$

and the inverse process is radiative recombination. We use the recursion relation described in Storey and Hummer (1991) to obtain values for the ionization cross-section (Appendix D). Values for the radiative recombination (α_{nl}) coefficients were obtained using the Milne relation and standard formulas (e.g. Rybicki and Lightman (1986), Appendix D). The program provided by Storey and Hummer (1991) only produces reliable values up to $n \sim 500$ due to cancellation effects in the iterative procedure. In order to avoid cancellation effects, the values computed here were obtained by working with logarithmic values in the recursion formula. As expected, our values for the rates match those of Storey and Hummer (1991) well.

For the n-method we require the sum of the individual α_{nl} values:

$$\alpha_n = \sum_{l=0}^{n-1} \alpha_{nl}. \tag{4.21}$$

The averaged α_n values agree well with the approximated formulation of Seaton (1959a) to better than 5%, validating our approach.

4.2.3.5 Collisional ionization and 3-body recombination

Collisional ionization occurs when an atom encounters an electron and, due to the interaction, a bound electron from the atom is ionized. Schematically the process can be represented as:

$$X_n + e^- \quad \rightleftarrows \quad X^+ + e^- + e^-. \tag{4.22}$$

The inverse process is given by the 3-body recombination and the value for the 3-body recombination rate is obtained from detailed balance:

$$\begin{aligned} C_{i,n} &= \frac{N_n(LTE)}{N_{ion}N_e} C_{n,i}, \\ &= \left(\frac{h^2}{2\pi m_e kTe}\right)^{3/2} n^2 e^{\chi_n} C_{n,i}, \\ &= \Lambda(T_e)^3 n^2 e^{\chi_n} C_{n,i}. \end{aligned} \tag{4.23}$$

We used the formulation of Brocklehurst and Salem (1977) and compared the values with those from the formulation given by Vriens and Smeets (1980). For levels above 100 and at $T_e = 10$ K, the Brocklehurst & Salem values are a factor of $\lesssim 2$ larger, but the differences quickly decrease for higher temperatures. To obtain the $C_{nl,i}$ that are needed in the *nl*-method, we followed Hummer and Storey (1987) and assumed that the rates are independent of the angular momentum. The mathematical formulation is reproduced in the Appendix F for convenience of the reader.

4.2.3.6 Dielectronic Recombination and Autoionization on Carbon Atoms

The dielectronic recombination process involves an electron recombining into a level n while simultaneously exciting one of the bound electrons (left side of Equation 4.24, below). This state (X_n^*) is known as an autoionizing state. In this autoionizing state, the atom can stabilize either by releasing the recombined electron through autoionization (inverse process of dielectronic recombination) or through radiative stabilization (right hand side of Equation 4.24). Dielectronic recombination and autoionization are only relevant for atoms with more than one electron.

$$X^+ + e^- \rightleftarrows X_{nl}^* \rightarrow X_{n'l'} + h\nu. \tag{4.24}$$

For C^+ recombination, at $T_e \sim 100$ K free electrons in the plasma can recombine to a high n level, and the kinetic energy is transfered to the core of the ion, producing an excitation of the $^2P_{1/2} - {}^2P_{3/2}$ fine-structure level of the C^+ atom core [7] (which has a difference in energy $\Delta E = 92$ K). Due to the long radiative lifetime of the fine-structure transition (4×10^6 s), radiative stabilization can be neglected.

The autoionization rate, A_{nl}^a, was obtained from the approximate expression given in Dickinson (1981):

$$A_{nl}^a = 2.25 \frac{2\pi Ryc}{n^3 \left(0.5 + l\right)^6}. \tag{4.25}$$

The dielectronic recombination rate is obtained by detailed balance:

$$N_{1/2}^+ N_e \alpha_{nl}^d = N_{nl} A_{nl}^a. \tag{4.26}$$

Walmsley and Watson (1982a) defined b_{di} as the departure coefficient when

[7] The process has been referred in the literature as dielectronic-like recombination or dielectronic capture by Watson et al. (1980).

autoionization/dielectronic recombination dominate:

$$\begin{aligned} b_{di} &= \frac{g_{1/2}N^+_{1/2}}{g_{3/2}N^+_{3/2}} \exp\left[-\Delta E/kT_e\right], \\ &= \frac{1}{R}. \end{aligned} \tag{4.27}$$

4.3 Results

The behavior of CRRLs with frequency depends on the level population of carbon via the departure coefficients. We compute departure coefficients for carbon atoms by solving the level population equation using the rates described in Section 4.2.3 and the approach in Section 4.2.2. Here, we present values for the departure coefficients and provide a comparison with earlier studies in order to illustrate the effect of our improved rates and numerical approach. A detailed analysis of the line strength under different physical conditions relevant for the diffuse clouds and the effects of radiative transfer are provided in an accompanying article (Paper II).

4.3.1 Departure Coefficient for Carbon Atoms

The final departure coefficients for carbon atoms (i.e. b_n^{final}) are obtained by computing the departure coefficients recombining from both parent ions, those in the $^2P_{1/2}$ level and those in the $^2P_{3/2}$ level. Therefore, it is illustrative to study the individual departure coefficients for the $^2P_{1/2}$ core, which are hydrogenic, and the departure coefficients for the $^2P_{3/2}$ core separately.

4.3.1.1 Departure Coefficient in the Hydrogenic Approximation

In Figure 4.3 we show example b_n and $b_n\beta_n$ values obtained in the hydrogenic approximation at $T_e = 10^2$ and 10^4 K for a large range in density. The behavior of the b_n values as a function of n can be understood in terms of the rates that are included in the level population equation. At the highest n levels, collisional ionization and three body recombination dominate the rates in the level population equation and the b_n values are close to unity. We can see that as the density increases, collisional equilibrium occurs at lower n levels and the b_n values approach unity at lower levels. In contrast, for the lowest n levels, the level population equation is dominated by radiative processes and the levels drop out of collisional equilibrium. As the radiative rates increase with decreasing n level, the departure coefficients become smaller. We note that differences in the departure coefficients for the low n levels for different

temperatures are due to the radiative recombination rate, which has a $T_e^{-3/2}$ dependence.

At intermediate n levels, the behavior of the b_n as a function of n shows a more complex pattern with a pronounced "bump" in the b_n values for intermediate levels ($n \sim 10$ to ~ 100). To guide the discussion we refer the reader to Figure 4.3. Starting at the highest n, $b_n \to 1$, as mentioned above. For these high n levels, l-changing collisions efficiently redistribute the electron population among the l states and, at high density, the b_{nl} departure coefficients are unity as well (Figure 4.4, upper panels). For lower values of n, the b_n values decrease due to an increased importance of spontaneous transitions. At these n levels, the b_n values obtained by the nl method differ little from the values obtained by the n-method, since l-changing collisions efficiently redistribute the electrons among the l sublevels for a given n level. For lower n levels, the effects of considering the l sublevel distribution become important as l-changing collisions compete with spontaneous decay, effectively "storing" electrons in high l sublevels for which radiative decay is less important. Specifically, the spontaneous rate out of a given level is approximately $A_{nl} \simeq 10^{10}/n^3/l^2(\mathrm{s}^{-1})$, and is higher for lower l sublevels. Thus, high-l sublevels are depopulated more slowly relative to lower l sublevels on the same n level. This results in a slight increase in the departure coefficients. Reflecting the statistical weight factor in Equation 4.5, the higher l sublevels dominate the final b_n value resulting in an increase in the final b_n value. As the density increases, the l sublevels approach statistical distribution faster. As a result, the influence of the l sublevel population on the final b_n is larger for lower densities than for higher densities at a given T_e. The interplay of the rates produce the "bump" which is apparent in the b_n distribution (Figure 4.3)

The influence of l-changing collisions on the level populations and the resulting increase in the b_n values was already presented by Hummer and Storey (1987) and analyzed in detail by Strelnitski et al. (1996) in the context of hydrogen masers. The results of our level population models are in good agreement with those provided by Hummer and Storey (1987) as we show in Section 4.3.2.

4.3.1.2 Departure Coefficient for Carbon Atoms Including Dielectronic Recombination

Only carbon atoms recombining to the $^2P_{3/2}$ ion core are affected by dielectronic recombination. Having analyzed the departure coefficients for the hydrogenic case, we focus now on the $b_{nl}^{3/2}$ values and the resulting b_n^{final} as introduced in Section 4.2.1.

Figure 4.5 show example values for $b_n^{3/2}$ for $T_e = 50,\ 100,\ 200$ and $1000\ K$ and electron densities between 10^{-3} and 10^2 cm^{-3}. As pointed out by Watson

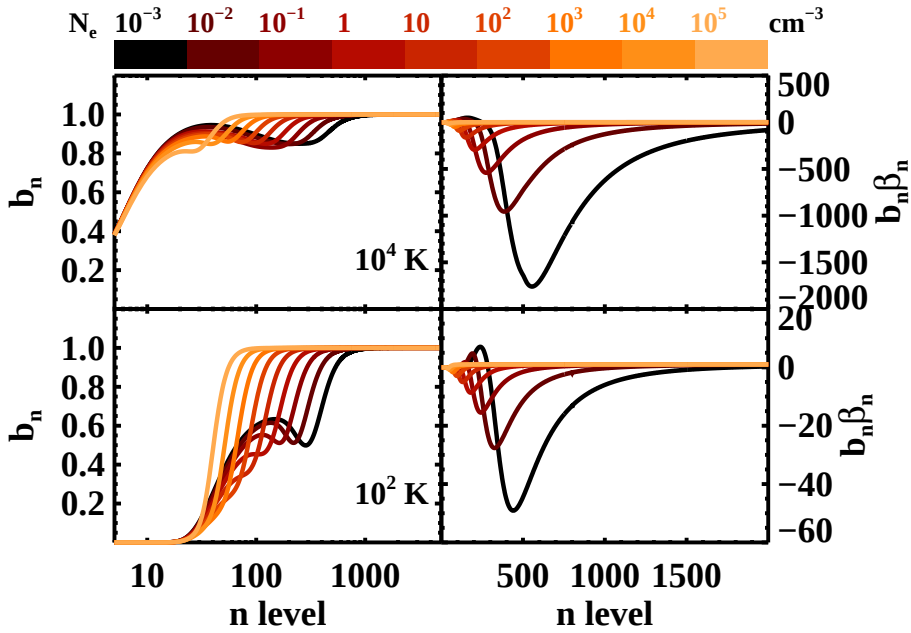

Figure 4.3: b_n values (left) and $b_n\beta_n$ values (right) for hydrogen at $T_e = 10^4$ and 10^2 K (upper and lower panels, respectively) for different densities (N_e, colorscale). The departure coefficients obtained using the nl-method show a "bump" at low n levels. The strength and position of the "bump" depend on the physical conditions. As density increases, the l-changing collisions redistribute the electron population more effectively.

et al. (1980), the low lying l sublevels are dominated by the dielectronic process and the $b_{nl}^{3/2}$ values are equal to b_{di} (Equation 4.27). As can be seen in Figure 4.1, such values can be much larger than unity at low densities resulting in an overpopulation of the low n levels for the 3/2 ion cores. In Figure 4.6 we show b_n^{final} as a function of n level under the same conditions. We see that at high electron densities the departure coefficients show a similar behavior as the hydrogenic values. Furthermore, an increase in the level population to values larger than unity is seen at low densities and moderate to high temperatures.

To guide the discussion, we analyze the behavior of the b_n^{final} when autoionization/dielectronic recombination dominates. This occurs at different levels depending on the values of T_e and N_e considered. Nevertheless, it is instructive to understand the behavior of the level population in extreme cases. When autoionization/dielectronic recombination dominate, the b_n^{final} in Equation 4.12

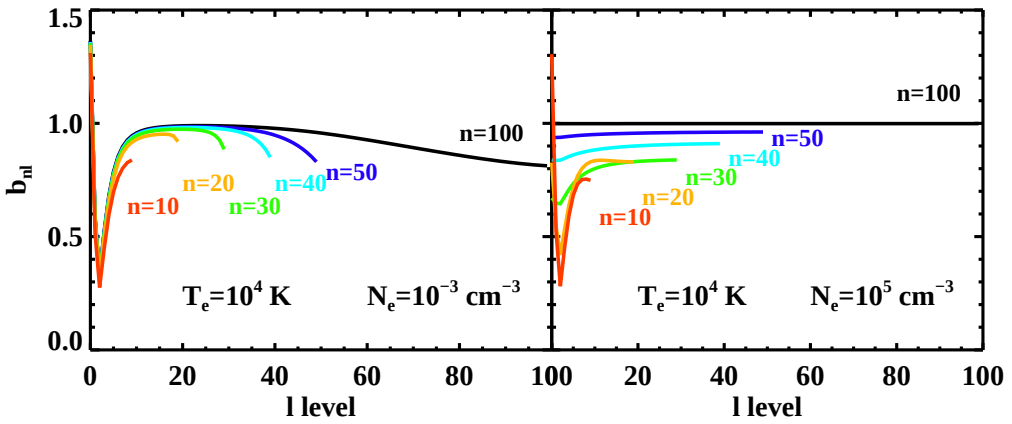

Figure 4.4: Example of hydrogenic b_{nl} values at low densities (*Left panel*) and high densities (*Right panel*). Statistical distribution of the l-sublevels is attained at levels as low as ~ 40. For lower levels, radiative processes dominate the level population. At low density (*Left panel*), radiative processes dominate even at high n levels.

is given by:

$$b_n^{final} \approx \frac{b_n^{1/2} + \left[N^+_{3/2}/N^+_{1/2}\right]_{LTE}}{1 + R\left[N^+_{3/2}/N^+_{1/2}\right]_{LTE}}. \tag{4.28}$$

At high densities, R approaches unity and we note two cases. The first case is when T_e is high, the maximum value of $\left[N^+_{3/2}/N^+_{1/2}\right]_{LTE} = 2$, meaning that a large fraction of the ions are in the $^2P_{3/2}$ core. Consequently, $b_n^{final} \approx (b_n^{1/2} + 2)/3$, thus the effect of dielectronic recombination is to increase the level population as compared to the hydrogenic case. We also note that since $b_n^{1/2} \leq 1$ the final $b_n^{final} \leq 1$. The second case we analyze is for low T_e, where

the ion LTE ratio is low and most of the ions are in the $^2P_{1/2}$ core. Thus, $b_n^{final} \approx b_n^{1/2}$ and the departure coefficients are close to hydrogenic.

At low densities, $R \ll 1$ and, as above, we study two cases. The first is when T_e is high, the maximum value of $\left[N^+_{3/2}/N^+_{1/2}\right]_{LTE} = 2$ and $b_n^{final} \approx b_n^{1/2} + 2$, therefore dielectronic recombination produces a large overpopulation as compared to the hydrogenic case. The second case is when T_e is low and most of the ions are in the $^2P_{1/2}$ level and, as in the high density case, the $b_n^{final} \approx b_n^{1/2}$. We note from this analysis that overpopulation of the b_n^{final} (relative to the hydrogenic case) is only possible for a range of temperatures and densities. In particular, b_n^{final} is maximum for high temperatures and low densities.

Having analyzed the behavior of the b_n^{final} values in the extreme $b_n^{3/2} = b_{di}$ case, now we analyze the behavior of $b_n^{3/2}$ with n. The population in the low n levels is dominated by dielectronic recombination (Watson et al., 1980; Walmsley and Watson, 1982a) and $b_n^{3/2} = b_{di}$ up until a certain n level where $b_n^{3/2}$ begins to decrease down to a value of one. The n value where this change happens depends on temperature, moving to higher n levels as T_e decreases. To understand this further, we analyze the rates involved in the l sublevel population (Figure 4.5). The low l sublevels are dominated by dielectronic recombination and autoionization and the b_{nl} values for the 3/2 ion cores are $b_{nl}^{3/2} = b_{di}$. For the higher l sublevels other processes (mainly collisions) populate or depopulate electrons from the level n and the net rate is lower than that of the low l dielectronic recombination/autoionization. This lowers the b_{nl} value, which is effectively delayed by l-changing collisions since they redistribute the population of electrons in the n level. The b_{nl} for highest l values dominate the value of $b_n^{3/2}$ due to the statistical weight factor.

We note that the behavior of the $b_n^{3/2}$ cores as a function of n (see Figure 4.7) can be approximated by:

$$b_n^{3/2} \approx \tanh\left(\left[\frac{l_m}{n}\right]^3\right) \times (b_{di} - 1) + 1. \tag{4.29}$$

with b_{di} defined as in Walmsley and Watson (1982a) (Equation 4.27) and l_m was derived from fitting our results:

$$l_m \approx 60 \times \left(\frac{N_e}{10}\right)^{-0.02} \left(\frac{T_e}{10^4}\right)^{-0.25} \tag{4.30}$$

In diffuse clouds the integrated line to continuum ratio is proportional to $b_n\beta_n$. We note that the β_n behavior is more complex as can be seen in Figure 4.8. The low n "bump" on the b_n^{final} makes the $b_n\beta_n$ high at low densities

and for levels between about 150 and 300. Since the b_n^{final} values decrease from values larger than one to approximately one, the β_n changes sign. In Figure 4.9 we show the electron density as a function of the level where the change of sign on the $b_n\beta_n$ occurs. At temperatures higher than about 200, our models for $N_e = 0.1$ cm^{-3} show no change of sign due to the combined effects of l-changing collisions and dielectronic recombination.

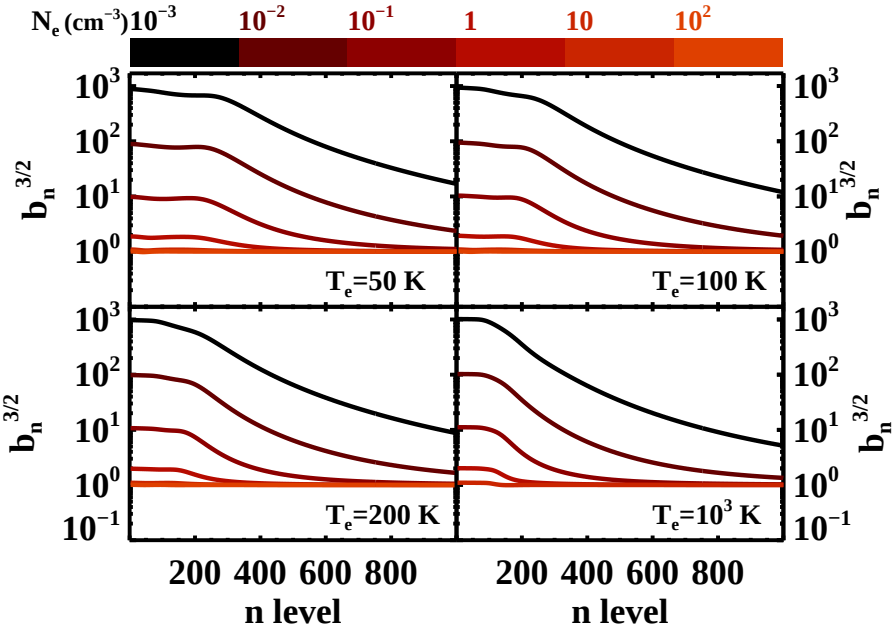

Figure 4.5: Departure coefficients for the $^2P_{3/2}$ parent ions as a function of n at $T_e = 50,\ 100,\ 200$ and 1000 K for different densities (N_e, colorscale). The values for low n levels are close to b_{di} and decrease towards a value of one. At high densities, $b_n^{3/2} \approx 1$.

4.3.2 Comparison with Previous Models

The level population of hydrogenic atoms is a well studied problem. Here, we will describe the effects of the updated collision rates as well as point out differences due to the improved numerical method.

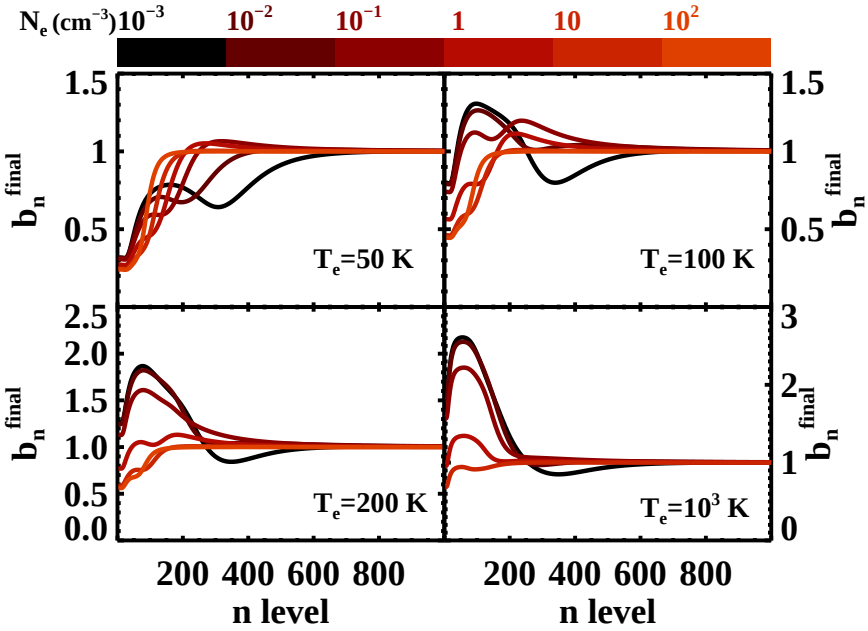

Figure 4.6: Final departure coefficients for carbon atoms (b_n^{final}) as a function of n level at T_e = 50, 100, 200 and 1000 K for different densities (N_e, colorscale). The "bump" seen in hydrogenic atoms is amplified by dielectronic recombination. As density increases the b_n^{final} are closer to the hydrogenic value.

4.3.2.1 Hydrogenic Atoms

At the lowest densities, we can compare our results for hydrogenic atoms with the values of Martin (1988) for Hydrogen atoms. The results of Martin (1988) were obtained in the low density limit, i.e. no collision processes were taken into account in his computations. The results are given in terms of the emissivity of the line normalized by the Hβ emissivity. As can be seen in Figure 4.10, our results agree to better than 5%, and for most levels to better than 0.5%.

At high densities, we compare the hydrogenic results obtained here with those of Hummer and Storey (1987). Our approach reproduces well the b_{nl} (and b_n) values of Hummer and Storey (1987) (to better than 1%) when using the same collision rates (Gee et al., 1976; Pengelly and Seaton, 1964) as can be seen in Figure 4.11. We note that the effect of using different energy changing rates ($C_{n,n'}$) has virtually no effect on the final b_n values. On the other hand, using

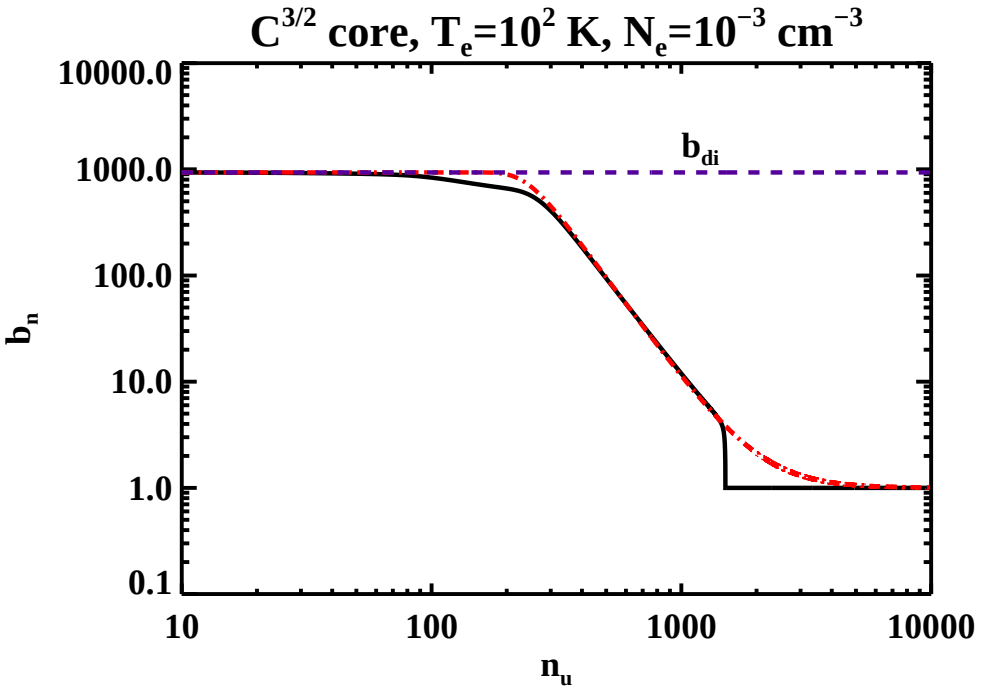

Figure 4.7: $b_n^{3/2}$ values for carbon as a black line (solid), the discontinuity at $n = 1500$ is due to the n_{crit} value. Overplotted as a red (dot dashed) line is the approximation in Equation 4.29. The blue (dashed) line is the value of b_{di}.

Vrinceanu et al. (2012) values for the $C_{nl,nl\pm1}$ rates results in differences in the b_n values of 5% at $T_e = 10^4$ K, $N_e = 100$ cm^{-3}. As expected, the difference is less at higher temperatures and densities since values are closer to equilibrium (see Figure 4.12). At low n levels, our results for high l levels are overpopulated as compared to the values of Hummer and Storey (1987) leading to an increases in the b_n values.

4.3.2.2 Carbon

Now we compare the departure coefficients obtained here with the results of Ponomarev and Sorochenko (1992). We focus the discussion on the b_n values from Ponomarev and Sorochenko (1992) as the Walmsley and Watson (1982a) values are similar. However, Walmsley and Watson (1982a) only present $b_n\beta_n$ plots and the values of β_n are quite sensitive to small changes in b_n. While the results presented here are remarkably different from those of Walmsley and Watson (1982a), some trends are similar.

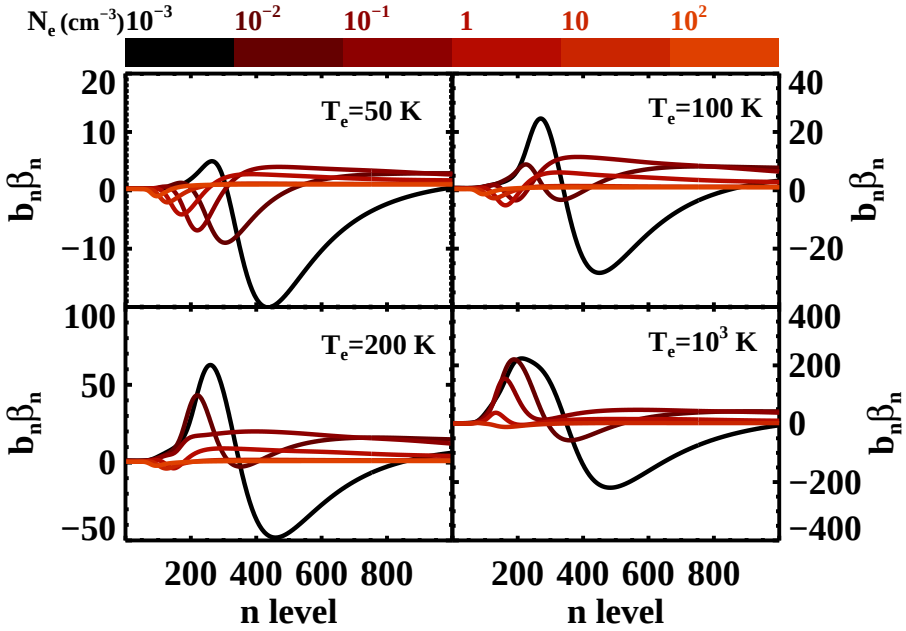

Figure 4.8: $b_n\beta_n$ values for carbon atoms at $T_e = 50,\ 100,\ 200$ and 1000 K for different densities (N_e, colorscale).

We start by comparing the departure coefficient presented here with those from Ponomarev and Sorochenko (1992) for the $T_e = 100$ K and at a density of $N_e = 0.1$ cm^{-3} (Figure 4.13). From the plots in Ponomarev and Sorochenko (1992) and using Equation 4.12 we can estimate the $b_n^{3/2}$ value [8]. At level $n = 100$ they give values of $b_n^{final} \sim 0.7$ and $b_n^{1/2} \sim 0.2$ from which we derive $b_n^{3/2} \sim 7$, which is 30% lower than our value of 10. Close to their peak in the b_n^{final} value, at $n = 400$, we derive from the plots a $b_n^{3/2} \sim 9$, while from our method we obtain a value closer to 3. Finally, at level $n = 900$, $b_n^{3/2} \sim 4$ from Ponomarev and Sorochenko (1992) and this is about a factor of two larger than our value.

The same exercise can be done for $N_e = 1$ cm^{-3}: for $n = 100,\ 300$ and 900 the $b_n^{3/2}$ calculated by Ponomarev and Sorochenko (1992) are $\sim 1.6,\ 1.8$ and 1, respectively. Our $b_n^{3/2}$ values are $\sim 2,\ 1.1$ and 1 for the same levels. At higher

[8] It is difficult to estimate the b_n value from the plots in Ponomarev and Sorochenko (1992) since the scale in their plots is not evenly spaced. We believe this might be due to a misprint and the values for $T_e = 100$ K were taken from Figure 2.35 in Gordon and Sorochenko (2009). For $T_e = 50$ K, we used the plots in Ponomarev and Sorochenko (1992).

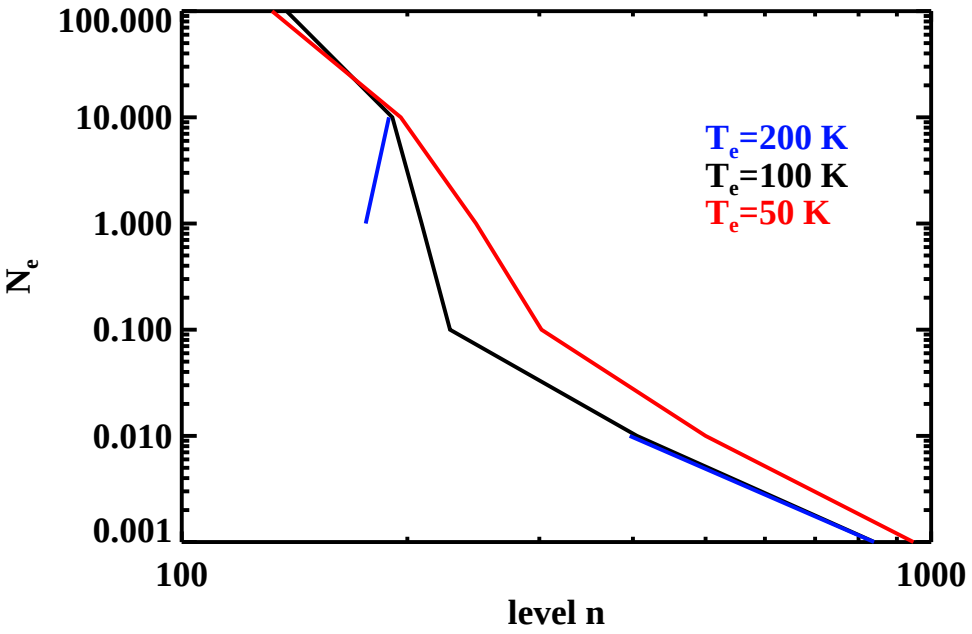

Figure 4.9: Level where the $b_n\beta_n$ values go to zero for $T_e = 50,\ 100$ and 200 K. At temperatures larger than 200 K and for an electron densities around 10^{-1} cm^{-3} the $b_n\beta_n$ values do not go through zero.

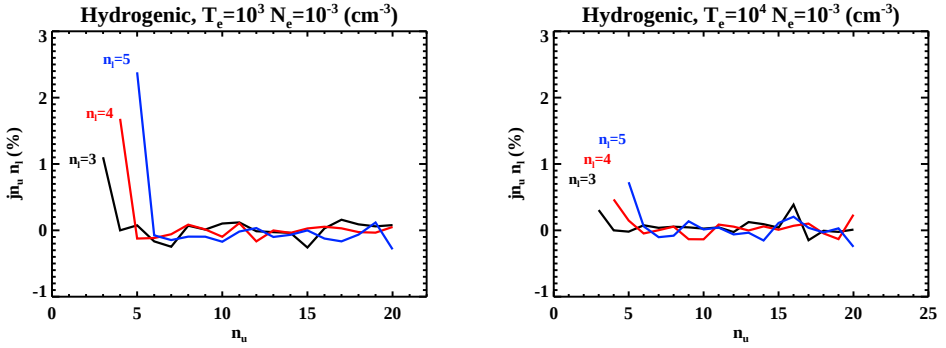

Figure 4.10: Difference between the emissivities (normalized to Hβ) for low nl lines at low density and the results from Martin (1988) in the low N_e approximation. Our results agree to better than 1% at most levels.

densities, our results are similar to the hydrogenic case and agree with Ponomarev and Sorochenko (1992). This is expected, as discussed in Section 4.3.1

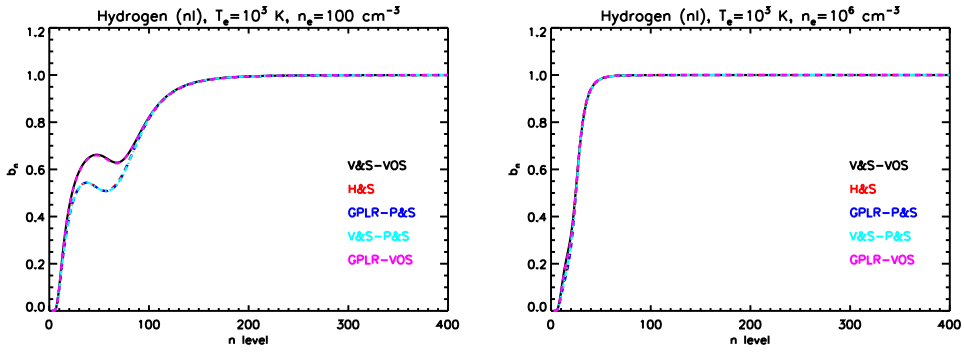

Figure 4.11: A comparison of the effect of different collision rates on the final b_n values for $T_e = 100$ K and $N_e = 100$ and 10^6 cm^{-3}. H&S are the departure coefficients from Hummer and Storey (1987) who used Gee et al. (1976); GPLR corresponds to the use of n changing collision rates from Gee et al. (1976), V&S from Vriens and Smeets (1980); P&S corresponds to the use of l-changing collision rates from Pengelly and Seaton (1964), VOS corresponds to Vrinceanu et al. (2012). The largest differences are $\sim$ 30% due to the use of different l-changing collision rates.

at high densities b_n values approach equilibrium.

At lower temperatures, we analyze the case of $T_e = 50$ K. For $N_e = 0.1$ cm^{-3}, the $b_n^{3/2}$ values derived from the Ponomarev and Sorochenko (1992) plots are: 8, 7, and 3 for levels $n = 100,\ 400$ and 900, respectively (cf. Figure 4.13). The values derived from our models are 10, 7, and 1, for the same levels (Figure 4.5). At $N_e = 1$ cm^{-3}, Ponomarev and Sorochenko (1992) find $\sim 1.6,\ 1.6$ and 1 for these levels and our values are quite similar. As a general trend, our values at $n \approx 100$ are similar to those from Ponomarev and Sorochenko (1992). At this level, dielectronic recombination and autoionization dominate the rates in the level population equation and the $b_n^{3/2}$ are close to b_{di}. At higher levels, the Ponomarev and Sorochenko (1992) values remain close to b_{di} while our values decrease. It seems that the influence of dielectronic processes in Ponomarev and Sorochenko (1992) remain important at higher n levels than in our simulations. We attribute this discrepancy to the use of different collision rates. Indeed, at high densities the differences become smaller since the levels approach collisional equilibrium.

Differences in the b_n^{final} values obtained here and those given in Ponomarev and Sorochenko (1992) produce discrepancies in the β_n values. For high n levels, our values can differ by an order of magnitude when compared to those of Ponomarev and Sorochenko (1992). For example, at level $n = 900$, the $b_n\beta_n$ value from Ponomarev and Sorochenko (1992) is $\sim$ 100 for the $T_e =$

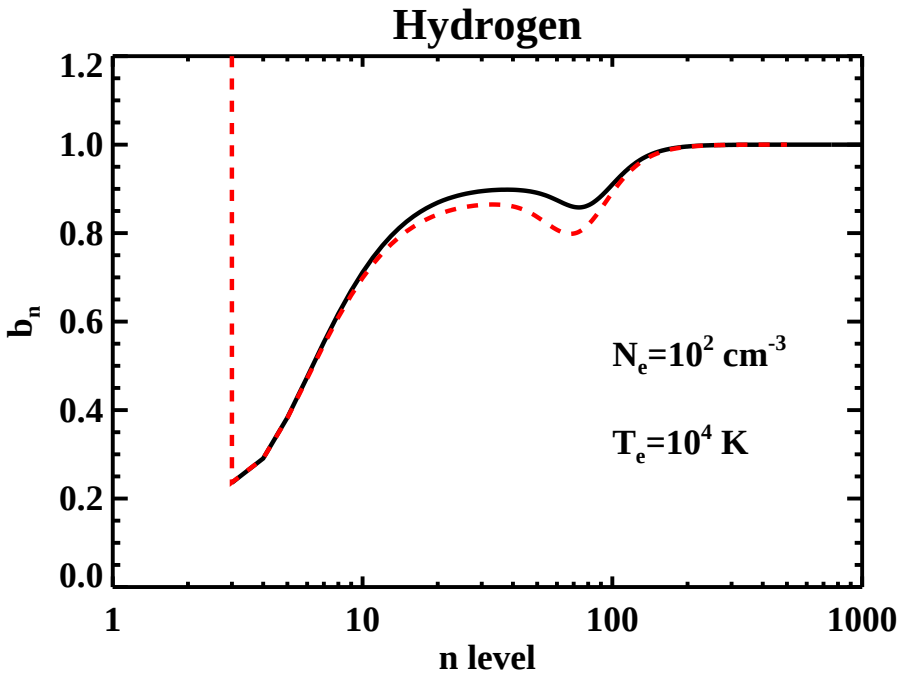

Figure 4.12: Comparison between our b_n values (black) at $T_e = 10^4$ K and $N_e = 100$ cm^{-3} and the results from Hummer and Storey (1992) (red line, dashed). Differences are due to the use of l-changing collision rates from Vrinceanu et al. (2012).

100 K, $N_e = 0.1$ cm^{-3} case. Using $b_n = 1.2$ and Equation 4.6, we estimate the ratio $b_{n+1}/b_n = 0.9996$ for the results in Ponomarev and Sorochenko (1992). Our result is ~ 0.99997 for the same physical conditions. The β_n values are quite sensitive to small variations in b_n^{final}. Since our b_n^{final} values are quite different from those in Ponomarev and Sorochenko (1992), large differences in the β_n values are not surprising.

4.4 Summary and Conclusions

We have solved the level population equation for hydrogenic atoms using accurate rates involved in the process. The level population equation is solved in two approximations: the n and the nl method. The departure coefficients obtained using the n method are similar to values from the literature (e.g. Brocklehurst 1970 and Shaver 1975). Our results using the nl method reproduce those from Hummer and Storey (1987) well, once allowance is made for updates in the

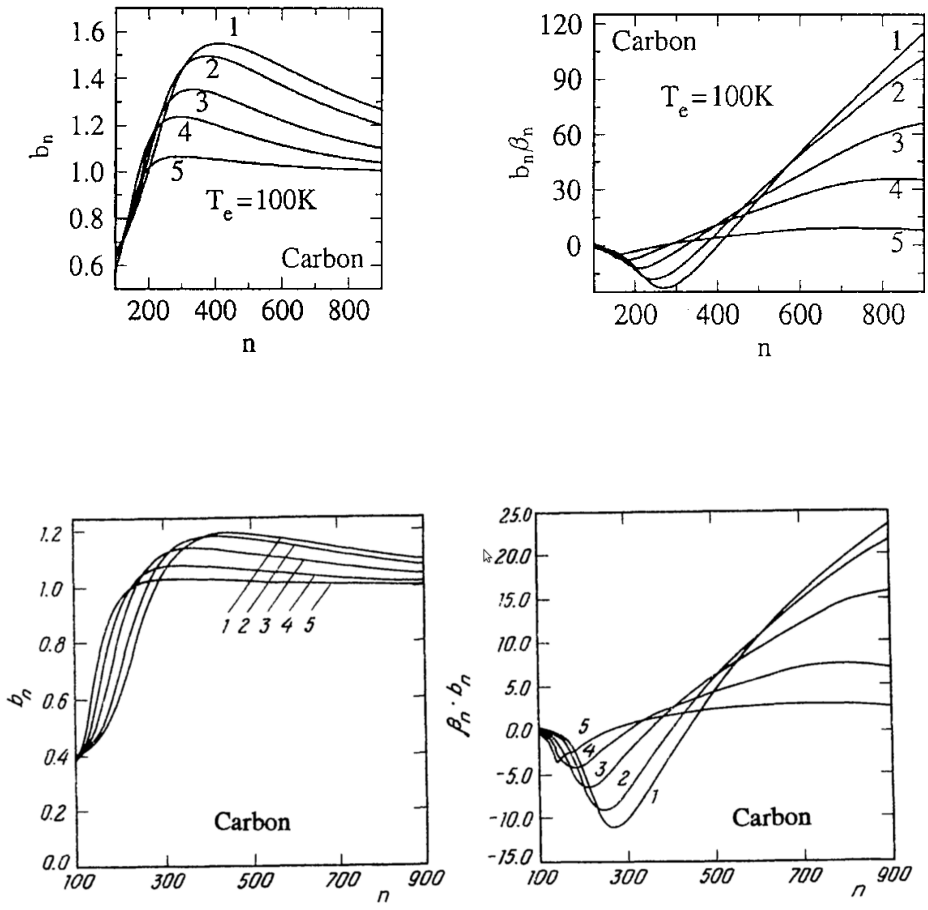

Figure 4.13: Departure coefficients from Ponomarev and Sorochenko (1992) at T_e = 100 K and 50 K. Lines correspond to electron densities n_e = 0.05, 0.1, 0.3, 1.0 and 3.0 cm^{-3} marked from 1 to 5 (from lower to higher densities). Upper panels: b_n values (Left) and $b_n\beta_n$ values for T_e = 100 K (Gordon and Sorochenko, 2009). Lower panels: b_n values (Left) and $b_n\beta_n$ values for T_e = 50 K (Ponomarev and Sorochenko, 1992).

collisional rates.

By including the dielectronic recombination process together with the *nl* method we are able to model the level population of carbon in terms of the departure coefficients. Our results are qualitatively similar to those of Watson

et al. (1980); Walmsley and Watson (1982a). However, the values obtained here differ considerably from those from the literature. The differences can be understood in terms of the use of improved collision rates and the improved numerical approach using the nl method. We confirm that dielectronic recombination can indeed produce an increase on the values of the departure coefficients at high n levels compared to the hydrogenic values.

In anticipation of low frequency radio recombination line surveys of the diffuse interstellar medium now being undertaken by LOFAR, we have expanded the range of applicability of the formulation to the conditions of the cold neutral medium. For this environment, external radiation fields also become important at intermediate principal quantum levels while at high levels the influence of radiation fields on the level population is less important. In Section 5, we discuss the expected line strength for low frequency carbon radio recombination lines. We compare our results to existing observations of CRRLs towards Cas A and regions in the inner galaxy. We also describe the analysis techniques and diagnostic diagrams that can be used to analyze the forthcoming LOFAR CRRL survey. The departure coefficients obtained here will be used to analyze the LOFAR observations of Cas A in a future article (Oonk et al., 2015a).

A List of Symbols

Table 4.1: List of Symbols

Symbol	Descritpion
$A_{3/2,1/2}$	Spontaneous transition rate of the carbon fine structure line $^2P_{3/2}$-$^2P_{1/2}$
A^a_{nl}	Autoionization rate
$A_{n'n}$	Einstein coefficient for spontaneous transition between n' and n
$A_{n'l'nl}$	Einstein coefficient for spontaneous transition between $n'l'$ state to nl state
a_0	Bohr radius
a_{nl}	Photoionization cross section
$B_{nn'}$	Einstein coefficient for stimulated transition from level n' to n
b_n	Departure coefficient for level n
$b_n^{1/2}$	Departure coefficient for atoms recombining from the 1/2 ion core for level n
$b_n^{3/2}$	Departure coefficient for atoms recombining from the 3/2 ion core for level n
b_n^{final}	Departure coefficient for atoms recombining from both ion cores
C$n\alpha$	Carbon recombination line for α transition
$C_{n'n}$	Rates for energy changing collisions between level n' and n
$C(n,l)$	Coefficient for recursion relations used to obtain the radial matrices values
c	Speed of light
$EM_{\mathrm{C+}}$	Emission measure of carbon ions
$g_{3/2}$	Statistical weight for the fine structure level $^2P_{3/2}$
$g_{1/2}$	Statistical weight for the fine structure level $^2P_{1/2}$
h	Planck constant
$I_0(\nu)$	Intensity of the background continuum
I_ν^{line}	Intensity of the line
I_ν^{cont}	Intensity of the continuum
I_{158}	Intensity of the fine structure line of carbon at 158 μm
j_ν	line emission coefficient
k_ν	line absorption coefficient
k	Boltzmann constant

Continued on next page

Table 4.1 – *Continued from previous page*

Symbol	
L	Pathlength of cloud
l	Angular momentum quantum number
N_{cr}	Critical density for collisions on a two level atom
N_n	Density of atoms in level n
N_{nl}	Density of atoms in level n and sublevel l
N_e	Electron density
N_H	Hydrogen density
N_{ion}	Density of the parent ions
$N^+_{3/2}$	Level population of carbon ions in the $^2P_{3/2}$ core
$N^+_{1/2}$	Level population of carbon ions in the $^2P_{1/2}$ core
n	Lower principal quantum number
n'	Upper principal quantum number
n_{max}	Maximum level considered in our simulations
n_{crit}	Critical level considered in our simulations for the nl-method
n_t	Level where observed lines transition from emission to absorption
$\mathscr{R}(n,l)$	Normalized radial wave function for level n, l
R	Ratio between the fine structure ($^2P_{3/2}$-$^2P_{1/2}$) level population and the fine structure level population in LTE
$R(l',l)$	Integral of the radial matrix elements
Ry	Rydberg constant
T_0	Temperature of power law background spectrum at frequency ν_0
T_e	Electron temperature
Z	
α_n	Radiative recombination coefficient to a level n
α_{nl}	Radiative recombination coefficient to a level n and sublevel l
α^d_{nl}	Dielectronic recombination rate
$\beta_{nn'}$	Correction factor for stimulated emission
γ_e	De-excitation rate for carbon ions in the $^2P_{3/2}$ core due to collisions with electrons
γ_H	De-excitation rate for carbon ions in the $^2P_{3/2}$ core due to collisions with hydrogen atoms
ΔE	Energy difference between two levels
Δn	$n'-n$, difference between the upper an lower principal quantum number
η	Correction factor to the Planck function due to non-LTE level population

Continued on next page

Table 4.1 – *Continued from previous page*

Symbol	
μ	Reduced mass
ν	Frequency of a transition
ν_0	Reference frequency for the power law background spectrum
$\phi(\nu)$	Line profile
ω_{nl}	Statistical weight of level nl
ω_i	Statistical weight of parent ion
χ_n	Ionization potential of a level n, divided by kT_e

B Level population

The strength (or depth) of an emission (absorption) line depends on the level population of atoms. The line emission and absorption coefficients are given by (e.g. Shaver 1975; Gordon and Sorochenko 2009):

$$j_\nu = \frac{h\nu}{4\pi} A_{n'n} N_{n'} \phi(\nu), \tag{B1}$$

$$k_\nu = \frac{h\nu}{4\pi} \left(N_n B_{nn'} - N_{n'} B_{n'n}\right) \phi(\nu), \tag{B2}$$

where h is the Planck constant, $N_{n'}$ is the level population of a given upper level (n') and N_n is the level population of the lower level (n); $\phi(\nu)$ is the line profile, ν is the frequency of the transition and $A_{n'n}$, $B_{n'n}(B_{nn'})$ are the Einstein coefficients for spontaneous and stimulated emission (absorption), respectively. Following Hummer and Storey (1987), we present the results of our modeling in terms of the departure coefficients (b_n) and the correction factor for stimulated emission/absorption (β_n):

$$b_n = \frac{N_n}{N_n(LTE)}. \tag{B3}$$

$$\beta_{n,n'} = \frac{1 - (b_{n'}/b_n)\exp(-h\nu/kT_e)}{1 - \exp(-h\nu/kT_e)}, \tag{B4}$$

unless otherwise stated the β_n presented here correspond to $\beta_{n+1,n}$, i.e. α transitions. When a cloud is located in front of a strong background source the integrated line to continuum ratio is proportional to $b_n\beta_n$ (Shaver, 1975; Payne et al., 1994). We expand on the radiative transfer problem in Paper II.

B.1 Hydrogenic atoms

Under thermodynamic equilibrium conditions, level populations are given by the Saha-Boltzmann equation (e.g. Brocklehurst and Seaton 1972; Gordon and Sorochenko 2009):

$$N_{nl}(LTE) = N_e N_{ion} \left(\frac{h^2}{2\pi m_e k T_e} \right)^{3/2} \frac{\omega_{nl}}{2\omega_i} e^{\chi_n}, \chi_n = \frac{hcZ^2 Ry}{n^2 k T_e}, \quad \text{(B5)}$$

where N_e is the electron density in the nebula, N_{ion} is the ion density, m_e is the electron mass, k is the Boltzmann constant, Ry is the Rydberg constant ω_{nl} is the statistical weight of the level n and angular quantum momentum level l [$\omega_{nl} = 2(2l+1)$, for hydrogen], ω_i is the statistical weight of the parent ion. The factor $\left(h^2/2\pi m_e k T_e\right)^{0.5}$ is the thermal de Broglie wavelength, Λ, of the free electron $\left[\Lambda(T_e)^3 \approx 4.14133 \times 10^{-16}\ T_e^{-1.5}\ \mathrm{cm}^3\right]$. In general, lines are formed under non-LTE conditions and, in order to properly model the line behavior, the level population equation must be solved. We follow the methods described in Brocklehurst (1971) and improved upon by Hummer and Storey (1987) as described in Section 4.2. Here, we give a detailed derivation of the theory and methods. First, we solve the level population equation assuming statistical population of the angular momentum l-levels, i.e.:

$$N_n = \sum_{l=0}^{n-1} \frac{(2l+1)}{n^2} N_{nl}, \quad \text{(B6)}$$

for all n levels. This assumption greatly simplifies the calculations but is only valid when l changing transitions are faster than other processes, and, in general, this is not the case for low n levels. The level population equation under this assumption is (e.g. Shaver 1975; Gordon and Sorochenko 2009):

$$N_n \left[\sum_{n'<n} A_{nn'} + \sum_{n' \neq n} (B_{nn'} I_\nu + C_{nn'}) + C_{ni} \right] =$$
$$\sum_{n'>n} N_{n'} A_{n'n} + \sum_{n' \neq n} N_{n'} (B_{n'n} I_\nu + C_{n'n}) + N_e N_{ion} (\alpha_n + C_{in}). \quad \text{(B7)}$$

The right- and left-hand side of Equation B7 describe how level n is populated and depopulated, respectively. We take into account spontaneous transitions from level n to lower levels ($A_{nn'}$), stimulated emission and absorption ($B_{nn'} I_\nu$, $B_{n'n} I_\nu$), collisional transitions ($C_{nn'}$), radiative recombination (α_n), collisional ionization (C_{in}) and 3-body recombination (C_{ni}). Equation B7 can be written

in terms of the departure coefficients (b_n):

$$b_n \left[\sum_{n'<n} A_{nn'} + \sum_{n' \neq n} (B_{nn'} I_\nu + C_{nn'}) + C_{ni} \right] = \sum_{n'>n} b_{n'} \frac{\omega_{n'}}{\omega_n} e^{\Delta\chi_{n'n}} A_{n'n} + \sum_{n' \neq n} b_{n'} \frac{\omega_{n'}}{\omega_n} e^{\Delta\chi_{n'n}} (B_{n'n} I_\nu + C_{n'n}) + \frac{N_e N_{ion}}{N_n(LTE)} (\alpha_n + C_{in}). \quad \text{(B8)}$$

The previous equation can be written as a matrix equation of the form $\mathbf{R}\times\mathbf{b}=\mathbf{S}$ by choosing the appropriate elements to form the matrices $\mathbf{R}$ and $\mathbf{S}$ (e.g. Shaver 1975):

$$R_{n'n} = -\frac{\omega_{n'}}{\omega_n} e^{\Delta\chi_{n'n}} (A_{n'n} + B_{n'n} I_\nu + C_{n'n}), (n' > n) \quad \text{(B9)}$$

$$R_{nn} = \sum_{n'<n} A_{nn'} + \sum_{n' \neq n} (B_{nn'} I_\nu + C_{nn'}) + C_{ni} \quad \text{(B10)}$$

$$R_{n'n} = -\frac{\omega_{n'}}{\omega_n} e^{\Delta\chi_{n'n}} (B_{n'n} I_\nu + C_{n'n}), (n' < n) \quad \text{(B11)}$$

$$S_n = \frac{N_e N_{ion}}{N_n(LTE)} (\alpha_n + C_{in}). \quad \text{(B12)}$$

It is easy to solve for the b_n values by using standard matrix inversion techniques. We will refer to this approach of solving the level population equation as the n-method.

At low n levels, the quantum angular momentum distribution must be obtained, since the assumption that the angular momentum levels are in statistical equilibrium is no longer valid. Moreover, as described in Watson et al. (1980); Walmsley and Watson (1982a), dielectronic recombination is an important process for carbon ions at low temperatures and densities. Since the dielectronic recombination process depends on the quantum angular momentum distribution, we need to include the l sublevel distribution for a given n level.

The level population equation considering l-levels is:

$$b_{nl} \left[\sum_{n'<n} \sum_{l'=l\pm1} A_{nln'l'} + \sum_{n' \neq n} (B_{nln'l'} I_\nu + C_{nln'l'}) + \sum_{l'=l\pm1} C_{nlnl'} + C_{nl,i} \right] = \sum_{n'>n} \sum_{l'=l\pm1} b_{n'l'} \frac{\omega_{n'l'}}{\omega_{nl}} e^{\Delta\chi_{n'n}} A_{n'l'nl} + \sum_{n' \neq n} \sum_{l'=l\pm1} b_{n'l'} \frac{\omega_{n'l'}}{\omega_{nl}} e^{\Delta\chi_{n'n}} (B_{n'l'nl} I_\nu + C_{n'l'nl}) + \sum_{l'=l\pm1} b_{nl'} \left(\frac{\omega_{nl'}}{\omega_{nl}} \right) C_{nl'nl} + \frac{N_e N_{ion}}{N_{nl}(LTE)} (\alpha_{nl} + C_{i,nl}). \quad \text{(B13)}$$

To solve for the l level distribution at a given n level we followed an iterative approach as described in Brocklehurst (1971); Hummer and Storey (1987). We will refer to this approach of solving the level population equation as the nl-method.

We start the computations by applying the n-method, i.e. assuming $b_{nl} = b_n$ for all l levels, thus obtaining $b_{nl}^{(0)}$ values. For levels above a given n_{crit} value we expect the l-sublevels to be in statistical equilibrium. In this case, Equation B6 is valid and the b_{nl} values are equal to those obtained by the n-method. On the first iteration, we start solving Equation B13 at $n = n_{crit}$ and use the previously computed values ($b_{n'l'}^{(0)}$) for levels $n' \neq n$. Equation B13 is then a tri-diagonal matrix (only elements with $l' = l \pm 1$, enter in the equation) and, by solving the system of equations, we obtain $b_{nl}^{(1)}$ values. The operation is repeated for all n levels down to $n = n_{min}$. In all our simulations we assume $n_{min} = 3$ since we are focused on studying carbon atoms whose ground level correspond to $n = 2$. We repeat the operation by using the $b_{nl}^{(1)}$ values instead of the $b_{nl}^{(0)}$ values. Hummer and Storey (1987) have proven that considering collisions from (and to) all n' levels guarantees a continuous distribution between both approaches at levels close to n_{crit}. The final b_n values are computed by taking the weighted sum of the b_{nl} values:

$$b_n = \sum_{l=0}^{n-1} \left(\frac{2l+1}{n^2} \right) b_{nl}, \tag{B14}$$

Details on the parameters used in this work are given in the text (Section 4.2.2).

C Radial Matrices and Einstein A coefficients

In general, the radiative decay depends on the angular momentum quantum number of the electron at the level n. Transitions from level $nl \rightarrow n'l'$ are described by $A_{nln'l'}$ coefficients, in the dipole approximation (Seaton, 1959a):

$$A_{nln'l'} = \frac{64\pi^4\nu^3}{3hc^3} e^2 a_0^2 \frac{\max(l,l')}{2l+1} \left| \int_0^\infty \mathscr{R}(n',l') r \mathscr{R}(n,l) \mathrm{d}r \right|^2, \tag{C1}$$

where a_0 is the Bohr radius and $\mathscr{R}(n,l)$ is the normalized radial wave function solution to the Schrödinger equation of the Hydrogen atom (Burgess, 1958; Brocklehurst, 1971). The computation of the matrix elements is challenging (see Morabito et al. 2014c for details) and we follow the recursion relations given by Storey and Hummer (1991) to calculate them up to $n = 10000$. Defining:

$$R(l',l) = \int_0^\infty \mathscr{R}(n',l') r \mathscr{R}(n,l) \mathrm{d}r, \tag{C2}$$

where the first argument of $R(l', l)$ corresponds to the lower state. For a given n' level, Storey and Hummer (1991) give the following relations, with the starting values:

$$\begin{aligned} R(n', n'-1) &= 0, \\ R(n'-1, n') &= \frac{1}{4}\left(4nn'\right)^{n'+2}\left[\frac{(n+n')!}{(n-n'-1)!(2n'-1)!}\right]^{1/2}\frac{(n-n')^{n-n'-2}}{(n+n')^{n+n'+2}}. \end{aligned}$$

The recursion relations are:

$$2lC(n', l)R(l-1, l) = (2l+1)C(n, l+1)R(l, l+1) + C(n', l+1)R(l+1, l), \quad \text{(C3)}$$

and:

$$2lC(n, l)R(l, l-1) = C(n, l+1)R(l, l+1) + (2l+1)C(n', l+1)R(l+1, l), \quad \text{(C4)}$$

with:

$$C(n, l) = \frac{\sqrt{(n+l)(n-l)}}{nl} \quad \text{(C5)}$$

D Radiative recombination cross-section

Storey and Hummer (1991) give a formula for computing the photoionization cross-section:

$$a_{nl}(h\nu) = \left(\frac{4\pi a_0^2 \alpha}{3}\right)\frac{\left(1+n^2\kappa^2\right)}{\mu^2 Z^2 n^2}\frac{\max(l, l')}{2l+1}\left|\int_0^\infty \mathscr{R}(n', l')r\mathscr{R}(\kappa, l)\mathrm{d}r\right|^2. \quad \text{(D1)}$$

To obtain the radial matrices elements, we use the same recursion formula as for the Einstein A coefficients with the substitution: $n = i/\kappa$, with i the imaginary number. The $C(n, l)$ coefficients are:

$$C(n, l) = \frac{\sqrt{(1+l^2\kappa^2)}}{l}, \quad \text{(D2)}$$

and the initial values are:

$$\begin{aligned} R(n', n'-1) &= 0, \\ R(n'-1, n')_{\kappa=0} &= \frac{1}{4}\left[\frac{\pi}{2\,(2n'-1)!}\right]^{1/2}(4n')^{n'+2}e^{-2n'}, \\ R(n'-1, n')_{\kappa\neq 0} &= \left[\frac{\prod_{s=1}^{n'}(1+s^2\kappa^2)}{1-\exp(-2\pi/\kappa)}\right]^{1/2}\frac{\exp[2n'-(2/\kappa)\arctan(n'\kappa)]}{\left(1+n'^2\kappa^2\right)^{n'+2}}R(n'-1, n')_{\kappa=0}. \end{aligned}$$

We are interested in computing the recombination cross-section for an electron with energy E recombining to a level nl. From Milne relation we obtain (e.g. Rybicki and Lightman 1986):

$$\sigma(E,nl) = \frac{16\pi a_0^2}{3\sqrt{2}}\sqrt{\frac{hcRy}{E}}\sqrt{\frac{m_e c^2}{E}}\left(\frac{E+h\nu_n}{m_e c^2}\right)^3 \sum_{l'} \max(l,l') \left| \int_0^\infty \mathscr{R}(\kappa,l') r \mathscr{R}(n,l) \mathrm{d}r \right|^2 \quad \text{(D3)}$$

expressed in terms of the radial matrices. Here, $h\nu_n$ is the ionization energy of the level n. The final rate is obtained by integrating the cross-section over a Maxwellian velocity distribution:

$$\alpha_{nl} = \frac{8}{\sqrt{\pi m_e}}(kT_e)^{-3/2} \int_0^\infty \sigma(E,nl) e^{-E/kT_e} \mathrm{d}E. \quad \text{(D4)}$$

We consider $x = E/kT_e$ and $I(x)$ is the function in the integral. To integrate the cross-section, we followed an approach similar to Burgess (1965). We divide the integral in 30 segments starting at $x_0 = kT \times 10^{-10}$, and ending at $x_f = 20 \times kT$. Each segment is integrated by using a 6-point Gauss-Legendre quadrature scheme. This approach provides the value of the integral close to kT, therefore two correction factors must be applied: for the small values of x we note that the integrand is almost constant and the value of the integral is then $I(x_0)x_0^2/2$; for large values of x we use a 6-point Gauss-Legendre quadrature starting at $x_0 = 20 \times kT$ and ending at $x_f = 30 \times kT$. As mentioned in Section 4.3 we compare the sum over l, of our radiative recombination rates with the formula of Seaton (1959b):

$$\alpha_n = 2.06 \times 10^{-11} \left(\frac{Z}{nT_e^{0.5}}\right) \chi_n S_n(\lambda) \ \mathrm{cm^3 s^{-1}}, \quad \text{(D5)}$$

with $\lambda = n^2\chi_n$, and

$$S_n(\lambda) = \int_0^\infty \frac{g_{II}(n,\epsilon) e^{-x_n u}}{1+u} du, u = n^2\epsilon. \quad \text{(D6)}$$

Values for the $\chi_n S_n(\lambda)$ are given by Seaton (1959b) in two approximations for large and small argument, and tabulated values are also given for values in between the approximations. A first order expansion of the Gaunt factor (Allen, 1973) provides an accurate formula for the recombination coefficient:

$$\alpha_n = 3.262 \times 10^{-6} \left(\frac{Z^4}{n^3 T_e^{1.5}}\right) e^{\chi_n} E_1(\chi_n) \ \mathrm{cm^3 s^{-1}}. \quad \text{(D7)}$$

E Energy changing collision rates

Vriens and Smeets (1980) obtained the following semi-empirical formula for excitation by electrons. The formula is given by:

$$C_{nn'} = 1.6 \times 10^{-7} \frac{\sqrt{kT_e}}{kT_e + \Gamma_{nn'}} \exp(-\epsilon_{nn'}) \left[A_{nn'} \ln(0.3 \frac{kT_e}{hcRy} + \Delta_{nn'}) + B_{nn'} \right], \quad \text{(E1)}$$

with the coefficients defined as:

$$\begin{aligned}
s &= |n - n'|, \\
A_{nn'} &= 2 \frac{hcRy}{E_{nn'}} f_{nn'}, \\
B_{nn'} &= 4 \frac{(hcRy)^2}{n^3} \left(\frac{1}{E_{nn'}^2} + \frac{4}{3} \frac{E_{ni}}{E_{nn'}^3} + b_p \frac{E_{ni}^2}{E_{nn'^4}} \right), \\
b_p &= 1.4 \frac{\ln(n)}{n} - \frac{0.7}{n} - \frac{0.51}{n^2} + \frac{1.16}{n^3} - \frac{0.55}{n^4}, \\
\Delta_{nn'} &= \exp(-\frac{B_{nn'}}{A_{n,n'}}) + 0.06 \frac{s^2}{nn'^2},
\end{aligned}$$

$$\Gamma_{nn'} = hcRy \ln(1 + \frac{n'^3 kT_e}{hcRy}) \left[3 + 11 \left(\frac{s}{p} \right)^2 \right] \left(6 + 1.6ns + \frac{0.3}{s^2} + 0.8 \sqrt{\frac{n^3}{s}} \, |s - 0.6| \right)^{-1}.$$

F Collisional ionization

We use the formulation in the code of Brocklehurst and Seaton (1972) to obtain the values for the collisional ionization rates, the formulation is based on Burgess and Percival (1968):

$$C_{i,n} = \frac{5.444089}{T_e^{3/2}} e^{-\chi_n} \left[\left(\frac{5}{3} - \frac{\chi_n}{3} \right) \frac{1}{\chi_n} + \frac{1}{3} (\chi_n - 1) E_1(\chi_n) e^{\chi_n} - \frac{1}{2} E_1(\chi_n)^2 e^{2\chi_n} \right], \quad \text{(F1)}$$

in units of cm^3 s^{-1}.

Chapter 5

Low Frequency Carbon Radio Recombination Lines II: The Diffuse Interstellar Medium

Based on: Salgado, F. et al., 2015

Abstract

In the second paper of the series, we have modeled low frequency carbon radio recombination lines (CRRL) from the interstellar medium. Anticipating the LOw Frequency ARray (LOFAR) survey of Galactic CRRLs, we focus our study on the physical conditions of the diffuse cold neutral medium (CNM). We have used the improved departure coefficients computed in the first paper of the series to calculate line-to-continuum ratios. The results show that the line width and integrated optical depths of CRRL are sensitive probes of the electron density, gas temperature, and the emission measure of the cloud. Furthermore, the ratio of CRRL to the [CII] at 158 μm line is a strong function of the temperature and density of diffuse clouds. Guided by our calculations, we analyze CRRL observations and illustrate their use with data from the literature.

5.1 Introduction

The interstellar medium (ISM) plays a central role in the evolution of galaxies. The formation of new stars slowly consumes the ISM, locking it up for millions to billions of years while stars, as they age, return much of their mass increased in metallicity, back to the ISM. Stars also inject radiative and kinetic energy into the ISM and this controls the physical characteristics (density, temperature and pressure) as well as the dynamics of the gas as revealed in observed spectra. This interplay of stars and surrounding gas leads to the presence of distinct phases (e.g. Field et al. 1969; McKee and Ostriker 1977). Diffuse atomic clouds (the Cold Neutral Medium, CNM) have densities of about 50 cm^{-3} and temperatures of about 80 K, where atomic hydrogen is largely neutral but carbon is singly ionized by photons with energies between 11.2 eV and 13.6 eV. The warmer ($\sim$ 8000 K) and more tenuous ($\sim$ 0.5 cm^{-3}) intercloud phase [the Warm Neutral medium (WNM) and Warm Ionized Medium (WIM)] is heated and ionized by FUV and EUV photons escaping from HII regions (Wolfire et al., 2003). While these phases are often considered to be in thermal equilibrium and in pressure balance, the observed large turbulent width and presence of gas at thermally unstable, intermediate temperatures attests to the importance of heating by kinetic energy input. In addition, the ISM also hosts molecular clouds, where hydrogen is in the form of H_2 and self-gravity plays an important role. All of these phases are directly tied to key questions on the origin and evolution of the ISM, including energetics of the CNM, WNM and the WIM; the evolutionary relationship of atomic and molecular gas; the relationship of these ISM phases with newly formed stars; and the conversion of their radiative and kinetic power into thermal and turbulent energy of the ISM (e.g. Cox 2005; Elmegreen and Scalo 2004; Scalo and Elmegreen 2004; McKee and Ostriker 2007).

The diffuse interstellar medium has been long studied using, in particular, the 21 cm hyperfine transition of neutral atomic hydrogen. On a global scale, these observations have revealed the prevalence of a two phase structure in the interstellar medium of cold clouds embedded in a warm intercloud medium but they have also pointed out challenges to this theoretical view (Kulkarni and Heiles, 1987; Kalberla and Kerp, 2009). However, it has been notoriously difficult to determine the physical characteristics (density, temperature) of these structures in the ISM as HI by itself does not provide a good probe. Optical and UV observations of atomic lines can provide the physical conditions but are by necessity limited to pinpoint experiments towards bright background sources. However, with the opening up of the low frequency radio sky with modern interferometers such as the Low Frequency ARray for Radioastronomy (LOFAR, van Haarlem et al. 2013), Murchison Wide field Array (Tingay et al., 2013), Long Wavelength Array (Ellingson et al., 2013) and, in the future, the Square

Kilometer Array (SKA), systematic surveys of low frequency ($\nu \lesssim 300$ MHz) Carbon Radio Recombination Lines (CRRLs) have come in reach and these surveys can be expected to quantitatively measure the conditions in the emitting gas (Oonk et al., 2015b).

Carbon has a lower ionization potential (11.2 eV) than hydrogen and can be ionized by radiation fields in regions where hydrogen is largely neutral. Recombination of carbon ions with electrons to high Rydberg states will lead to CRRLs in the sub-millimeter to decameter range. CRRLs have been observed in the interstellar medium of our Galaxy towards two types of clouds: diffuse clouds (e.g.: Konovalenko and Sodin 1981; Erickson et al. 1995; Roshi et al. 2002; Stepkin et al. 2007; Oonk et al. 2014) and photodissociation regions (PDRs), the boundaries of HII regions and their parent molecular clouds (e.g.: Natta et al. 1994; Wyrowski et al. 1997; Quireza et al. 2006). Recently, Morabito et al. (2014b) discovered extragalactic CRRLs associated with the nucleus of the nearby starburst galaxy, M82. Theoretical models for CRRLs were first developed by Watson et al. (1980) and Walmsley and Watson (1982a), including the effects of dielectronic recombination with the simultaneous excitation of the $^2P_{3/2}$ fine-structure level and later extended by Ponomarev and Sorochenko (1992) and by Payne et al. (1994). However, these studies were hampered by the limited computer resources available at that time.

In the coming years, we will use LOFAR to carry out a full northern hemisphere survey of CRRL emitting clouds in the Milky Way. This will allow us to study the thermal balance, chemical enrichment and ionization rate of the cold neutral medium from degree-scales down to scales corresponding to individual clouds and filaments in our Galaxy. Furthermore, following the first detection of low-frequency CRRLs in an extragalactic source (M82; Morabito et al. 2014b) we will also use LOFAR to perform the first flux limited survey of CRRLs in extragalactic sources. Given the renewed observational interest in CRRLs, a new theoretical effort seems warranted. In Section 4, we studied the level population of hydrogenic atoms including the effects of dielectronic recombination in carbon atoms. The level population of atoms, however, is not the only process that influences the strength of an observed line as radiative transfer effects can alter the strength/depth of an observed line. In this paper, we use the results of Paper I to develop CRRLs as a tool to derive the physical conditions in the emitting gas. In this, we will focus on cold diffuse clouds as these are expected to dominate the low frequency CRRL sky. The paper is organized as follows: in Section 5.2.1 we review radiative transfer theory in the context of radio recombination lines. We review the line broadening mechanisms of CRRLs in Section 5.2.3. In Section 5.3, we present the results of our models and compare them with observations from the literature and provide guidelines to analyze such observations. Finally, in Section 5.6, we summarize our results and provide the conclusions of our work.

5.2 Theory

5.2.1 Radiative transfer of carbon radio recombination lines

The physical conditions of the diffuse interstellar medium (temperatures of $T_e \approx 100$ K and electron densities $n_e \approx 10^{-2}$) favor an increase in the level population at high quantum levels via dielectronic recombination (Paper I). Moreover, the presence of an external radiation field can also alter the level population of carbon atoms. In addition, while low frequency CRRLs are observed in absorption against a background continuum (e.g. Kantharia and Anantharamaiah 2001; Oonk et al. 2014; Morabito et al. 2014b), high frequency recombination lines are observed in emission. Therefore, radiative transfer effects must be analyzed in order to derive meaningful physical parameters from observations.

We begin our analysis by revisiting the radiative transfer problem in the context of CRRLs. At a given frequency, the observed emission has two components, corresponding to the line transition itself and the underlying continuum emission. In Appendix B, we summarize the standard general solution to the one dimensional radiative transfer equation of a line in a homogeneous medium. Here, we show the result for a cloud at a constant temperature T_e:

$$\frac{I_\nu^{line}}{I_\nu^{cont}} = \frac{\eta B_\nu(T_e)(1-e^{-\tau_\nu^{total}}) + I_0(\nu)e^{-\tau_\nu^{total}}}{B_\nu(T_e)(1-e^{-\tau_\nu^{c}}) + I_0(\nu)e^{-\tau_\nu^{c}}} - 1, \tag{5.1}$$

where I_ν^{line} is the intensity of a line at a frequency ν, I_ν^{cont} is the intensity of the continuum, η is a correction factor to the Planck function due to non-LTE effects (as defined in Strelnitski et al. 1996; Gordon and Sorochenko 2009, see Appendix B), $B_\nu(T_e)$ is the Planck function, τ_ν^{total} is the sum of the line and continuum optical depth (τ_l and τ_c, respectively) and $I_0(\nu)$ is the intensity of a background continuum source at the frequency of the line.

In the presence of a strong background radiation field, as is the case for low frequency lines in the diffuse ISM ($I_0 \gg \eta B_\nu(T_e)$, see below), the background term (I_0) dominates and the first term in the numerator and denominator on the right-hand-side of Equation 5.1 can be ignored and this equation simplifies to,

$$\frac{I_\nu^{line}}{I_\nu^{cont}} = e^{-\tau_\nu^{l}} - 1, \tag{5.2}$$

independent of the background source. Assuming that the line is optically thin ($|\tau_\nu^l| \ll 1$), Equation 5.2 is approximated by (e.g. Kantharia and Anantharamaiah 2001):

$$\frac{I_\nu^{line}}{I_\nu^{cont}} = -\tau_\nu^{l}. \tag{5.3}$$

Note that, due to the minus sign on the right hand side of Equation 5.3, when τ_l is positive the line is observed in absorption against the background source.

From the definition of τ_ν^l (see Appendix B) and explicitly considering the normalized line profile, $\phi(\nu)$, (with $\int \phi(\nu) = 1$):

$$\frac{I_\nu^{line}}{I_\nu^{cont}} = -\kappa_\nu^l \phi(\nu) L. \tag{5.4}$$

Introducing the departure coefficients from LTE, b_n and the correction factor for stimulated emission or absorption, β_n (Brocklehurst and Seaton, 1972; Gordon and Sorochenko, 2009), we can write,

$$\begin{aligned} \frac{I_\nu^{line}}{I_\nu^{cont}} &= -\kappa_\nu^l(LTE)\phi(\nu) b_n \beta_{nn'} L, \\ \frac{I_\nu^{line}}{I_\nu^{cont}} &\approx -1.069 \times 10^7 \Delta n M(\Delta n) \frac{b_n \beta_{nn'}}{T_e^{5/2}} e^{\chi_n} EM_{\rm C+} \phi(\nu), \end{aligned} \tag{5.5}$$

assuming $h\nu \ll kT_e$, and $\Delta n/n \ll 1$, in Equation 5 we have inserted the value for κ_ν^l absorption coefficient (Appendix B). Here, $EM_{\rm C+} = N_e N_{\rm C+} L$ is the emission measure in units of cm^{-6} pc, N_e is the electron density, N_{C+} is the carbon ion density and L is the pathlength of the cloud in pc. $\Delta n = n' - n$ is the difference between the levels involved in the transition, the factor $M(\Delta n)$[1] comes from the approximation to the oscillator strength of the transition, as given by Menzel (1968) (see Appendix C). The $b_n \beta_{nn'}$ factor relates the line emission or absorption to the level population of the emitting atoms and has been calculated following the method described in Paper I.

At the line center, the line to continuum ratio depends on the broadening of the line (see Section 5.2.3, below). However, we can remove the dependence on the line profile by integrating the line over frequency:

$$\int \frac{I_\nu^{line}}{I_\nu^{cont}} {\rm d}\nu = -1.069 \times 10^7 \Delta n M(\Delta n) \frac{b_n \beta_{nn'}}{T_e^{5/2}} e^{\chi_n} EM_{\rm C+} \text{ Hz}. \tag{5.6}$$

Note that by setting $\Delta n = 1$ (i.e. for C$n\alpha$ lines[2]) in Equation 5.6 we recover Equation 70 in Shaver (1975) and Equation 5 in Payne et al. (1994).

For high densities, $b_n \beta_n$ approaches unity at high n levels and the integrated line to continuum ratio changes little with n for a given T_e and $EM_{\rm C+}$. When the β_n factor in Equation 5.6 is positive (negative) the line is in absorption (emission). The strong dependence on electron temperature of the

[1]Some values for $M(\Delta n) = 0.1908,\ 0.02633,\ 0.008106,\ 0.003492,\ 0.001812$, for $\Delta n = 1,\ 2,\ 3,\ 4,\ 5$, respectively (Menzel, 1968).

[2]We will refer to electron transitions in carbon from levels $n+1 \rightarrow n$ as C$n\alpha$, $n+2 \rightarrow n$ as C$n\beta$ and $n+3 \rightarrow n$ as C$n\gamma$ (Gordon and Sorochenko, 2009).

integrated line to continuum ratio ($\propto T_e^{-2.5}$) favors the detection of low temperature clouds. An increase of a factor of two (three) in the temperature reduces the integrated line to continuum by a factor of about 6 (15), all other terms being equal.

From Equation 5.6, we note that for C$n\alpha$ lines:

$$\int \frac{I_\nu^{line}}{I_\nu^{cont}} \mathrm{d}\nu = -20.4 b_n \beta_{nn'} \left(\frac{T_e}{100\ \mathrm{K}}\right)^{-2.5} EM_{\mathrm{C+}}\ \mathrm{Hz}, \quad (5.7)$$

$$= -0.2 b_n \beta_{nn'} \left(\frac{T_e}{100\ \mathrm{K}}\right)^{-2.5} \left(\frac{N_e}{0.1\ \mathrm{cm}^{-3}}\right)^2 \left(\frac{L}{\mathrm{pc}}\right)\ \mathrm{Hz}, \quad (5.8)$$

assuming that electrons are produced by singly ionized carbon ($N_e = N_{C+}$) and for high n level ($n \gg \sqrt{(1.6 \times 10^5/T_e)}$). The typical optical depths that can be observed with current instruments are $\sim 10^{-3}$. As we already mentioned, for high n $b_n\beta_n \simeq 1$. Hence, clouds ($L \simeq 5$ pc) with electron densities greater than 10^{-2} cm^{-3} (hydrogen densities > 50 cm^{-3}) are readily observable.

5.2.2 The far-infrared fine structure line of C^+

The fine structure transition $^2P_{1/2} - {}^2P_{3/2}$ of carbon ions is one of the main coolants in diffuse neutral clouds at 158 μm. Moreover, the [CII] 158 μm is directly linked to the level population of carbon atoms at low temperatures through the dielectronic recombination process. In Section 5.3, we show how observations of this line combined with CRRLs can be used as powerful probes of the temperature of diffuse neutral clouds. Here, we give a description of an emission model of the line. The intensity of the [CII] 158 μm line in the optically thin limit is given by (e.g. Sorochenko and Tsivilev 2000):

$$I_{158} = \frac{h\nu}{4\pi} A_{3/2,1/2} N^+_{3/2} L$$

$$= \frac{h\nu}{4\pi} \frac{A_{3/2,1/2} 2\exp(-92/T_e) R}{1 + 2\exp(-92/T_e) R} N_{\mathrm{C^+}} L, \quad (5.9)$$

with ν the frequency of the $^2P_{1/2} - {}^2P_{3/2}$ transition, $A_{3/2,1/2} = 2.4 \times 10^{-6}$ s^{-1} is the spontaneous transition rate, $N^+_{3/2}$ the number density of carbon ions in the 3/2 state, L the length along the line of sight of the observed cloud and $N_{\mathrm{C^+}}$ the density of carbon ions; R is defined in Ponomarev and Sorochenko (1992); Payne et al. (1994) (see Paper I):

$$R = \frac{N_e\gamma_e + N_H\gamma_H}{N_e\gamma_e + N_H\gamma_H + A_{3/2,1/2}}, \quad (5.10)$$

where γ_e and γ_H are the de-excitation rates due to electrons and hydrogen atoms, respectively. The rates involved are detailed in Paper I. We assume that

collisions with electrons and hydrogen atoms dominate over molecular hydrogen and neglect collisions with H_2, as in Paper I. This is a good approximation for diffuse clouds with column densities up to $\sim 10^{21}$ cm^{-2}. For larger column densities, the H/H_2 transition will have to be modeled in order to evaluate R.

The optical depth of the C^+ fine structure line for the transition $^2P_{1/2}-^2P_{3/2}$ is given by Crawford et al. (1985); Sorochenko and Tsivilev (2000):

$$\tau_{158} = \frac{c^2}{8\pi\nu^2}\frac{A_{3/2,1/2}}{1.06\Delta\nu}2\alpha_{1/2}\beta_{158}N_{C^+}L, \tag{5.11}$$

$\Delta\nu$ is the FWHM of the line (assumed to be Gaussian); the $\alpha_{1/2}(T_e)$ and $\beta_{158}(T_e)$ coefficients depend on the electron temperature of the cloud and are defined by Sorochenko and Tsivilev (2000):

$$\alpha_{1/2}(T_e) = \frac{1}{1+2\exp(-92/T_e)R}, \tag{5.12}$$

$$\beta_{158}(T_e) = 1-\exp(-92/T_e)R. \tag{5.13}$$

Adopting a line width of 2 km s^{-1}, at low electron temperatures and densities, the FIR [CII] line is optically thin for hydrogen column densities less than about 1.2×10^{21} cm^{-2}. For a cloud size of 5 pc, this corresponds to hydrogen densities of $\sim 10^2$ cm^{-3} and electron densities of $\simeq 10^{-2}$ cm^{-3} if carbon is the dominant ion.

5.2.3 Line profile of recombination lines

The observed profile of a line depends on the physical conditions of the cloud, as an increase in electron density and temperature or the presence of a radiation field can broaden the line and this is particularly important for high n. Therefore, in order to determine the detectability of a line, the profile must be considered. Conversely, the observed line width of recombination lines provides additional information on the physical properties of the cloud.

The line profile is given by the convolution of a Gaussian and a Lorentzian profile, and is known as a Voigt profile (Shaver, 1975; Gordon and Sorochenko, 2009). Consider a cloud of gas of carbon ions at a temperature T_e. Random thermal motions of the atoms in the gas produce shifts in frequency that reflect on the line profile as a Gaussian broadening (Doppler broadening). In the most general case, turbulence can increase the width of a line and, as is common in the literature (e.g. Rybicki and Lightman 1986), we describe the turbulence by an RMS turbulent velocity. Thus, the Gaussian line profile can be described by:

$$\Delta\nu_D = \frac{\nu_0}{c}\sqrt{\frac{2kT_e}{m_C}+\langle v_{RMS}\rangle^2}, \tag{5.14}$$

where m_C is the mass of the carbon atom and $\langle v_{RMS} \rangle$ is the RMS turbulent velocity. The Gaussian width in frequency space is proportional to the frequency of the line transition.

At low frequencies, collisions and radiation broadening dominate the line width. The Lorentzian (FWHM) broadening produced by collisions is given by:

$$\Delta\nu_{col} = \frac{1}{\pi} \sum_{n \neq n'} N_e C_{n'n}, \tag{5.15}$$

where $C_{n'n}$ is the collision rate for electron induced transitions from level n' to n, and N_e is the electron density. Note that $C_{n'n}$ depends on temperature (Shaver, 1975; Gordon and Sorochenko, 2009). In order to estimate the collisional broadening, we fitted the following function at temperatures between 10 and 30000 K:

$$\sum_{n \neq n'} C_{n'n} = 10^{a(T_e)} n^{\gamma_c(T_e)}, \tag{5.16}$$

which is valid for levels $n > 100$. Values for $a(T_e)$ and $\gamma_c(T_e)$ as a function of electron temperature are given in Table 5.3.

In a similar way as for collisional broadening, the interaction of an emitter with a radiation field produces a broadening of the line profile. In Appendix C, we give a detailed expansion for different external radiation fields. Here, we discuss the case of a synchrotron radiation field characterized by a power-law with a temperature T_0 at a reference frequency $\nu_0 = 100$ MHz and an spectral index $\alpha_{pl} = -2.6$ (see section 5.3). Under the above considerations, the FWHM for radiation broadening is given by :

$$\Delta\nu_{rad} = 6.096 \times 10^{-17} T_0 n^{5.8} \ (\mathrm{s}^{-1}). \tag{5.17}$$

As is the case for collisional broadening, radiation broadening depends only on the level and the strength of the surrounding radiation field. The dependence on n is stronger than that of collisional broadening at low densities and radiation broadening dominates over collisional broadening. As the density decreases, the level n where radiation broadening dominates decreases. In order to estimate where this occurs we define t_n as:

$$\begin{aligned} t_n(T_e, T_0, N_e) &= \frac{\Delta\nu_{rad}}{\Delta\nu_{col}}, \\ &= \left[\frac{6.096 \times 10^{-17}}{10^{a(T_e)}}\right] \left(\frac{T_0}{N_e}\right) n^{5.8-\gamma_c(T_e)}. \end{aligned} \tag{5.18}$$

Note that the dependence on electron temperature is contained within the fitting coefficients, a and γ_c. For $T_e = 100$ K, we find $t_n \approx 5.82 \times 10^{-7} \sqrt{n}\,(T_0/N_e)$.

In Figure 5.1, we show t_n as a function of electron density for $T_0 = 1000$ K. For a given electron temperature and density, the influence of an external radiation field is larger for higher levels since $t_n \propto n^{5.8-\gamma_c}$ and $\gamma_c < 5.8$ (see Appendix). For a given density, the influence of the radiation field on the line width is larger at higher electron temperatures. For the typical conditions of the CNM, i. e. at $T_e = 100$ K and $N_e = 0.02$ cm^{-3}, the value of $t_n \approx 1$ and both radiation field and electron density affect the line width in similar amounts.

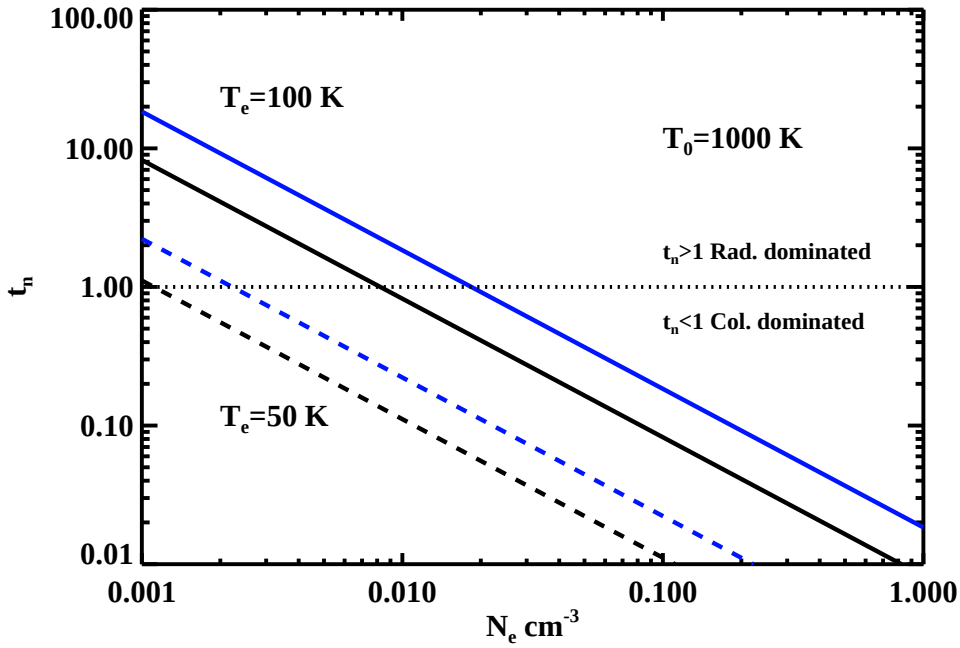

Figure 5.1: The t_n factor defined in Equation 5.18 as a function of electron density for quantum n levels between 200 (black line) and 1000 (blue line). The figure is presented for two electron temperatures: $T_e = 50$ K (dashed lines) and $T_e = 100$ K (solid lines). The dotted line marks the limit between the collision dominated regime ($t_n < 1$) and the radiative dominated regime ($t_n > 1$).

5.3 Method

In order to study the radiative transfer effects on the lines we use the method outlined in Paper I to compute the departure coefficients for different electron temperatures, densities and considering an external radiation field. The cosmic

microwave radiation field (CMB) and the Galactic synchrotron power law radiation field spectra are included. We represent the cosmic microwave radiation field (CMB) by a 3 K blackbody and the galactic radiation field by a power law $[I_0(\nu) = T_0(\nu/\nu_0)^{\alpha_{pl}}]$ with $T_0 = 1000$ K at a frequency $\nu_0 = 100$ MHz and $\alpha_{pl} = -2.6$ (Landecker and Wielebinski, 1970; Bennett et al., 2003). In the galactic plane, the Galactic radiation field can be much larger than 1000 K at 100 MHz (Haslam et al., 1982). At frequencies higher than 1 GHz, corresponding to C$n\alpha$ transitions from levels with $n < 200$, the background continuum is dominated by the CMB (Figure 5.2). At even higher frequencies, the background continuum can be dominated by dust and free-free emission, which are strongly dependent on the local conditions of the cloud and its position in the Galaxy. For simplicity, we focus our study on levels with $n > 200$.

Departure coefficients were computed for $T_e = 20,\ 50,\ 100$ and 200 K and electron densities in the range 10^{-2} to 1 cm^{-3}. Once the departure coefficients were obtained, we computed the corresponding optical depths assuming a fixed length along the line of sight of 1 pc from the usually adopted approximated optical depth solution to the radiative transfer problem (Equation 5.6). The value of 1 pc corresponds to emission measures in the range of $EM_{\rm C+} = 10^{-4}$ to 1 cm^{-6} pc. Our calculations assume a homogeneous density distribution in a cloud and should be taken as illustrative since it is well known that inhomogeneities exist in most clouds. The fixed length of 1 pc corresponds to column densities of 10^{18} to 10^{21} cm^{-2}, with the adopted density range. Diffuse clouds show a power-law distribution function in HI column density with a median column density of 0.8×10^{20} cm^{-2} (Kulkarni and Heiles, 1987). Reddening studies are weighted to somewhat large clouds and the standard "Spitzer" type cloud (Spitzer, 1978) corresponds to a column density of 3.6×10^{20} cm^{-2}. Local HI complexes associated with molecular clouds have $N_H \approx 10^{21}$ cm^{-2}.

5.4 Results

5.4.1 Line widths

We begin our discussion with the results for the line widths. We show the line widths for our diffuse clouds models in Figure 5.3. At high frequencies (low n), the Gaussian (Doppler) core of the line dominates the line profile in frequency space and the line width increases with frequency. At low frequencies (high n), on the other hand, the Lorentzian profile dominates –either because of collisional or radiation broadening– and the line width decreases with increasing frequency. In order to guide the discussion we have included observed line widths for C$n\alpha$ transitions for Cas A (Kantharia et al., 1998; Payne et al., 1994), Cyg A (Oonk et al., 2014) and M82 (Morabito et al., 2014b) .

When the Doppler core dominates, CRRLs observations provide both an

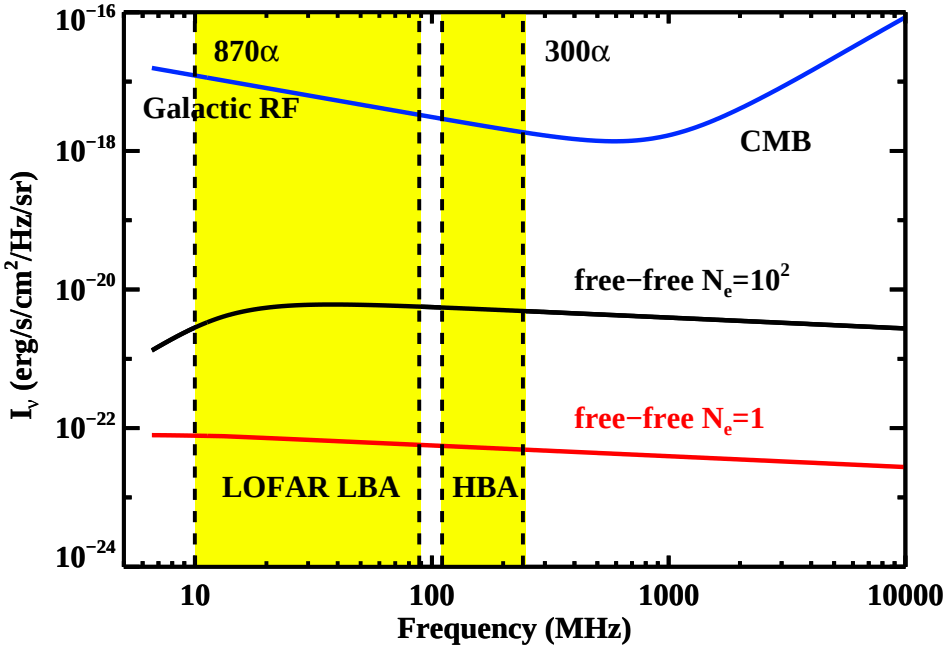

Figure 5.2: A comparison between the continuum radiation fields. The galactic synchrotron radiation field dominates over the free-free cloud continuum at $T_e = 100$ K. Therefore, the strong background approximation is valid for the low temperature cases considered in this analysis. The yellow zone marks the range in frequency observable by LOFAR.

upper limit on the gas temperature and an upper limit on the turbulent velocity of the diffuse ISM (cf. Equations 5.17 and 5.16). For typical parameters of the turbulent ISM (1 km s^{-1}), turbulence dominates over thermal velocities when $T_e \lesssim 700$ K.

Radiation broadening and collisional broadening show a very similar dependence on n and it is difficult to disentangle these two values from CRRLs observations. For the Galactic radiation field (i.e. synchrotron spectrum with $T_0 = 1000$ K at 100 MHz), the two processes contribute equally to the line width at a density $N_e \approx 0.03$ cm^{-3} (Figure 5.3). Low frequency observations can, thus, provide an upper limit on the density and radiation field. As illustrated in Figure 5.3, the transition from a Doppler to a Lorentzian broadened line is quite rapid (in frequency space) but the actual value depends on the physical conditions of the cloud (i.e. T_e, N_e, T_0 and $\langle v_{RMS} \rangle$).

In Figure 5.3 we can see that the RRLs from Cas A and Cyg A fall in a region of the diagram corresponding to densities lower than about 0.1 cm^{-3}

and the detection in M82 corresponds to either higher densities, to a much stronger radiation field or to the blending of multiple broad components. From observations at high frequencies, it is known that the lines observed towards Cas A are the result of three components at different velocities in the Perseus and Orion arms. Therefore, the physical parameters obtained from line widths should be taken as upper limits.

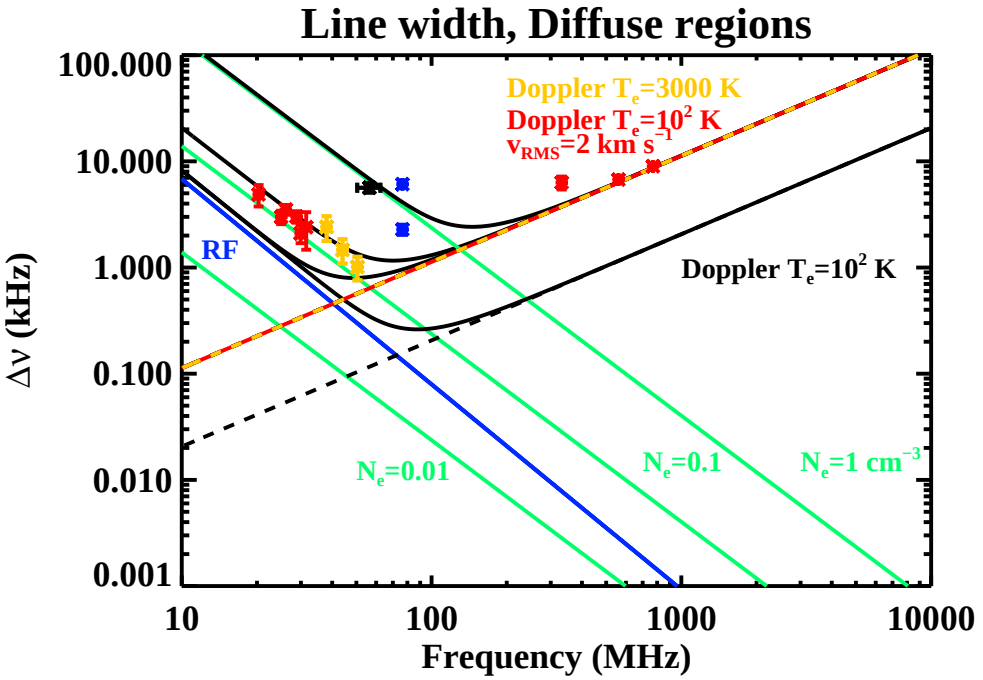

Figure 5.3: A comparison between broadening produced by the Galactic radiation field (blue line), collisional broadening at $N_e = 1,\ 0.1$ and 0.01 cm^{-3} (green lines) and thermal (Doppler) broadening at 100 K (black dashed line). The red and yellow curves correspond to a turbulent Doppler parameter $< v_{RMS} >^2 = 2$ km s^{-1} and $T_e = 300$ K, respectively. We include data for Cas A (Payne et al., 1994; Kantharia et al., 1998) as red points, Cyg A (Oonk et al., 2014) as yellow points, regions for the inner galaxy (Erickson et al., 1995) as blue points and data for M82 (Morabito et al., 2014b) as a black point.

When the line profile is dominated by the Doppler core, the ratio of the β to α line width is unity. However, radiation or collisional broadening affects the C$n\alpha$ and C$n\beta$ lines differently as the frequency decreases (as C$n\alpha$ and C$n\beta$ lines originate from different n levels). In Figure 5.4, we show the ratio $\Delta\nu(\beta)/\Delta\nu(\alpha)$. We notice that, when radiation broadening dominates the line width, this ratio goes to a constant value, independent of the background

temperature. From the radiation broadening formula (Equation 5.17) we see that $\Delta\nu(\beta)/\Delta\nu(\alpha) = (n_\beta/n_\alpha)^{-3\alpha_{pl}-2}$ and, for a power law $\alpha_{pl} = -2.6$, the ratio approaches $\Delta\nu(\beta)/\Delta\nu(\alpha) = 3.8$ as n increases. At high electron densities, collisional processes dominate the broadening of the lines. From Equation 5.16 the $\Delta\nu(\beta)/\Delta\nu(\alpha)$ ratio tends to a constant value of $(n_\beta/n_\alpha)^{\gamma_c} = 1.26^{\gamma_c}$. There is a temperature dependence in the exponent γ_c and, for electron temperatures less than 1000 K, we find that $\Delta\nu(\beta)/\Delta\nu(\alpha) \approx 3.1-3.6$ (see Table 5.3); similar to the radiation broadening case.

5.4.2 Integrated line to continuum ratio

As discussed in section 5.2.1, the line to continuum ratio of CRRL is often solved approximately, using equation (5.6). In this subsection, we will discuss when this approximation is justified. In this, we have to recognize that, under the conditions of the diffuse ISM, recombining carbon atoms are not in LTE (Paper I). Indeed, electrons can recombine to high levels due to dielectronic recombination, thus increasing the population in comparison to the LTE values. This increase in the level population leads to an increase in the values of the $b_n\beta_n$ coefficients in Equation 5.6 and, consequently, to an increase in the optical depth of the lines.

In Figure 5.5 we show the integrated line to continuum ratio as a function of level n for $T_e = 100$ K. We compare the values obtained using the approximated expression given in Equation 5.6 (red lines) and by solving the radiative transfer equation (Equation 5.1, black lines). The agreement between the two approaches is good for levels $n \gtrsim 250$, since at these high levels the approximations that lead to Equation 5.6 are valid. For levels lower than $n \approx 250$, differences appear. In particular, at low electron densities ($N_e \approx 0.01$ cm^{-3}) results using Equation 5.6 show lines in absorption while the results derived from solving the radiative transfer equation predict lines in emission. The difference between the two approaches can be understood in terms of the excitation temperature (see Appendix). As can be seen in Figure 5.6, the red zones correspond to low n levels, where the excitation temperature is higher than the background continuum temperature and the lines appear in emission (despite the β_n being positive). At higher n values, $\beta_n < 0$ (yellow zones) and the excitation temperature is negative reflecting an inversion in the level population, consequently, lines appear in emission. While there is an inversion of the level population the line optical depths are too low ($\tau_l \sim 10^{-3}$) to produce a maser (cf. Equation 5.7). At even higher levels (blue zones in Figure 5.6), the excitation temperature is less than the background continuum temperature and the lines are in absorption. As the electron density increases, dielectronic recombination is less efficient and the levels for which β_n is negative shift to lower n values, resembling the values for hydrogenic level population (Hum-

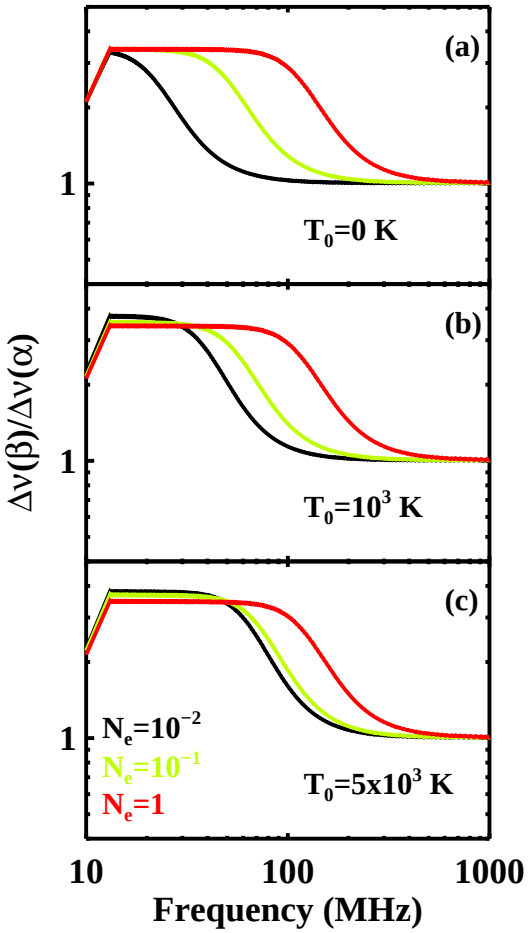

Figure 5.4: α and β line width transitions for diffuse regions as a function of frequency for different power law radiation fields. a) Without an external radiation field; b) a power law radiation field with $T_0 = 1000$ K and c) as b) for $T_0 = 5000$ K. The line widths correspond to electron densities of $N_e = 1,\ 0.1,$ and 0.01 cm^{-3} (red, green and black lines).

mer and Storey 1987, Paper I). Furthermore, for high quantum numbers and high densities, $\beta_n = 1$ and the excitation temperature is equal to the electron temperature of the gas.

From this analysis, we conclude that Equation 5.6 is valid for high ($n \gtrsim 250$) quantum numbers and the ratio of two lines depends only on the temperature and electron density of the cloud through the departure coefficients. In Figure 5.7, we demonstrate this by showing the integrated line to continuum ratio

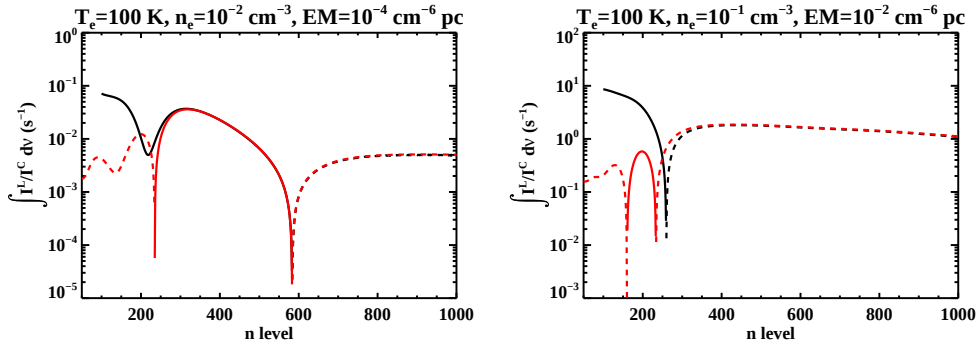

Figure 5.5: The line-to-continuum ratio of CRRL as a function of principal quantum number for $T_e = 100$ K and $N_e = 0.01$ and 0.1 cm^{-3} (left and right panels, respectively). The values were computed from the radiative transfer solution (Equation 5.1) and the galactic radiation field as a background. Black lines correspond to the result of solving the equation of radiative transfer while red lines correspond to the approximation expression given in Equation 5.6. At levels larger than $n \gtrsim 250$, the differences between the approximation (dashed) and the radiative transfer solution (solid) are minor.

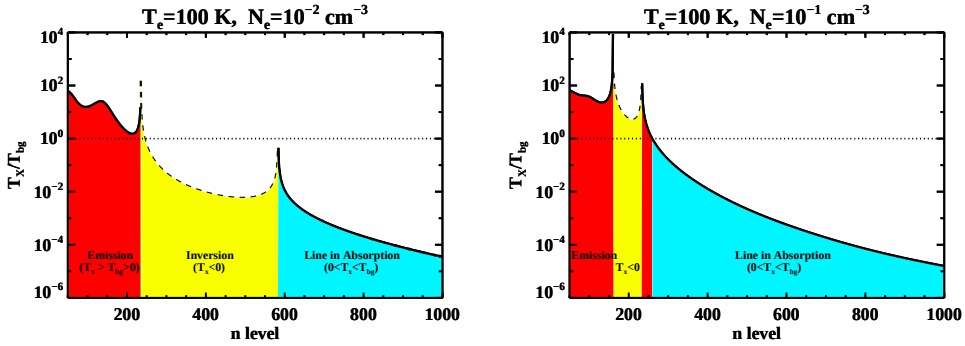

Figure 5.6: Ratio of the excitation to background temperature (T_X/T_{bg}) as a function of n. Lines are in emission in the red zone since $T_X > T_{bg}$ and in the yellow zone due to an inversion on the level population and $T_X < 0$. Lines appear in absorption in the light blue zone since the background temperature is (much) larger than the excitation temperature.

of C$n\alpha$ as a function of quantum number normalized to the level 500 (similar results can be obtained by using other n levels). The normalized ratio becomes smaller for high densities owing to the fact that $b_n\beta_n$ values change little with n as the levels are closer to equilibrium. As the electron density decreases, di-electronic recombination is more efficient in overpopulating intermediate levels

(Paper I) producing large changes in the values of the ratios.

5.4.3 CRRLs as diagnostic tools for the physical conditions of the ISM

5.4.3.1 Line Ratios

We have already discussed the use of the line width to constrain the properties of the emitting/absorbing gas. As figure 5.7 illustrates, line ratios are very sensitive to the physical conditions in the gas. Moreover, the use of line ratios "cancels out" the dependence on the emission measure. Here, we demonstrate the use of line ratios involving widely different n's as diagnostic tools in "ratio vs. ratio" plots. As an example, we show three line ratios in Figure 5.8, normalized to $n = 500$. The lines are chosen to sample the full frequency range of LOFAR and the different regimes (collisional, radiative) characteristic for CRRLs. The $n = 300,\ 400,\ 500$ lines are a particularly good probe of electron density for regions with temperature less than about 100 K. The use of the $n = 500$ level does not affect our results and other levels (e.g. $n = 600$ or 800) may be used for computing the fractions. We note that in a limited but relevant electron density range ($N_e \sim 1 - 5 \times 10^{-2}$ cm^{-3}), these lines can be good tracers of temperature. At higher densities, the departure coefficients approach unity and the ratios tend to group in a small region of the plot and the use of the ratios as probes of temperature requires measurements with high signal to noise ratio to derive physical conditions from the observations.

5.4.3.2 The Transition from Absorption to Emission

In Paper I, we discussed the use of the level where lines transition from emission to absorption (n_t) as a constraint on the density of a cloud (Figure 5.9). The limited observations in the Galactic plane (Erickson et al., 1995; Kantharia and Anantharamaiah, 2001) indicate that $400 > n_t > 350$ and n_t depends on both temperature and density. The transition level can be used to estimate the electron density for electron densities lower than about 10^{-1} cm^{-3}. For increasing electron density it becomes more difficult to constrain this quantity from the transition level alone.

5.4.3.3 Line Ratios as a Function of Δn

Combining observations of C$n\alpha$ lines with C$n\beta$ and C$n\gamma$ lines can provide further constraints on the physical parameters of the cloud. In Figure 5.10 we show the α-to-β ratio of the integrated line to continuum ratio as a function of frequency. Recall that C$n\alpha$ and C$n\beta$ lines observed at al-

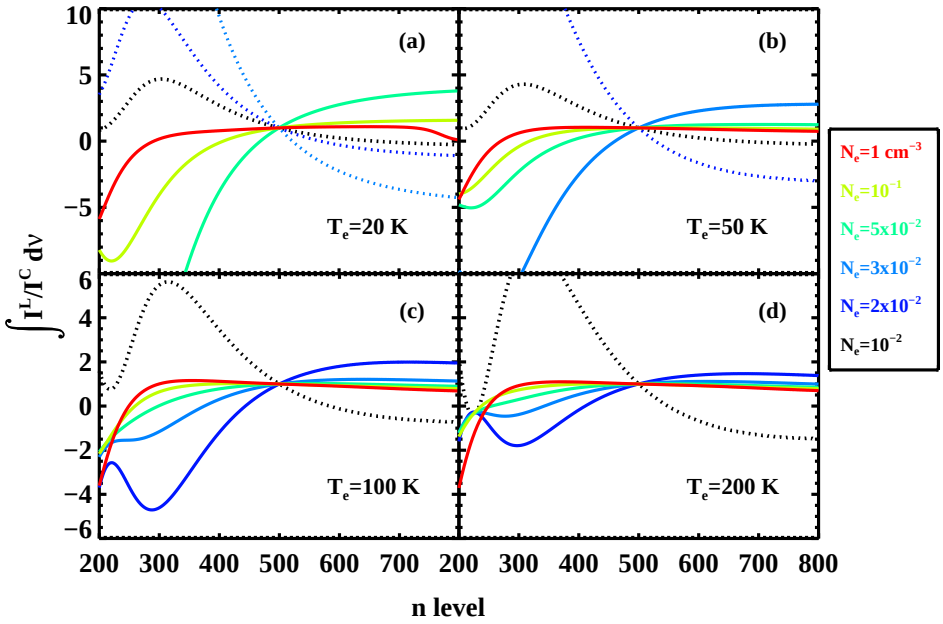

Figure 5.7: Integrated line to continuum ratio normalized to the value at the level $n = 500$ for $T_e = 20,\ 50,\ 100,$ and 200 K. Dotted lines indicate that the C500α line is in emission. The values have been computed considering radiative transfer effects (Equation 5.1).

most the same frequency probe very different n levels ($n_\alpha = 1.26 n_\beta$). Figure 5.10 shows that both electron density and temperature are involved. At high n levels the $b_n\beta_n$ are approximately unity and the α-to-β approaches $M(1)/2M(2) \approx 0.1908/0.0526 = 3.627$ (Equation 5.6) making the ratio less useful to constrain temperature and electron density. However, even at high n, this ratio does remain useful for investigating the radiation field incident upon the CRRL emitting gas.

5.4.3.4 The CRRL/[CII] Ratio

The [CII] 158 μm is the dominant cooling line of diffuse clouds and acts as a thermostat regulating the temperature (Hollenbach and Tielens, 1999). In realistic models of the ISM of galaxies (e.g. Wolfire et al. 1995), the pho-

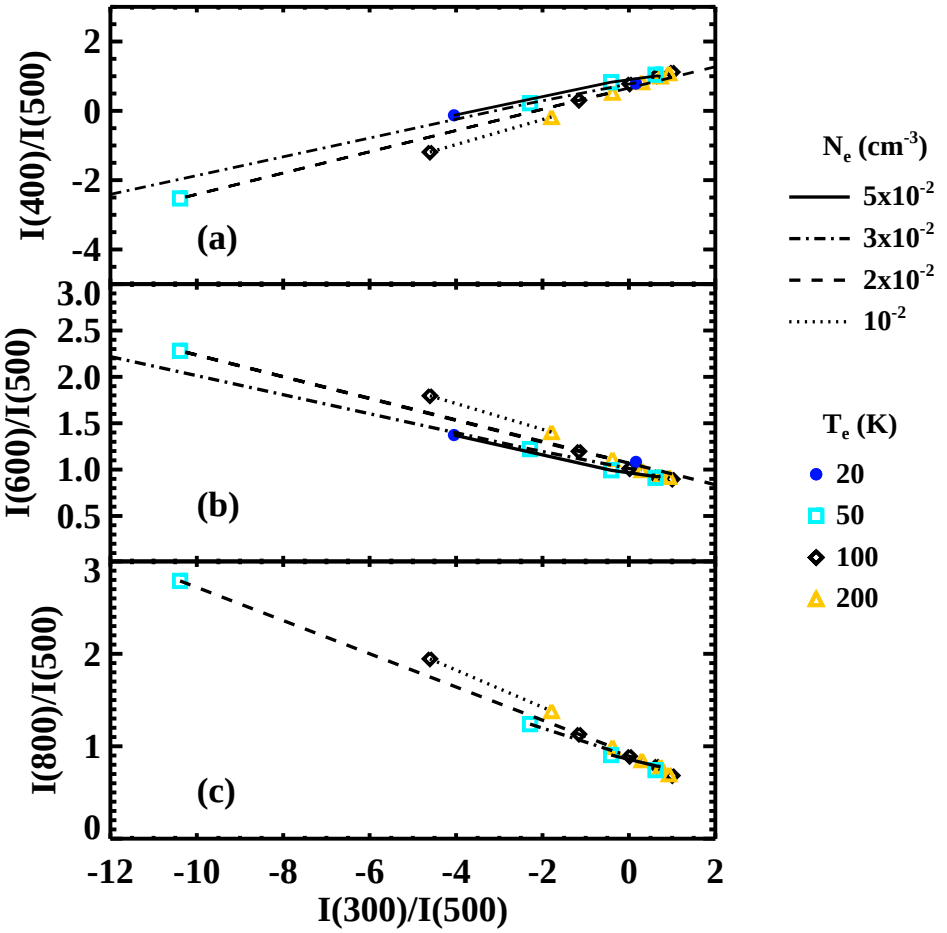

Figure 5.8: Example ratio diagnostic plots for different electron temperatures and densities. Cyan points are at $T_e = 50$ K, black points for $T_e = 100$ K and orange points for $T_e = 200$ K. Different densities are joined by: dotted lines ($N_e = 10^{-2}$ cm^{-3}), dashed lines ($N_e = 2 \times 10^{-2}$ cm^{-3}), dashed-dotted lines ($N_e = 3 \times 10^{-2}$ cm^{-3}) and continuous lines ($N_e = 5 \times 10^{-2}$ cm^{-3}). (a) Ratio of the integrated line to continuum for levels 400 and 500 vs. 300 to 500 ratio. (b) Ratio of the integrated line to continuum for levels 600 and 500 vs. 300 to 500 ratio. (c) Ratio of the integrated line to continuum for levels 800 and 500 vs. 300 to 500 ratio.

toelectric effect on polycyclic aromatic hydrocarbon molecules and very small grains heats the gas and the cooling by the [CII] 158 μm line adjust to satisfy the energy balance. As the heating is a complicated function of the physical

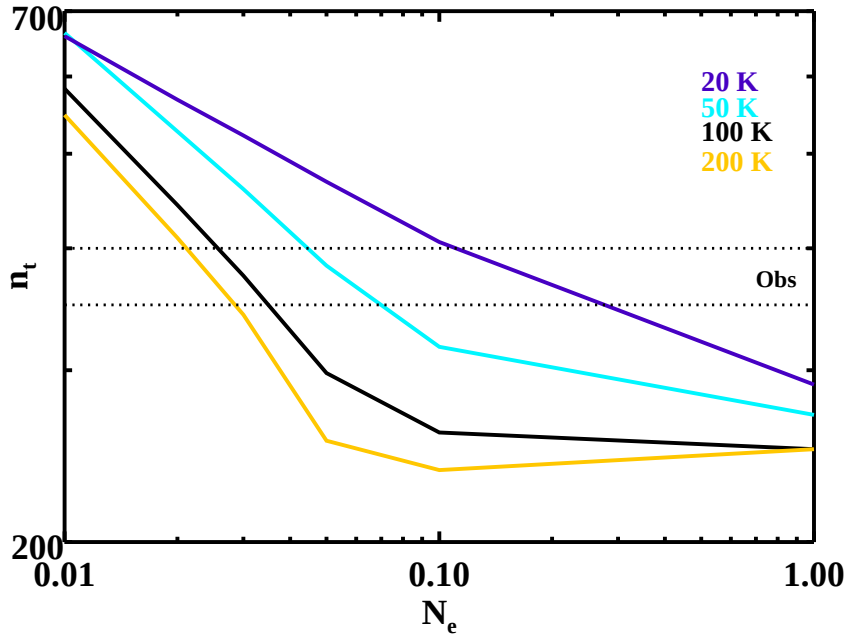

Figure 5.9: Level where lines transition from emission to absorption (n_t) as a function of electron density (N_e) for $T_e = 50,\ 100$ and 200 K. The horizontal dashed lines mark the limits as suggested by observations of CRRLs in the Galaxy.

conditions (Bakes and Tielens, 1994), models become very involved. Here, we sidestep this issue and we calculate the [CII] 158 μm intensity as a function of N_e and T_e for a uniform cloud. The intensity scales with the column density of carbon ions, N_{C^+}, and temperature. In contrast, the CRRLs scale with the emission measure divided by $T_e^{5/2}$ (cf. Equation 5.6). Hence, the ratio of the CRRL to the 158 μm line shows a strong dependence on temperature (and electron density), but for a constant density this ratio does not depend on column density. In Figure 5.11 we show the CRRL/[CII] ratio as a function of density for different temperatures. For the physical conditions relevant for diffuse clouds, the CRRL/[CII] ratio is a powerful diagnostic tool.

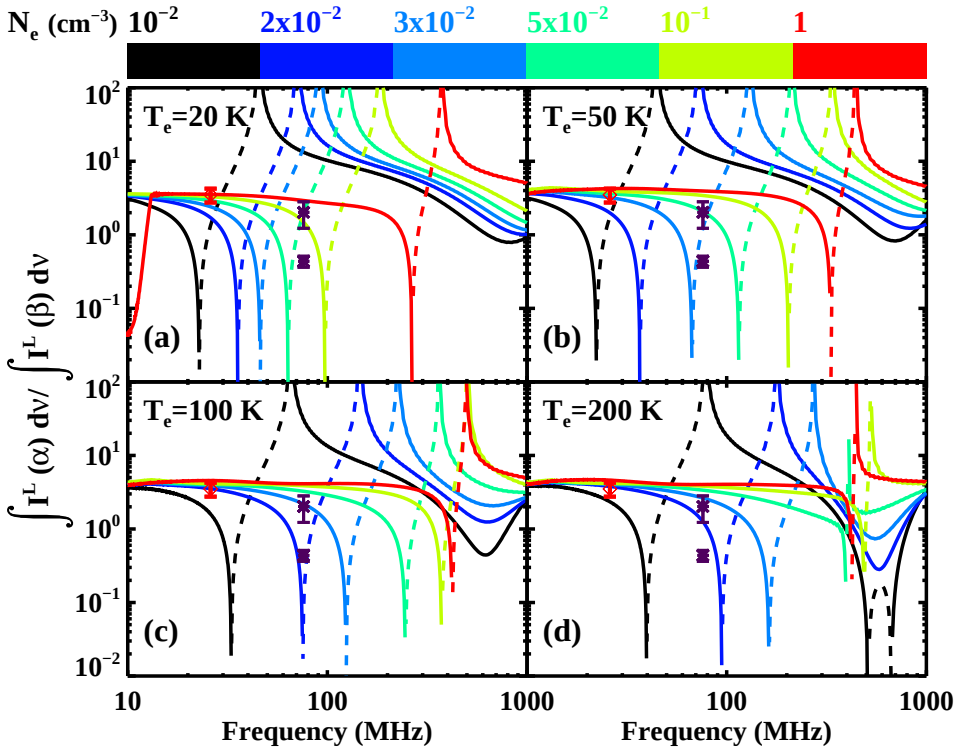

Figure 5.10: Comparison between the integrated line to continuum $I(\alpha)/I(\beta)$ ratio as a function of frequency for different densities (colorbar); dashed lines indicate that the ratio is negative, the color of the lines is the same as in Figure 5.7. The values for the ratios approach the LTE value of 3.6 at high n. Large differences can be observed for different densities because lines observed at the same frequency correspond to different levels. We have included the data points for Cas A from Stepkin et al. (2007) (red point) and for inner Galaxy from Erickson et al. (1995) (dark blue points).

5.5 On the Observed Behavior of CRRLs

5.5.1 General considerations

CRRLs have been observed towards two types of regions: high density PDRs and diffuse clouds (Gordon and Sorochenko, 2009). In general, low frequency CRRLs are observed in absorption with values for the integrated line to con-

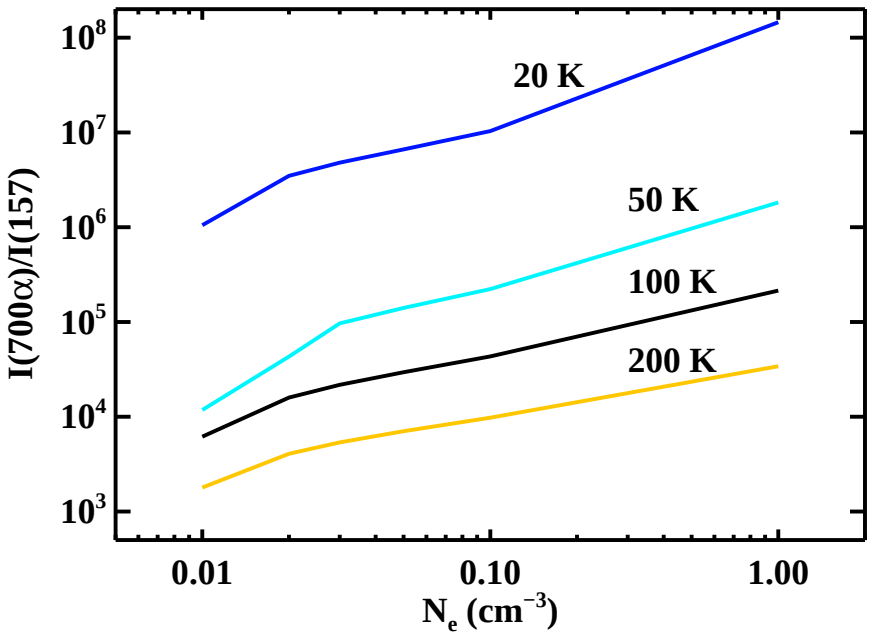

Figure 5.11: Ratio of the line to continuum ratio, for $n = 700$, to the [CII] 158 μm line as a function of density. This example ratio shows how CRRL/[CII] can be used as a diagnostic plot to constrain electron density and temperature.

tinuum ratio in the range of 1 to 5 Hz and a peak line-to-continuum ratio of $\sim 10^{-4}$ to 10^{-3} (Erickson et al., 1995; Kantharia et al., 1998; Roshi et al., 2002; Oonk et al., 2014).

In order to observe CRRLs, carbon atoms must be singly ionized. In HII regions carbon is found in higher stages of ionization and recombination lines of the type we study here are not expected. In photodissociation regions of high density, carbon atoms transition from ionized to neutral and into molecular (CO) around a visual extinction $A_V \approx 4$ mag depending on the density and UV field. Assuming $A_V = N_H/1.9 \times 10^{21}$ mag cm^{-2} we can estimate the maximum column density of carbon that can be expected for such a transition region. Assuming that carbon is fully ionized and a carbon abundance of 3×10^{-4}, we obtain $A_V = N_C/5.7 \times 10^{17}$ mag cm^{-2} and the column density of carbon is $N_C = 2.4 \times 10^{18}$ cm^{-2}.

As mentioned in Section 5.2.1, CRRLs produced in clouds with high temperatures are faint due to the strong dependence of the line-to-continuum ratio on temperature. Therefore, regions of low temperature are favored to be observed using low frequency recombination lines. These two considerations (low

T_e and N_e) set a range of electron density and temperature for which CRRLs are easier to detect. Specifically, consider a medium with two phases in pressure equilibrium. From Equation 5.4, the optical depth ratio scales then with:

$$\frac{\tau_1}{\tau_2} \propto \frac{N_{e,1}^2}{T_{e,1}^{5/2}} \frac{T_{e,2}^{5/2}}{N_{e,2}^2} \frac{(b_n\beta_n)_1}{(b_n\beta_n)_2} \frac{L_1}{L_2} \propto \left(\frac{T_2}{T_1}\right)^{9/2} \frac{(b_n\beta_n)_1}{(b_n\beta_n)_2} \frac{L_1}{L_2}. \tag{5.1}$$

For parameters relevant for the CNM and WNM ($T_{e,1} = 80$ K, $T_{e,2} = 8000$ K, respectively, Tielens 2005), we have then $\tau_1/\tau_2 \sim 10^9 (b_n\beta_n)_1/(b_n\beta_n)_2 L_1/L_2$. Clearly, CRRLs will overwhelmingly originate in cold, diffuse clouds. Therefore, unlike 21 cm HI observations, analysis of CRRL observations is not hampered by confusion of CNM and WNM components.

The fact that low frequency recombination lines are observed in absorption sets a lower limit on the density for the clouds where CRRLs are produced. Our models show that at electron densities lower than 10^{-2} cm^{-3} and for temperatures lower than 200 K low frequency CRRLs are in emission.

5.5.2 Illustrative examples

In this section we illustrate the power of our models to derive physical parameters from observations of CRRLs. We selected observations towards Cas A as, to our knowledge, the clouds towards Cas A are the best studied using CRRLs. We then expand this illustration, by using observations of two regions observed towards the Galactic Center from Erickson et al. (1995).

5.5.2.1 Cas A

We begin our analysis with CRRLs detected towards Cas A from the literature (e.g. Payne et al. 1994; Kantharia et al. 1998; Stepkin et al. 2007). In Figure 5.12, we summarize the constraints from: the integrated line α to β ratio as a blue zone using the Stepkin et al. (2007) data. The transition from emission to absorption ($350 < n_t < 400$) is shown as the green zone. The 600 to 500 ratio vs. 270 to 500 ratio is included as the red zone[3]. Finally, the yellow zone is the intersection of all the above mentioned zones.

The line width does not provide much of an additional contraint. For Cas A, with an observed line width of 6.7 kHz at $\nu = 560$ MHz (Kantharia et al., 1998) the implied gas temperature would be $T_e = 3000$ K and actually we expect that the line is dominated by turbulence with $< v_{RMS} > \approx 2$ km s^{-1} (Figure 5.3). Likewise, the Cas A observations from Payne et al. (1994); Kantharia et al.

[3]We use the $n = 270$ data from Kantharia et al. (1998) and estimate the data at $n = 600$ from Payne et al. (1994) and analogous plots as in Figure 5.8.

(1998) are of little additional use as we arrive at $N_e \lesssim 0.1$ cm^{-3} and $T_0 \lesssim$ 2000 K.

Perusing Figure 5.12, we realize that the α to β line ratio does not provide strong constraints due to the frequency at which the lines were observed as all the models converge to the high density limit (Figure 5.10). The transition level from emission to absorption (n_t) restricts the allowed models to an area in the N_e vs T_e plane. However, at low temperatures ($T \lesssim 50$ K), the constraining power of n_t is limited. The "ratio vs. ratio" plots can be quite useful in constraining both the electron density and the temperature of the line producing cloud, as we have illustrated here.

The results of our models show that the properties of the cloud are well restricted in density ($N_e = 2 - 3 \times 10^{-2}$ cm^{-3}) – corresponding to H-densities of $\sim 100 - 200$ cm^{-3} – but somewhat less in temperature ($T_e = 80 - 200$ K). We emphasize, though, that these results are ill-defined averages as the CRRLs towards Cas A are known to be produced in multiple velocity components which are blended together. In addition, preliminary analysis of the LOFAR data indicates variations in CRRL optical depth on angular scales significantly smaller than the beam sizes used in the observational data from the previous literature studies quoted here. Nevertheless, this example illustrates the power of CRRL observations to measure the physical conditions in diffuse interstellar clouds.

5.5.2.2 Galactic Center Regions

As a second example, we analyze observations of clouds detected towards regions in the galactic plane (Erickson et al., 1995). Due to the scarceness, low spatial resolution and limited frequency coverage of the data available in the literature our results should be taken with care and considered illustrative. We chose two regions with good signal to noise measurements (SNR> 10). In Table 1, we show the line parameters for C441α and C555β lines from Erickson et al. (1995) with a beam size of 4°.

Table 5.1: Selected values for C$n\alpha$ and C$n\beta$ lines for regions observed by Erickson et al. (1995).

Name	$\tau(441\alpha)$ $\times 10^{-3}$	$\Delta v(441\alpha)$ km s^{-1}	$\tau(555\beta)$ $\times 10^{-3}$	$\Delta v(555\beta)$ km s^{-1}
G000.0+0	0.73±0.03	24±1	0.35±0.03	24±2
G002.0-2	0.97±0.08	9±1	0.75±0.04	25±2

In Figure 5.13, we summarize the constraints imposed by the integrated α to β line ratio as a blue zone, the transition from emission to absorption (n_t

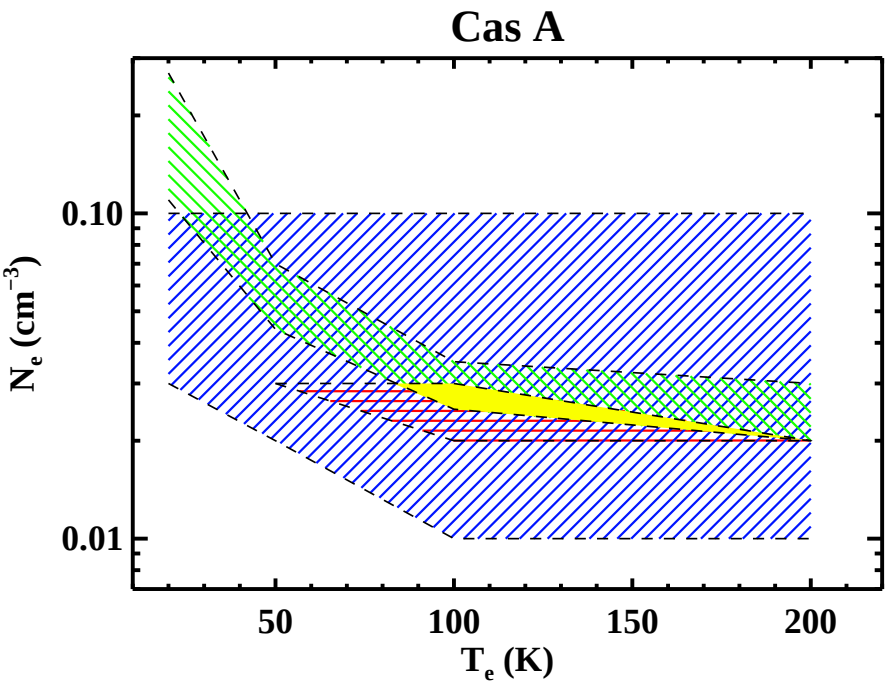

Figure 5.12: Summary of the constraints for the C$n\alpha$ and C$n\beta$ transitions from Stepkin et al. (2007) towards Cas A. The blue zone shows the region allowed by the integrated α to β ratio constraints. The green zone is the region allowed from the n_t constraints. The red zone is the region allowed from the 600 to 500 ratio vs. 270 to 500. The yellow zone shows the overlap region from all the constraints. The electron density is well constrained to be $2 - 3 \times 10^{-2}$ cm^{-3}. The temperature is constrained to be within 80 and 200 K.

level) as a green zone (we estimate to be $350 < n_t < 400$) and the integrated line-to-continuum to the $I(158\ \mu m)$ ratio as the orange zone.

From the line widths towards the lines of sight in Table 1 an upper limit to the density can be estimated by assuming pure collisional broadening, as shown in Section 5.2.3. The upper limits on density are $N_e \leq 1.5$ cm^{-3} for G000.0+0 and $N_e \leq 0.5$ cm^{-3} for G002.0-2. The constraint is even more strict when considering that part of the broadening must be produced by the Galactic radiation field. Assuming no collisional broadening, the upper limits on the background temperatures for the regions are $T_e \leq 4 \times 10^4$ K for G000.0+0 and $T_e \leq 1.5 \times 10^4$ K for G002.0-2. These are strict upper limits as the observations from Erickson et al. (1995) were performed with large beams and the observed lines are likely produced by several "clouds" in the beam.

We estimate the value for $I(158\ \mu$m) to be $8 - 12 \times 10^{-5}$ erg s cm^{-2} sr^{-1}

from *COBE* data (Bennett et al., 1994). Since the data from Erickson et al. (1995) is for the C441α line, we created a diagnostic plot similar to that in Figure 5.11 for the level 441. We obtain for G000.0+0 T_e has a value between 20 and 60 K and N_e between 4×10^{-2} and 1×10^{-1} cm^{-3}. For G002.0-2, we obtain $T_e = 20$ to 80 K and $N_e = 4 \times 10^{-2} - 1 \times 10^{-1}$ cm^{-3}. With these values and using Equation 5.7 we determine lengths of 2 to 19 pc for G000.0+0 and 1 to 9 pc for G002.0-2. It is clear from Figure 5.13 that the n_t level (green zone in the plots) and the integrated α to β line ratio provide similar constrains in the N_e vs. T_e plane. For the strongest constraint comes from n_t, since the errors in the measurements do not provide strong limits on the α-to-β line ratio. As the error bars are rather large the derived constraints – given above – are not very precise. Nevertheless, the inherent power of CRRL for quantitative studies of diffuse clouds in the ISM is quite apparent.

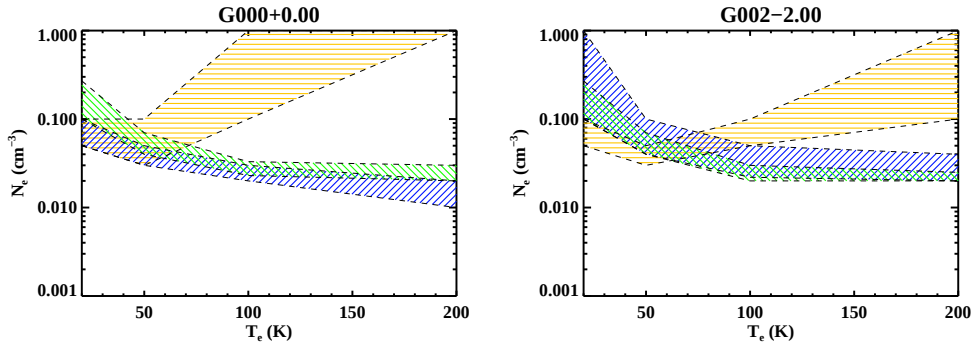

Figure 5.13: Same as Figure 5.12 for regions towards the Galactic center (data from Erickson et al. 1995). The α to β ratio constraints is shown as a blue region. The constraints derived from n_t are shown as a green zone. In addition, we have added the constraint from CRRL to [CII] 158 μm ratio as the orange shaded zone.

5.5.3 Discussion

As the examples of Cas A and G000.0+0 and G002.0-2 show, a large amount of relevant physical information on the properties of the clouds can be obtained from CRRL measurements, despite the scarceness of the data used here. The α-to-β line ratios can provide powerful constraints as long as the frequency observed is higher than 30 MHz. As illustrated by our Cas A example, the CRRL ratio plots can be extremely useful in constraining the electron density and temperature, and lines with a large separation in terms of quantum number are expected to be the most useful ratios. As illustrated in Figure 5.8, ratios between levels around 300 and 500 can provide direct constraints or indirect

constraints by using, in addition, the n_t value. An advantage of using ratios is that they only depend on the local conditions and beam filling factors are of little concern.

5.6 Summary and Conclusions

In this paper we have analyzed carbon radio recombination line observations. Anticipating the LOFAR CRRL survey, we focus our study in the low frequency regime, corresponding to transitions between lines with high principal quantum number. We have studied the radiative transfer of recombination lines and the line broadening mechanisms in the most general form.

Our results show that line widths provide constraints on the physical properties of the gas. At high frequencies the observed line widths provide limits on the gas temperature and on the turbulent velocity of the cloud. At low frequencies, observed line widths provide constraints on the electron density of the intervening cloud and on the radiation field that the cloud is embedded in. Using the departure coefficients obtained in Paper I, we analyzed the behavior of the lines under the physical conditions of the diffuse ISM. Integrated optical depths provide constraints on the electron density, electron temperature and the emission measure or size of the cloud. The use of CRRLs together with [CII] at 158 μm can constrain the temperature.

As an illustration of the use of our models, we have analyzed existing data in low frequency CRRLs towards Cas A and the inner galaxy to derive physical parameters of the absorbing/emitting clouds (Payne et al., 1994; Stepkin et al., 2007; Erickson et al., 1995).

Our models predict that detailed studies of CRRLs should be possible with currently available instrumentation. By using realistic estimates for the properties of the diffuse ISM we obtain optical depths that are within the capabilities of LOFAR and of the future Square Kilometer Array (Oonk et al., 2015b). Given the clumpy nature of the ISM, we encourage observations with high angular resolution. Observations with large beams are biased towards line of sights with large optical depth and narrow lines, and these happen to be clouds of low density for a given temperature. High spectral resolution is also encouraged in order to distinguish multiple components along the line of sights. Once the temperature and the density have been determined, the observed intensities yield the C^+ column density which can be combined with the HI column density from 21 cm observations to determine the gas phase carbon abundance.

The main conclusions of our work are:

1) CRRLs provide a powerful probe of the physical conditions of diffuse interstellar clouds.

2) Meaningful constraints on gas properties can be derived from combining

information on the location of the transition from emission to absorption, α-to-β ratios and α-line ratios spread in frequency. Further limits are provided by the low frequency line width.

3) Comparison of CRRLs with [CII] 158 μm line measured by COBE (Bennett et al., 1994), BICE (Nakagawa et al., 1998) and Herschel (GOT C+;Pineda et al. 2013); in addition to new observations with the German Receiver for Astronomy at Terahertz Frequencies (GREAT; Heyminck et al. 2012) on board of SOFIA, will provide important constraints primarily on the temperature, but also aid in further constraining the density and size of diffuse clouds.

A List of Symbols

Table 5.2: List of Symbols

Symbol	Descritpion
$A_{n'n}$	Einstein coefficient for spontaneous transitions
$A_{3/2,1/2}$	Spontaneous transition rate of the carbon fine structure line $^2P_{3/2}$-$^2P_{1/2}$
$a(T_e)$	Fitting coefficient for collisional broadening
$B_{nn'}$	Einstein coefficient for stimulated transition
b_n	Departure coefficient for level n
$B_\nu(T)$	Planck function at frequency ν for a temperature T
$C_{n'n}$	Rates for energy changing collisions between level n' and n
C$n\alpha$	Carbon recombination line with $\Delta n = 1$
c	Speed of light
$EM_{\mathrm{C+}}$	Emission measure of carbon ions
h	Planck constant
$I_0(\nu)$	Intensity of the background continuum
I_ν^{line}	Intensity of the line
I_ν^{cont}	Intensity of the continuum
I_{158}	Intensity of the fine structure line of carbon at 158 μm
j_ν^l	line emission coefficient
j_ν^c	continuum emission coefficient
k	Boltzmann constant
k_ν^l	line absorption coefficient
k_ν^c	continuum absorption coefficient
L	Pathlength of the cloud
$M(\Delta n)$	Approximation factor for the oscillator strength, as given by Menzel (1968)
m_C	Mass of a carbon atom
$N_{3/2}^+$	Level population of carbon ions in the $^2P_{3/2}$ core
$N_{\mathrm{C+}}$	Number density of carbon ions
N_e	Electron density
n	Lower principal quantum number
n'	Upper principal quantum number
n_t	Level where the observed lines transition from emission to absorption
R	Ratio between the fine structure ($^2P_{3/2}$-$^2P_{1/2}$) level population and the fine structure level population in LTE
Ry	Rydberg constant

Continued on next page

Table 5.2 – *Continued from previous page*

Symbol	
T_0	Temperature of power law background spectrum at frequency ν_0
t_n	Ratio of radiation to collisional broadening
T_X	Excitation temperature
T_e	Electron temperature
$\langle v_{RMS} \rangle$	RMS turbulent velocity
$\alpha_{1/2}$	Fraction of carbon ions in the $^2P_{1/2}$ level
α_{pl}	Exponent of the power law background spectrum
$\beta_{nn'}$	Correction factor for stimulated emission
β_{158}	Correction for simulated emission to the [CII] fine structure line $^2P_{3/2}$-$^2P_{1/2}$
$\gamma_c(T_e)$	Fitting coefficient for collisional broadening
γ_e	De-excitation rate for carbon ions in the $^2P_{3/2}$ core due to collisions with electrons
γ_H	De-excitation rate for carbon ions in the $^2P_{3/2}$ core due to collisions with hydrogen atoms
Δn	$n'-n$, difference between the upper and lower principal quantum number
$\Delta\nu_D$	Doppler width
$\Delta\nu_{rad}$	Radiation broadening
$\Delta\nu_{col}$	Collisional broadening
ν	Frequency of a transition
η	Correction factor to the Planck function due to non-LTE level population
τ_{158}	Optical depth for the [CII] fine structure line $^2P_{3/2}$-$^2P_{1/2}$
τ_ν^l	Optical depth of the line
τ_ν^c	Optical depth of the continuum
τ_ν^{total}	Sum of τ_ν^l and τ_ν^c
$\phi(\nu)$	Line profile
ν_0	Reference frequency for the power law background spectrum

B Radiative Transfer

The radiative transfer equation for a line in the plane parallel approximation is given by:

$$\frac{dI_\nu}{dx}(x) = -k_\nu(x)I_\nu(x) + j_\nu(x) \quad \text{(B1)}$$

$$k_\nu = k_\nu^l + k_\nu^c \quad \text{(B2)}$$

$$j_\nu = j_\nu^l + j_\nu^c, \quad \text{(B3)}$$

where k_ν^l is the line absorption coefficient, k_ν^c is the continuum absorption coefficient, j_ν^l is the line emission coefficient, j_ν^c is the continuum emission coefficient and $I_\nu(x)$ is the specific intensity of a nebula at a frequency ν as a function of depth in the cloud x. The line absorption and emission coefficients are given by:

$$j_\nu^l = \frac{h\nu}{4\pi} A_{n'n} N_{n'} \phi(\nu), \quad \text{(B4)}$$

$$k_\nu^l = \frac{h\nu}{4\pi} \left(N_n B_{nn'} - N_{n'} B_{n'n}\right) \phi(\nu), \quad \text{(B5)}$$

where $N_{n'}$ is the level population of a given upper level and N_n is the level population of the lower level; ν is the frequency of the transition and $A_{n'n}$, $B_{n'n}(B_{nn'})$ are the Einstein coefficients for spontaneous and stimulated emission (absorption), related to each other by:

$$A_{n'n} = \frac{2h\nu^3}{c^2} B_{n'n}, \quad \text{(B6)}$$

$$B_{nn'} = \frac{\omega_{n'}}{\omega_n} B_{n'n}. \quad \text{(B7)}$$

The factor $\phi(\nu)$ in Equation B4 is the normalized line profile ($\int \phi(\nu)\mathrm{d}\nu = 1$). The effects on the emission are analyzed in Section 5.2.3. Here, we assume that j_ν is evaluated at the line center where the frequency of the transition is ν_0 and omit the $\phi(\nu_0)$ factor. Note that due to the normalization, $\phi(\nu_0) < 1$. Under thermodynamic equilibrium the level population of a level n ($N_n(LTE)$) is given by:

$$N_n(LTE) = N_e N_{ion} \left(\frac{h^2}{2\pi m_e k T_e}\right)^{1.5} \frac{\omega_n}{2\omega(i)} e^{\chi_n}, \chi_n = \frac{hcZ^2 Ry}{n^2 k T_e}, \quad \text{(B8)}$$

where N_e is the electron density in the nebula, T_e is the electron temperature, N_{ion} is the ion density, m_e is the electron mass, h is the Planck constant, k is the Boltzmann constant, c is the speed of light, Ry is the Rydberg constant and ω_n is the statistical weight of the level n ($\omega_n = 2n^2$, for hydrogen). In the ISM,

levels can be out of local thermodynamic equilibrium (Paper I). The level population can then be described by the departure coefficients $b_n = N_n/N_n(LTE)$, i. e. the ratio of the level population of a given level to its LTE value. From the definitions of j_ν^l and k_ν^l, we can write the emission and absorption coefficients in terms of the departure coefficients:

$$j_\nu^l = j_\nu^l(LTE)b_n, \tag{B9}$$

$$k_\nu^l = \frac{h\nu}{4\pi}\left(b_n N_n(LTE)B_{nn'} - b_{n'}N_{n'}(LTE)B_{n'n}\right), \tag{B10}$$

$$= k_\nu^l(LTE)b_n\frac{1-\frac{b_{n'}}{b_n}e^{-h\nu/kT_e}}{1-e^{-h\nu/kT_e}}. \tag{B11}$$

The correction factor for stimulated emission/absorption, $\beta_{nn'}$, is:

$$\beta_{nn'} = \frac{1-\frac{b_{n'}}{b_n}e^{-h\nu/kT_e}}{1-e^{-h\nu/kT_e}}. \tag{B12}$$

Deviations from equilibrium can be also described in terms of the excitation temperature (T_X) of a transition, defined as:

$$\frac{N_{n'}/\omega_{n'}}{N_n/\omega_n} = \exp\left(\frac{-h\nu}{kT_X}\right). \tag{B13}$$

It is easy to see that T_X is related to $\beta_{nn'}$ by:

$$\beta_{nn'} = \frac{1-e^{-h\nu/kT_X}}{1-e^{-h\nu/kT_e}}. \tag{B14}$$

Clearly, under LTE conditions the excitation temperature approaches the value of the electron temperature, i.e. $T_X = T_e$. The description of the level population in terms of T_X is useful to explain the behavior of the lines as we show in Section 5.3. For a homogeneous cloud, the radiative transfer equation can be solved. At a given frequency, the observed flux has contributions from both the line and the continuum; which can be written as:

$$I_\nu^{total} = \frac{j_\nu^c + j_\nu^l}{k_\nu^c + k_\nu^l}\left[1-e^{-(\tau_\nu^c+\tau_\nu^l)}\right] + I_0(\nu)e^{-(\tau_\nu^c+\tau_\nu^l)}, \tag{B15}$$

$$I_\nu^c = \frac{j_\nu^c}{k_\nu^c}(1-e^{-\tau_\nu^c}) + I_0(\nu)e^{-\tau_\nu^c}, \tag{B16}$$

where a background continuum source, $I_0(\nu)$ has been introduced. The coefficients $\tau_\nu^x = \int k_\nu^x(s)ds$ are the optical depth for x of either the continuum or the line. Assuming homogeneity $\tau_\nu^x = k_\nu^x L$, where L is the length along the line of

sight of the cloud, we can separate the contribution from the line itself since it is given by:

$$I_\nu^{line} = I_\nu^{total} - I_\nu^c \tag{B17}$$

$$I_\nu^{total} - I_\nu^{continuum} = \frac{j_\nu^c + j_\nu^l}{k_\nu^c + k_\nu^l}(1 - e^{-\tau_\nu^{total}}) + I_0(\nu)e^{-\tau_\nu^{total}} - \frac{j_\nu^c}{k_\nu^c}(1 - e^{-\tau_\nu^c}) - I_0(\nu)e^{-\tau_\nu^c} \tag{B18}$$

$$\tau_\nu^{total} = \tau_\nu^c + \tau_\nu^l. \tag{B19}$$

We can write the line contribution in terms of the source function (S_ν) by using Kirchoff's law [$j_\nu = \kappa_\nu B_\nu(T_e)$, with $B_\nu(T_e)$ the Planck function]:

$$S_\nu = \frac{j_\nu^c + j_\nu^l}{k_\nu^c + k_\nu^l} = \left[\frac{k_\nu^c + b_{n'}k_\nu^l(LTE)}{k_\nu^c + b_n\beta_{nn'}k_\nu^l(LTE)}\right] B_\nu(T_e). \tag{B20}$$

We identify a correction factor to the Planck function for departures from LTE:

$$\eta = \frac{k_\nu^c + b_{n'}k_\nu^l(LTE)}{k_\nu^c + b_n\beta_{nn'}k_\nu^l(LTE)}, \tag{B21}$$

as in e.g. Strelnitski et al. (1996) and Gordon and Sorochenko (2009).

With these definitions, we can write:

$$I_\nu^{line} = \eta B_\nu(T_e)(1 - e^{-\tau_\nu^{total}}) - B_\nu(T_e)(1 - e^{-\tau_\nu^c}) + I_0(\nu)e^{-\tau_\nu^c}\left(e^{-\tau_\nu^l} - 1\right), \tag{B22}$$

and the intensity of a line relative to the continuum is:

$$\frac{I_\nu^{line}}{I_\nu^{cont}} = \frac{\eta B_\nu(T_e)(1 - e^{-\tau_\nu^{total}}) + I_0(\nu)e^{-\tau_\nu^{total}}}{B_\nu(T_e)(1 - e^{-\tau_\nu^c}) + I_0(\nu)e^{-\tau_\nu^c}} - 1, \tag{B23}$$

In the absence of a background radiation field ($I_0 = 0$) this reduces to:

$$\frac{I_\nu^{line}}{I_\nu^{cont}} = \frac{\eta(1 - e^{-\tau_\nu^{total}})}{(1 - e^{-\tau_\nu^c})} - 1. \tag{B24}$$

In Section 5.2.3, we showed that under the conditions of the diffuse ISM the line profile is expected to be Lorentzian in shape, and, at the line center, $\phi(\nu_0) = 2/\pi\Delta\nu_L$ with $\Delta\nu_L$ the full width at half maximum (FWHM) of the line. This sets a range of physical parameters for which the approximation $|\tau_\nu^l| \ll 1$ is valid.

B.1 Doppler and Lorentzian broadening

Doppler broadening occurs due to turbulent motions in the gas and thermal motions is given by a Gaussian distribution with a Doppler width (Rybicki and Lightman, 1986):

$$\Delta\nu_D = \frac{\nu_0}{c}\sqrt{\frac{2kT}{m_{atom}} + \langle v_{RMS}\rangle^2}, \tag{B25}$$

where m_{atom} is the mass of the atom and $\langle v_{RMS}\rangle$ is the RMS turbulent velocity. The line profile as a function of frequency is given by the expression:

$$\phi_\nu^G(\nu) = \frac{1}{\Delta\nu_D\sqrt{\pi}}\exp -\left(\frac{\nu-\nu_0}{\Delta\nu_D}\right)^2. \tag{B26}$$

With this definition the FWHM is $\Delta\nu_D(\mathrm{FWHM}) = 2\sqrt{\ln(2)}\Delta\nu_D$. Note that Doppler broadening is dominated by turbulence for $T_e < 60.5\ (m_{atom}/m_H)\ (\langle v_{RMS}\rangle/\mathrm{km\ s^{-2}})^2$ K, here m_H is the mass of a proton.

The Lorentzian width of a line produced by a transition from a level n' to n is related to the net transition out of the levels (Shaver, 1975; Rybicki and Lightman, 1986):

$$\Gamma_{n'n} = \Gamma_{n'} + \Gamma_n, \tag{B27}$$

$$\Gamma_{n'} = \sum_{n<n'} A_{n'n} + \sum_{n\neq n'} N_e C_{n'n} + \sum_{n\neq n'} B_{n'n} I_\nu, \tag{B28}$$

$$= \Gamma_{natural} + \Gamma_{collisions} + \Gamma_{radiation} \tag{B29}$$

with an analogous formula for Γ_n. Here, we have to consider collisions with electrons and transitions induced by an external radiation field. This produces a Lorentzian line profile:

$$\phi_\nu^L(\nu) = \frac{\gamma}{\pi}\frac{1}{(\nu-\nu_0)^2+\gamma^2}, \tag{B30}$$

the FWHM is $\Delta\nu_L(\mathrm{FWHM}) = 2\gamma$. The width γ of a line transition between levels n and n' is given by $\gamma = (\Gamma_n + \Gamma_{n'})/4\pi$. For transitions between lines with $n \approx n'$ we have $\Gamma_n \approx \Gamma_{n'}$ and $\gamma \approx \Gamma_n/2\pi$.

In the most general case, the line profile is given by the Voigt profile, i.e. the convolution of the Gaussian and the Lorentzian profile, e. g. Gordon and Sorochenko (2009):

$$\phi_\nu^V(\nu) = \int_{-\infty}^{\infty} \phi_\nu^L(\nu)\phi_\nu^G(\nu)\mathrm{d}\nu. \tag{B31}$$

This can be written in terms of the Voigt function $[H(a,u)]$ by using the proper normalization:

$$\phi_\nu^V(\nu) = \frac{1}{\Delta\nu_D\sqrt{\pi}}H(a,u) \quad \text{(B32)}$$

$$H(a,u) = \frac{a}{\pi}\int_{-\infty}^{\infty}\frac{e^{-y^2}\mathrm{d}y}{a^2+(y-u)^2}, \quad \text{(B33)}$$

with $a=\gamma/\Delta\nu_D$ and $u=(\nu-\nu_0)/\Delta\nu_D$. The FWHM of the Voigt profile can be approximated by:

$$\Delta\nu_V = 0.5346\Delta\nu_L + \sqrt{0.2166\Delta\nu_L^2+\Delta\nu_D^2}, \quad \text{(B34)}$$

where all the widths are expressed in terms of the FWHM value.

B.2 Collisional/Stark broadening

Collisions with electrons produce line broadening:

$$\Delta\nu_{col} = \frac{2}{\pi}\sum_{n\neq n'}N_e C_{n'n}, \quad \text{(B35)}$$

where $C_{n'n}$ is the collision rate for electrons induced transitions from level n' to n, and N_e is the electron density. For levels $n>100$ we fitted the following function to depopulating collisions:

$$\sum_{n\neq n'}N_e C_{n'n} = N_e 10^a \times n^{\gamma_c}. \quad \text{(B36)}$$

Values for a and γ_c are given in Table 5.3. The values used here agree with those from Shaver at low temperatures, but at temperatures larger than about 1000 K they can differ by factors larger than about 4. The values presented here agree well with those of Griem (1967) at large temperatures. At low frequencies, collisional broadening is large and dominates over Doppler broadening in the absence of a background radiation field. As can be seen from the dependence on the electron density, clouds with higher densities have broader lines than those with lower densities at a given level n.

C Radiation broadening

The depopulation of a given level n' due to stimulated transitions is given by:

$$\Gamma_{n'}^{radiation} = \sum_{n\neq n'}B_{n'n}I_\nu. \quad \text{(C1)}$$

Table 5.3: Coefficients for Equation 5.16.

T_e (K)	a	γ_c
10	-10.97	5.482
20	-10.67	5.435
30	-10.49	5.407
40	-10.37	5.386
50	-10.27	5.369
60	-10.19	5.354
70	-10.12	5.341
80	-10.06	5.329
90	-10.01	5.318
100	-9.961	5.308
200	-9.620	5.228
300	-9.400	5.170
400	-9.234	5.122
500	-9.085	5.077
600	-8.969	5.041
700	-8.869	5.009
800	-8.780	4.980
900	-8.701	4.953
1000	-8.630	4.929
2000	-8.272	4.806
3000	-8.009	4.706
4000	-7.834	4.636
5000	-7.708	4.583
6000	-7.613	4.542
7000	-7.538	4.509
8000	-7.477	4.482
9000	-7.427	4.458
10000	-7.386	4.439
20000	-7.181	4.329
30000	-7.113	4.281

where $B_{n'n}$ is the Einstein B coefficient for stimulated transitions from level n' to n, and I_ν is an external radiation field.

We can write the Einstein $B_{n'n}$ coefficients in terms of the Einstein $A_{n'n}$ coefficients:

$$B_{n+\Delta n,n} I_\nu = \frac{c^2}{2h\nu^3} A_{n+\Delta n,n} I_\nu, \tag{C2}$$

(e.g. Shaver 1975 and Gordon and Sorochenko 2009) where we have used the $n' = n + \Delta n$. Assuming a power-law like radiation field, with temperature $T_R = T_0(\nu/\nu_0)^{\alpha_{pl}}$ we can write:

$$B_{n+\Delta n,n} I_\nu = \frac{kT_0}{h\nu_0^{\alpha_{pl}}} A_{n+\Delta n,n} \nu^{\alpha_{pl}-1}. \tag{C3}$$

The Einstein A coefficient can be written in terms of the oscillator strength, $f_{n,n+\Delta n}$ (e.g. Shaver 1975):

$$A_{n+\Delta n,n} = \frac{8\pi^2 e^2 \nu^2}{m_e c^3} \left(\frac{n}{n+\Delta n}\right)^2 f_{n,n+\Delta n}, \tag{C4}$$

Replacing in Equation C3 leads to:

$$\begin{aligned} B_{n+\Delta n,n} I_\nu &= \frac{kT_0}{h\nu_0^{\alpha_{pl}}} \frac{8\pi^2 e^2 \nu^2}{m_e c^3} \left(\frac{n}{n+\Delta n}\right)^2 f_{n,n+\Delta n} \nu^{\alpha_{pl}-1}, \\ &= \frac{8\pi^2 e^2}{m_e c^3} \left(\frac{kT_0}{h\nu_0^{\alpha_{pl}}}\right) \left(\frac{n}{n+\Delta n}\right)^2 f_{n,n+\Delta n} \nu^{\alpha_{pl}+1}. \end{aligned} \tag{C5}$$

Menzel (1968) gives a simple approximation for computing the oscillator strength:

$$\frac{f_{n+\Delta n,n}}{n} \approx M(\Delta n) \left(1 + \frac{3}{2}\frac{\Delta n}{n}\right), \tag{C6}$$

with $M(\Delta n) = 4/3 J_{\Delta n}(\Delta n) J'_{\Delta n}(\Delta n)/\Delta n^2$, where $J_{\Delta n}(\Delta n)$ is the Bessel function of order Δn. The $M(\Delta n)$ can be approximated by $M(\Delta n) \approx 0.1908/\Delta n^3$ to less than 16% in accuracy for $\Delta n = 5$, and to better than 3% accuracy, by changing the exponent from 3 to 2.9. The values for $M(\Delta n) = 0.1908,\ 0.02633,\ 0.008106,\ 0.003492,\ 0.001812$ for $\Delta n = 1,\ 2,\ 3,\ 4,\ 5$.

The frequency of a line in the hydrogenic approximation is given by:

$$\nu_{n+\Delta n,n} = RycZ^2 \left(\frac{1}{n^2} - \frac{1}{(n+\Delta n)^2}\right), \tag{C7}$$

$$\approx 2RycZ^2 \frac{\Delta n}{n^3} \left(1 - \frac{3}{2}\frac{\Delta n}{n}\right), \tag{C8}$$

(e. g. Shaver 1975; Gordon and Sorochenko 2009). Replacing ν in Equation C5 and for $Z = 1$, we obtain:

$$B_{n+\Delta n,n}I_\nu = \frac{8\pi^2 e^2 kT_0}{m_e c^3 h\nu_0^{\alpha_{pl}}}\left(\frac{n}{n+\Delta n}\right)^2 M(\Delta n)\left(1+\frac{3}{2}\frac{\Delta n}{n}\right)n \times \left[2Ryc\frac{\Delta n}{n^3}\left(1-\frac{3}{2}\frac{\Delta n}{n}\right)\right]^{\alpha_{pl}+1},$$

$$\approx \frac{8\pi^2 e^2 (2Ryc)^{\alpha_{pl}+1} kT_0}{m_e c^3 h\nu_0^{\alpha_{pl}}} M(\Delta n) n \left(\frac{\Delta n}{n^3}\right)^{\alpha_{pl}+1},$$

for $\Delta n/n \ll 1$. Rearranging the expression we arrive to:

$$\begin{aligned} B_{n+\Delta n,n}I_\nu &= \frac{8\pi^2 e^2 (2Ryc)^{\alpha_{pl}+1} kT_0}{m_e c^3 h\nu_0^{\alpha_{pl}}} M(\Delta n) n^{-3\alpha_{pl}-2}\Delta n^{\alpha_{pl}+1}, \\ &= \frac{8\pi^2 e^2 (2Ryc)^{\alpha_{pl}+1} kT_0}{m_e c^3 h\nu_0^{\alpha_{pl}}} 0.1908 n^{-3\alpha_{pl}-2}\Delta n^{\alpha_{pl}-2}, \\ &= 2.14\times 10^4 \left(\frac{6.578\times 10^{15}}{\nu_0}\right)^{\alpha_{pl}+1} kT_0\nu_0 n^{-3\alpha_{pl}-2}\Delta n^{\alpha_{pl}-2} \quad \text{(C9)} \end{aligned}$$

Evaluating Equation C9 for $T_0 = 22.6\times 10^3$ K, $\nu_0 = 30$ MHz, $\alpha_{pl} = -2.55$ at $n = 100$, and $\Delta n = 1$, we recover formula 2.177 of Gordon and Sorochenko (2009). Assuming $\alpha_{pl} = -2.6$ at a reference frequency of 100 MHz, Equation C9 is:

$$B_{n+\Delta n,n}I_\nu = 0.662 kT_0 n^{5.8}\Delta n^{-4.6}(\mathrm{s}^{-1}). \quad \text{(C10)}$$

Other relevant values are for an optically thick thermal source $\alpha_{pl} = 0$ and an optically thin thermal source $\alpha_{pl} = -2.1$.

The broadening due to a radiation field in terms of the FWHM is:

$$\begin{aligned} \Delta\nu_{rad}(FWHM) &= \frac{2}{\pi}\sum_{\Delta n} B_{n+\Delta n,n}I_\nu, & \text{(C11)} \\ &\approx 5.819\times 10^{-17} T_0 n^{5.8}(1+2^{-4.6}+3^{-4.6}), & \text{(C12)} \\ &= 6.096\times 10^{-17} T_0 n^{5.8}\ (\mathrm{s}^{-1}). & \text{(C13)} \end{aligned}$$

C.1 The FIR fine structure line of C^+

The beam averaged optical depth of the fine structure line of carbon ions for the transition $^2P_{1/2} - {}^2P_{3/2}$ is given by Crawford et al. (1985); Sorochenko and Tsivilev (2000):

$$\tau_{158} = \frac{c^2}{8\pi\nu^2}\frac{A_{3/2,1/2}}{1.06\Delta\nu} 2\alpha_{1/2}\beta_{158} N_{C^+} L, \quad \text{(C14)}$$

where $A_{3/2,1/2} = 2.4\times10^{-6}$ s^{-1}, ν is the frequency of the $^2P_{1/2}-^2P_{3/2}$ transition and $\Delta\nu$ is the FWHM of the line. The $\alpha_{1/2}$ and β_{158} defined by Sorochenko and Tsivilev (2000) are:

$$\alpha_{1/2} = \frac{1}{1+2\exp(-92/T_e)R}, \tag{C15}$$

$$\beta_{158} = 1-\exp(-92/T_e)R. \tag{C16}$$

The definition of R is (Ponomarev and Sorochenko 1992; Payne et al. 1994; see also Paper I):

$$R = \frac{N_e\gamma_e + N_H\gamma_H}{N_e\gamma_e + N_H\gamma_H + A_{3/2,1/2}}, \tag{C17}$$

where γ_e and γ_H are the de-excitation rates due to electrons and hydrogen atoms, respectively. For consistency we used the same values as in Paper I and neglected collisions with H_2.

For the physical conditions considered here, we note that the FIR [CII] line is optically thin for hydrogen column densities of $\sim 1.2\times10^{21}$ cm^{-2}. This corresponds to hydrogen densities of about 400 cm^{-3} and electron densities 6×10^{-2} cm^{-3}, assuming a length of the cloud of 1 pc and width of 2 km s^{-1}. The intensity of the [CII] 158 μm line in the optically thin limit is given by:

$$\begin{aligned} I_{158} &= \frac{h\nu}{4\pi}A_{3/2,1/2}N^+_{3/2}\times L, \\ &= \frac{h\nu}{4\pi}\frac{A_{3/2,1/2}2\exp(-92/T_e)R}{1+2\exp(-92/T_e)R}N_{C^+}, \end{aligned} \tag{C18}$$

with $N^+_{3/2}$ the number density of carbon ions in the 3/2 state, L the pathlength through the cloud along the line of sight and N_{C^+} the column density of carbon ions. Considering radiative transfer effects, the intensity of the line is given by:

$$I_{158} = \frac{2h\nu_0}{\lambda^2}\frac{1.06\Delta\nu(FWHM)}{e^{92/T_{158}}-1}, \tag{C19}$$

with T_{158} defined as:

$$T_{158} = \frac{92}{\ln\left[(e^{92/T_e}e^{\tau_{158}}/R-1)/(e^{\tau_{158}}-1)\right]}. \tag{C20}$$

Chapter 6

Samenvatting

6.1 Het belang van het interstellaire medium

Vrijwel alle informatie die we ontvangen van verschillende astronomische verschijnselen verkrijgen we via licht. Terwijl het meeste licht wat we van de hemel ontvangen afkomstig is van sterren, kunnen onze ogen maar een kleine fractie van het elektromagnetische spectrum zien. Vele interessante fysische verschijnselen gebeuren echter niet op optische golflengten, met name op lange golflengtes van het infrarood tot het radio gebied.

In melkweg stelsels is het merendeel van de baryonische massa is opgesloten in sterren. Daarnaast is er een kleine fractie van ongeveer 10–15van de massa van de Melkweg in de materie tussen de sterren: het interstellaire medium (ISM). Het ISM bestaat voornamelijk uit waterstof (in atomaire en moleculaire vorm), helium, en sporen van zwaardere elementen. Deze zwaardere elementen zijn geproduceerd door nucleosynthese. Nieuwe sterren verrijzen uit het as van vorige generaties van sterren in dichte moleculaire wolken van het ISM. Gedurende hun evolutie injecteren sterren energie in het ISM in de vorm van straling, sterwinden, en straalstromen. Op het einde van hun leven geven sterren grote hoeveelheden materiaal terug aan het interstellaire medium. De meest zware sterren eindigen hun leven in de vorm van een supernova explosie, waarmee een gigantische hoeveelheid aan kinetische energie gepaard gaat. Het materiaal dat vrijgegeven wordt zal gebruikt worden voor een nieuwe generatie van sterren. Uiteindelijk vormt en bepaalt het samenspel van sterren en het interstellaire medium de evolutie van sterrenstelsels.

De interacties van sterren en gas in sterrenstelsels leidt tot de formatie van verschillende fases van het ISM, dat zichzelf manifesteert als een complex, dynamisch systeem. In het algemeen wordt de structuur van het ISM beschreven door drie verschillende hoofdfases. In Figuur 6.1 laten we een diagram zien die de verschillende fases van het ISM beschrijft.

De meest zware sterren (diegene met meer dan acht maal de massa van onze eigen zon) spelen een belangrijke rol in de evolutie van het ISM. Deze zware sterren zenden een grote fractie van hun licht uit in het ultraviolet. Deze emissie van de zware sterren ioniseert het waterstof in hun omgeving en produceert gebieden van hoge temperatuur welke bekend staan als 'HII gebieden'. Op de

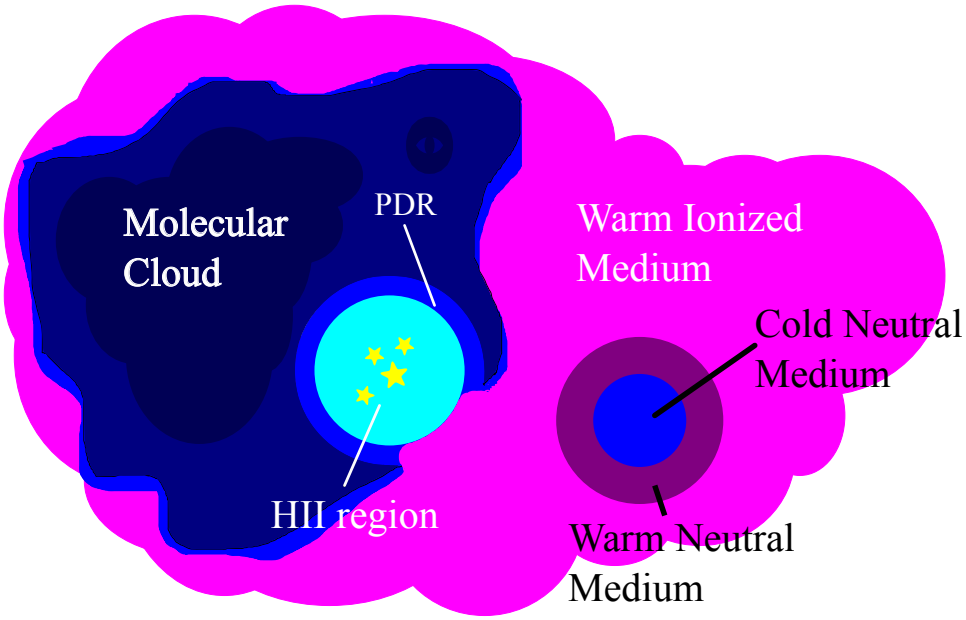

Figure 6.1: De fases van het ISM.

rand van het HII gebied en de wolk waarin dit HII gebied zich bevind vormt zich een photo-dissociatie regio (PDR). In een PDR spelen niet-ioniserende fotonen een grote rol: ze dissociëren moleculen, ioniseren atomen met lagere ionisatie potentialen (zoals C, S, Na), en verhitten het gas.

Een grote fractie van het ISM verkeerd in een neutrale staat omdat de meeste waterstof-ioniserende fotonen (geproduceerd door zware sterren) worden gebruikt om het gas van HII gebieden te geïoniseerd te houden. Het neutrale gas van het ISM is onderverdeeld in twee regimes die vaak worden beschouwd als zijnde in drukevenwicht: het Koude Neutral Medium (KNM), dat bestaat uit koude ($\sim$ 100 K) wolken met een dichtheid van $\sim$ 50 cm^{-3} welke ongeveer 1% van het volume van het sterrenstelsel omvatten; en het Warme Neutral Medium (WNM) met temperaturen van de orde $\sim 10^4$ K, dichtheden van $\sim$ 0.1 cm^{-3} en een veel grotere volumefractie ($\sim$ 30%) vergeleken met het KNM. Deze neutrale fases zijn omgeven door warme (10^4 K) en hete (10^6 K) geïoniseerde gassen. Het warme gas op 10^4 K word gevormd door de (relatief weinige) waterstof-ioniserende fotonen die aan HII gebieden ontsnappen; het hete gas op 10^6 K correspondeert met oude supernova restanten. Met de tijd zal de zwaartekracht

het materiaal in het ISM samenklonteren in moleculaire wolken: de meest dichte gebieden van het Galactische ISM. In deze wolken worden uiteindelijk nieuwe sterren gevormd.

In het KNM is waterstof overwegend neutral. Echter, stellaire fotonen met een energie tussen de 11.2 eV en 13.6 eV kunnen koolstofatomen ioniseren. De diffuse wolken die het KNM opmaken worden verhit door het foto-elektrisch effect op Polycyclische Aromatische Koolwaterstoffen (PAKs) en stofkorrels. De koeling van het gas word gedomineerd door de emissie van de [CII] fijnstructuurlijn op 157 μm. Het KNM en PDRs lijken in vele opzichten op elkaar: in feite kan het KNM worden beschreven als een PDR met een lage dichtheid. Het ISM speelt een belangrijke rol in de evolutie van een sterrenstelsel, omdat het als een reservoir dient voor de producten van nucleosynthese in sterren. Deze producten worden ook als bouwstenen voor de volgende generatie van sterren gebruikt. Deze kringloop van materie in het ISM is echter nog niet goed begrepen, wat vooral te maken heeft met het ontbreken van geschikte observationele methoden om deze processen te kunnen traceren. Om de interacties van sterren met hun omgeving in stervormingsgebieden te bestuderen (zoals HII gebieden en PDRs) hebben we gevoelige observaties nodig op mid- and ver-infraroodgolflengten. Op deze golflengtes liggen de meest belangrijke diagnostische lijnen, en het is dankzij de lancering van de ruimtetelescopen Spitzer in 2003, en Herschel in 2009 dat we deze straling kunnen waarnemen. Daarnaast is in 2010 het Stratospheric Observatory for Infrared Astronomy (SOFIA) begonnen met waarnemen: SOFIA zal de infrarood revolutie van het afgelopen decennium voortzetten.

De neutrale fases van het ISM worden voornamelijk bestudeerd door middel van transities in het ultraviolet (UV) en optische golflengten, alsmede door de 21 cm hyperfijne transitie van neutraal atomair waterstof. Het is echter moeilijk om fysische eigenschappen uit UV en optische lijnen te halen, omdat deze worden beïnvloed door stofextinctie. Het is ook een uitdaging om fysische eigenschappen van het neutrale ISM te achterhalen met de 21 cm lijn, omdat het moeilijk is om koude (KNM) en warme (WNM) componenten van elkaar te scheiden. In deze proefschrift onderzoeken we hoe infraroodwaarnemingen gebruikt kunnen worden om HII gebieden en PDRs te kunnen bestuderen, en bekijken we hoe radio recombinatie lijnen op lage frequenties de eigenschappen van het gas in het KNM kunnen meten. Op deze manier hopen we een eerste stap te zetten naar een beter inzicht in de kringloop van het ISM en de evolutie van sterrenstelsels.

6.2 Koolstof Radio Recombinatie Lijnen op lage frequenties

Recombinatielijnen komen voor wanneer een electron word ingevangen door een ion die zich in een kwantumtoestand bevind die boven de grondstoestand ligt. Onder de juiste fysische condities kan het gerecombineerde electron naar de grondtoestand vallen via tussengelegen kwantumtoestanden: dit proces gaat gepaard met de vorming van recombinatie lijnen. Koolstof kan geïoniseerd zijn in gebieden waar waterstof neutraal is (zoals in het KNM) omdat de ionisatiepotentiaal van koolstof lager ligt dan die van waterstof. Lijnen die worden geproduceerd door koolstof kunnen worden gebruikt om de fysische eigenschappen van het ISM te achterhalen. Transities tussen hoge Rydberg toestanden leiden tot de productie van Koolstof Radio Recombinatie-lijnen (KRRLs) op sub-millimeter tot decameter golflengten. Op deze lange golflengten is stofextinctie niet meer belangrijk (in tegenstelling tot op UV en optische golflengten). De KRRLs zijn gedetecteerd door het gehele ISM van de Melkweg. Om de gebieden te bestuderen waar de KRRLs worden gevormd zijn gedetailleerde modellen nodig. In deze thesis presenteren we dit soort modellen, gebruikmakende van verbeterde methoden en de meest recente botsingsfrequenties. Daarnaast zijn KRRLs erg zwak en hierdoor zijn diepe observaties nodig om deze lijnen te kunnen detecteren in het ISM.

6.3 LOw Frequency ARray (LOFAR)

De Low Frequency ARray (LOFAR) is een *aperture synthesis array* die bestaat uit *phased array* stations. De antennes van elk station vormen een *phased array* die een of meerdere bundels op de hemel produceren. Het combineren van verschillende bundels is een groot voordeel voor het concept van een *phased array*. Het word niet alleen gebruikt om de efficiëntie van de observaties te vergroten, maar kan ook belangrijk zijn voor het kalibreren van deze observaties. De *phased array* stations worden gecombineerd in een groot *aperture synthesis array*. De stations liggen verspreid over een groot oppervlak in Nederland en in Europa. Er zijn twee verschillende antenne soorten: de Lage Band Antenna (LBA) werkt tussen 10 en 90 MHz, terwijl de Hoge Band Antenna (HBA) tussen 110 en 250 MHz werkt. De observatiestations liggen verspreid in een gebied met een diameter van ongeveer 100 kilometer in het noordoosten van Nederland. Andere observatiestations liggen in Duitsland, Zweden, het Verenigd Koninkrijk en Frankrijk.

LOFAR opent het lage frequentie gebied van de hemel voor het bestuderen van KRRLs door midel van zijn hoge gevoeligheid en groot oplossend vermogen. Recente hoge resolutie (40 boogseconden) observaties van KRRLs

met LOFAR hebben de structuur van de wolken blootgelegd in de gezichtslijn naar Cas A. Daarnaast geeft de hoge spectrale resolutie van LOFAR voor het eerst de gelegenheid om verschillende snelheidscomponenten te onderscheiden op lage frequenties. Nieuwe detecties van KRRLs naar Cyg A en de eerste detectie buiten ons sterrenstelsel (in M82) geven weer hoe belangrijk LOFAR kan zijn in het onderzoek naar KRRLs.

De eerste studies laten zien dat het nu mogelijk is om grote programma's uit te voeren waarmee het gehele Melkwegvlak in kaart kan worden gebracht met radio recombinatie lijnen op lage frequenties. Hiermee kunnen we op een nieuwe manier het diffuse ISM bestuderen. De nieuwe observaties hebben ons gemotiveerd om de bestaande recombinatie lijn theorie en resultaten van eerdere studies opnieuw te onderzoeken. Daarnaast bestuderen we de invloed van verschillende factoren op de gemeten lijnsterktes, zoals temperatuur, dichtheid, en externe stralingsvelden.

6.4 Het belang van PAKs en interstellair stof

Stofdeeltjes zijn een belangrijk bestanddeel van het Interstellair Medium. Deze deeltjes bestaan hoofdzakelijk uit twee zeer verschillende chemische componenten: koolstof houdende deeltjes en silicaten. Ze dragen bij aan de extinctie van licht op ultraviolette en optische golflengten, waarbij ze sterlicht absorberen en opnieuw uitzenden op langere golflengten. Op die manier domineren de stofdeeltjes het infrarode en sub millimeter deel van het spectrum. De lichtkracht van (ultra) heldere infrarode sterrenstelsels [(U)LIRGs] en starburststelsels (sterrenstelseles waarin met een uitzonderlijk hoge snelheid stervorming plaatsvindt) wordt grotendeels veroorzaakt door emissie van stofdeeltjes. Deze infrarode emissie kan een handig middel zijn voor het traceren van starburststelsels. Emissie door stof is waargenomen in sterrenstelsels met een zeer hoge roodverschuiving van $z \approx 9$ (toen het universum ongeveer 600 miljoen jaar oud was) en is daarom een belangrijke indicator van de eigenschappen van sterrenstelsels op hoge roodverschuiving.

Bij lage temperaturen en hoge dichtheden kunnen er zich moleculen vormen op het oppervlak van de stofdeeltjes, waardoor ze de chemie in het ISM aandrijven. In protoplanetaire schijven vormen stofdeeltjes bovendien de bouwstenen voor rotsachtige planeten. Het is algemeen bekend dat stofdeeltjes worden gevormd door condensatie in de wind van asymptotische reuzentaksterren (AGB-sterren), Wolf-Rayet sterren, novae en in de ejecta van supernovae. Echter, de mate waarin deze objecten stof produceren is zeer onzeker en het wordt dan ook algemeen aangenomen dat een groot deel van het stof geproduceerd is in het ISM.

Stofdeeltjes hebben een verdeling in grootte die uiteenloopt van kleine polycyclische aromatische koolwaterstof deeltjes (PAK), grote koolstof houdende moleculen gevormd door koolstofringen, die in het infrarood in brede banden licht uitzenden; tot koolstofhoudende en silicaatstofkorrels van ongeveer een micron groot. Extinctie metingen laten zien dat de verdeling in grootte verandert met de positie in de Melkweg. Het is aangetoond dat deze verdeling kan worden omschreven met een machtswet $n(a) \propto a^{-3.5}$, waarbij a de straal van het deeltje is. Deze machtswet wordt gewoonlijk aangeduid als de MRN distributie van Mathis et al. (1977).

De eigenschappen van stofdeeltjes veranderen met de omgeving wanneer ze een interactie aangaan met gas en straling. Gedurende de tijd dat stofdeeltjes zich in een moleculaire wolk bevinden, kunnen ze groeien door een mantel van ijs om zich heen te verzamelen en door samenklontering van stofdeeltjes. Stofdeeltjes kunnen daarentegen makkelijk worden vernietigd in schokgolven door sputteren, waarbij ze hun bestanddelen weer vrijgeven in de gasfase. Andere oorzaken van stofdestructie zijn onder meer verdamping wanneer de deeltjes worden blootgesteld aan sterke stralingsvelden en verbrijzeling door onderlinge botsingen.

In Figuur 6.2 laten we modellen van emissie door stof zien voor twee verschillende omgevingen: het diffuse ISM en dichte PDRs. Hier is te zien dat het licht dat door stofdeeltjes wordt uitgezonden, grotendeels wordt waargenomen op golflengten tussen 1 en 1000 μm. Vanaf de grond zijn deze waarnemingen zeer lastig uit te voeren, omdat de atmosfeer van de aarde een groot deel van dit licht blokkeert (zie het bovenste paneel in Figuur 6.3). Een manier om dit probleem van absorptie door de atmosfeer te omzeilen is door op grote hoogtes te gaan waarnemen, waar de hoeveelheid waterdamp gering is en de transmissie door de atmosfeer in het infrarood toeneemt.

6.5 SOFIA FORCAST

Het Stratosferisch observatorium voor infrarood astronomie (The Stratospheric Observatory for Infrared Astronomy, SOFIA) is een telescoop met een 2.7 m diameter spiegel aan boord van een aangepaste Boeing 747SP. Door op grote hoogte te vliegen (12 tot 14 km), kan er boven de waterdamplaag van de atmosfeer worden waargenomen waar de transmissie van infraroodstraling veel effectiever is (Figure 6.3). De waarnemingen met SOFIA zijn gestart in mei 2012 en er wordt verwacht dat het observatorium 20 jaar in gebruik zal zijn.

Onder de instrumenten aan boord van SOFIA bevindt zich de Faint Object InfraRed Camera for the SOFIA Telescope (FORCAST). FORCAST is een mid-infrarood camera met twee kanalen die een korte golflengte detector (SWC,

variërend van 5 tot 25 μm) en een lange golflengte detector (LWC, variërend van 25 to 40 μm) bevat. Een afbeelding kan worden verkregen door de detectoren individueel of gelijktijdig te gebruiken, door middel van een dichroïsche spiegel. Daarbij is FORCAST ook in staat om grism spectroscopie uit te voeren in een golflengte gebied van 5-50 μm. Het golflengte gebied dat door FORCAST kan worden waargenomen is zeer geschikt voor het observeren van emissie door stof in HII gebieden en PDRs, omdat wordt verwacht dat de piek van de spectrale energie distributie (SED) van het stof zich in dit golflengte gebied bevindt (cf./vergelijk/vgl. Figure 6.2). Daarbij maken het grote blikveld van de FORCAST camera ($\sim 3.2' \times 3.2'$) en de pixelschaal $0.768''$/pixel) het instrument zeer geschikt voor om de grote uitgestrekte gebieden van de Melkwegstelsel te observeren. Nu SOFIA in gebruik is genomen, ligt de mogelijkheid om gedetailleerde en ruimtelijk opgeloste studies uit te voeren van stofemissie in HII gebieden binnen handbereik. De studies van HII gebieden die worden gepresenteerd in dit proefschrift zijn een van de eerste die gebruik maken van de nieuwe mogelijkheden die de SOFIA telescoop ons biedt om de stoffige HII gebieden te kunnen karakteriseren.

6.6 Dit Proefschrift

Dit proefschrift richt zich op de studie van het ISM en bestaat uit twee delen: in het eerste deel presenteren wij een studie van de eigenschappen van het stof in HII regio's en hun omliggende PDR's.

We richten onze studies om twee compacte HII regio's: W3(A) en de Orion Nevel (Hoofdstukken 2 en 3, respectievelijk). Deze twee regio's worden gekarakteriseed door dezelfde eigenschappen, zoals de centrale ster, temperatuur en grootte. Aan de hand van SOFIA/FORCAST waarnemingen hebben we de eigenschappen van stof in het geioniseerde gas, de omliggende PDR's en hun oorspronkelijke moleculaire wolk bestudeerd. Voor Orion hebben we onze waarnemingen aangevuld met *Herschel*/PACS fotometrie, waardoor we de complete infrarode SED van de regio hebben kunnen karakteriseren, inclusief de geëmitteerde infrarode straling van het stof. Eén van de belangrijkste conclusies van dit proefschrift is dat de groei van de stofdeeltjes van invloed is op de verdeling van de stofgrootte in de gebieden waar zware sterren vormen. De grote hoeveelheid archiefdata die beschikbaar is voor Orion maakt het mogelijk om andere belangrijke fenomenen die gerelateerd zijn aan het stof in deze gebied te bestuderen. Een voorbeeld daarvan is het effect van foto-elektrische verhitting en van verhitting via Lyman alfa straling.

Het tweede deel van dit proefschrift presenteert theoretische studies van de eigenschappen van het koude neutrale medium aan de hand van radio recombinatie lijnen van koolstof. Hoofdstukken 4 en 5 bestaan uit de theorie voor

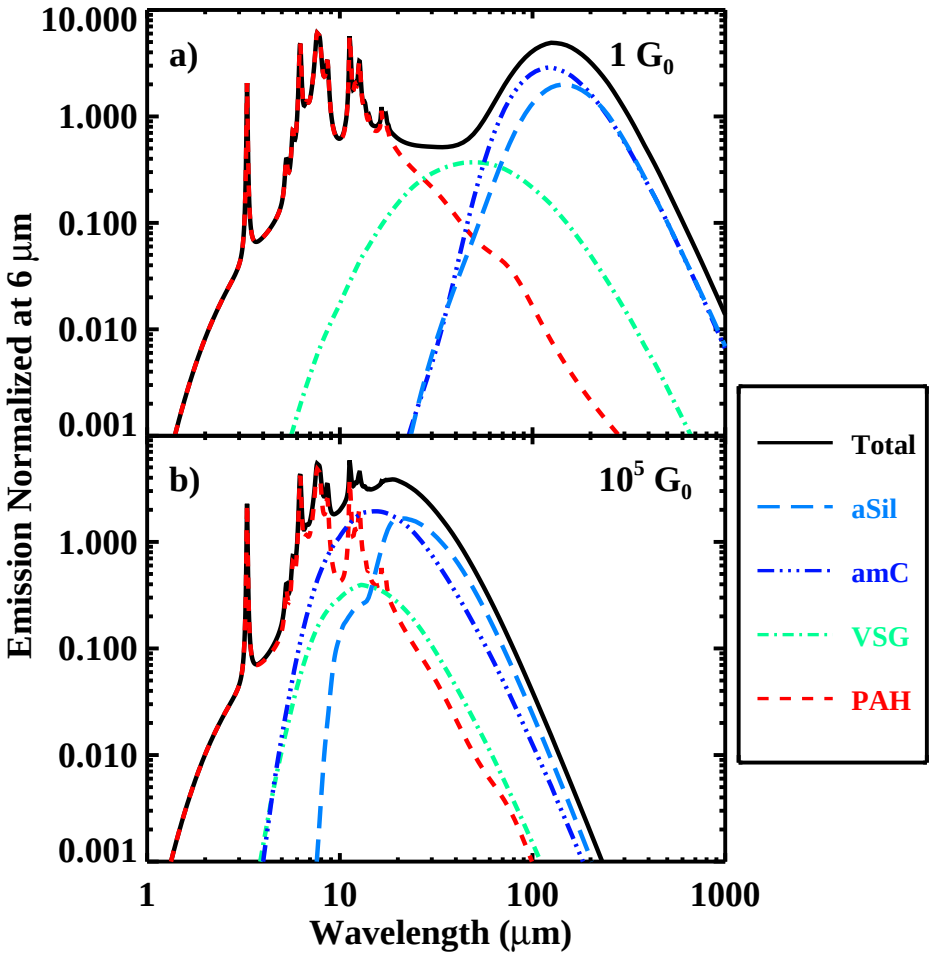

Figure 6.2: Emissie door stof geproduceerd door de Dustem code(Compiègne et al., 2011) voor twee gevallen: a) Onder invloed van een lokaal stralingsveld ($1\ G_0 = 1.6 \times 10^{-3}$ erg s^{-1} cm^{-2}), vergelijkbaar met het stralingsveld dat kan worden geobserveerd in het ISM. b) Onder invloed van een stralingsveld sterker dan het lokale FUV stralingsveld ($10^5\ G_0$), vergelijkbaar met het stralingsveld van een PDR dichtbij een massieve ster. Rode lijnen corresponderen met emissie geproduceerd door PAKs, cyaan kleurige lijnen met emissie door kleine stofdeeltjes, lichtblauwe lijnen met emissie door grote koolstof houdende stofdeeltjes en donkerblauwe lijnen met silicaten.

Koolstof Radio Recombinatie Lijnen; van de vergelijking van niveau populaties (Hoofdstuk 4) tot aan de berekening van de 'radiative transfer' (Hoofdstuk 5). Met deze modellen en waarnemingen van KRRL's kunnen de fysische parame-

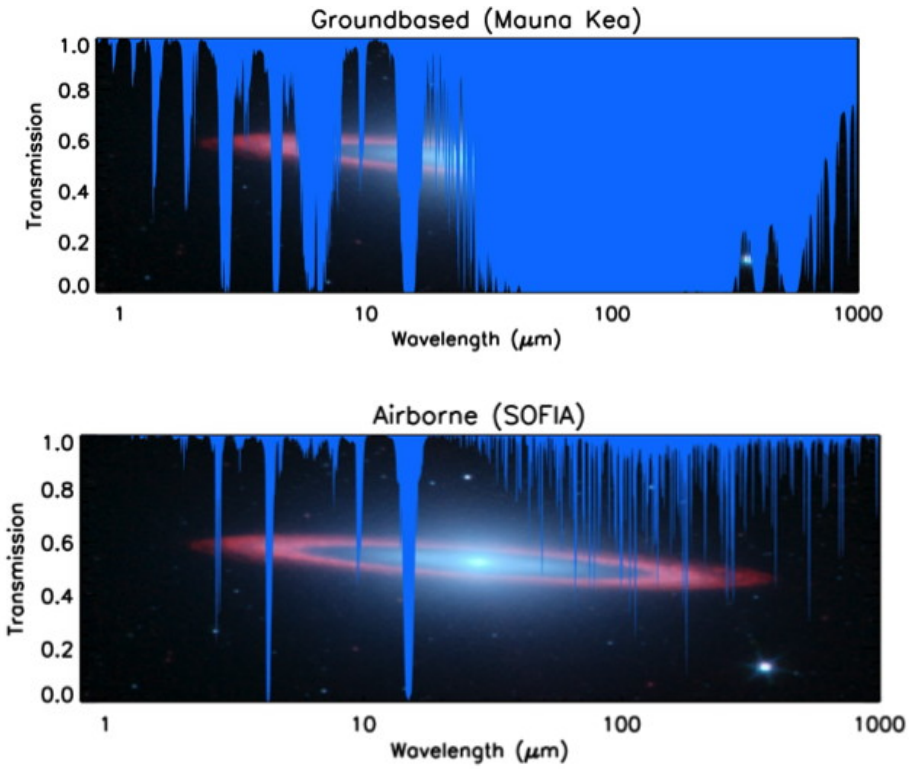

Figure 6.3: Vergelijking tussen de atmosferische transmissie op Mauna Kea en de transmissie die bereikt wordt door SOFIA. Op de hoogtes waar SOFIA kan waarnemen, neemt de atmosferische transmissie neemt in grote mate toe voor golflengten groter dan 20 μm.

ters van de CNM worden bepaald, wat in detail beschreven is in Hoofdstuk 5. De KRRL modellen worden momenteel gebruikt om LOFAR waarnemingen te analyseren.

6.7 De toekomst

Zoals de waarnemingen die in dit proefschrift gepresenteerd worden laten zien zijn de eigenschappen van stof in gebieden van zware stervorming erg verschillend van die van stof in het diffuse ISM. De lancering van de James Webb Space Telescope (JWST) wordt verwacht in oktober 2018 en zal dit vakgebied verder doen uitbreiden. Met een telescoop van 6.5 m zal JWST de grootste spiegel ooit gelanceerd in de ruimte met zich meebrengen. Onder de instrumenten aan boord van JWST heeft het Mid-Infrared Instrument (MIRI)

de mogelijkheid om zowel beeldvormende als spectroscopische studies van stof in HII regio's uit te voeren tussen 5 en 28 μm met een groot oplossend vermogen en een hoge gevoeligheid. De spectroscopische en fotometrische mogelijkheden van de JWST/MIRI kunnen de studie van HII regio's in ons sterrenstelsel uitbreiden zodat zwakkere signalen kunnen worden ontvangen als ook de detectie van nabijgelegen sterrenstelsels. Op deze manier kan een veel groter bereik van fysische karakteristieken (dichtheid, metalliciteit, stellaire cluster grootte, etc.) worden onderzocht met een ongekende resolutie. Zulke studies zijn de sleutel om waarnemingen van massieve-stervorming te begrijpen bij roodverschuivingen van ~ 1.

Zoals de eerste LOFAR studies demonsteren en de resultaten van dit proefschift kwantificeren bieden KRRL's een krachtige manier van onderzoek van de fysische condities in de koude fases van het ISM. De Square Kilometer Array (SKA) zal de volgende generatie van laag-frequente sterrenwachten zijn en zal daarmee onze studies van KRRL's aanzienlijk verbeteren. Aangezien het SKA op het zuiderlijk halfrond gesitueerd zal zijn is het mogelijk om het Galactisch Centrum en de Magelhaense Wolken in kaart te brengen in de zoektocht naar KRRL's. SKA is uitstekend geschikt voor studies binnen de Melkweg van het gedrag van KRRL's op grote en kleine schaal als ook voor extragalactische studies.

Curriculum Vitae

I was born on the 8th of July 1983 in Santiago, Chile; a rainy Friday as my parents have told me. I was a curious child, always asking questions and tearing apart my toys and other devices just to figure out how things work. I was lucky enough to have at my home in San Miguel a large library, with books from philosophy to general relativity; from literature to electrical engineering.

I coursed my primary studies at *Liceo Manuel Arriarán Barros*, a catholic school in La Cisterna, Santiago. I made really good friendships that I maintain to this day. Since I was a good student my parents decided to change me to a better school and my secondary studies were at *Instituto Nacional*, a prestigious public high-school in Santiago, Chile. I made some of my best friends there, sharing time with them discussing all kinds of topics from politics and religion to music and films.

I started my graduate studies under the *Plan Común* at Universidad de Chile in Santiago, a joint program for Engineering and Science studies. After finishing the *Plan Común*, I enrolled in the Electrical Engineering and Physics courses. After the first year, I decided to continue studying Physics and drop my Electrical Engineering studies. Finally, due to the similarity of the curricula, I decided to study Astronomy on top of Physics. From the Physics program, the most fun I had was working on the final project in the lab, in particular with Manuel Merello on the formation of SiC.

I finished my BSc studies on Astronomy and continued in the Master program in Astronomy at Universidad de Chile, where I worked under the supervision of Prof. Dr. Mario Hamuy on the use of type Ia supernovae as standard candles with data from the Carnegie Supernova Project (CSP). This was the first time that I felt working on a problem that was at the edge of the scientific knowledge. During the Master thesis, I learned all the processes involved in the analysis of optical imaging: from observations to the analysis, and the physics of supernovae; it was quite a rewarding experience. However, I wasn't completely sure whether to continue on Astronomy or not. At around that time, Mario told me about an open position at Las Campanas Observatory as a research assistant. It was part of the CSP program and it seemed to me like

a nice opportunity to see what to me was the "real" astronomy.

On 2008, I started to work at Las Campanas Observatory as a research assistant for the CSP. During this time at Las Campanas I greatly improved my skills on programming as well as creating, developing and maintaining the pipelines. I was well guided by Carlos Contreras and Luis Boldt in that task. The interaction with other astronomers either visitors or staff, greatly widened my view of astronomy. I vividly recall nice conversations with Wendy Freedman, Barry Madore, Nidia Morrel, Migel Roth, Mark Phillips and Dr. Krzemiński. I really enjoyed the time at the mountain performing observations and at the office in Colina el Pino with Luis, Herman, Abdo and Max.

The great experience that was for me working at Las Campanas motivated me to pursue a PhD. One of the questions that puzzled me during my Master studies was the problem of interstellar dust and decided to be my project during my PhD. I started my PhD studies at Leiden University under the supervision of Prof. Dr. Tielens on 2010 working on the study of PAHs and dust. During this time, I was able to work with observations from telescopes such as Herschel and SOFIA. I learned about the interstellar medium, dust and astrochemistry. I was also challenged by the theoretical study of carbon recombination lines, which started as a small project but ended up being half of my thesis.

Acknowledgements

Finishing a PhD can be a daunting task but with a little help of friends and family it is bearable. While I would like to thank everyone that helped me during the development of this thesis and the time spent in Leiden, there is not enough space to do so. I apologize in advance in case someone that read this lines doesn't find his/her name.

First, I would like to thank my family: Muchas gracias viejillos, sin su apoyo y motivación nada de esto sería posible. A mi hermanilla siempre tu contagiosa alegría me ha hecho sentir mejor en tiempos que he estado triste ademas de apoyarme en todo, muchas gracias.

Arriving to a new country can be an overwhelming experience. However, upon my arrival I was lucky enough to meet Kalle, Carina, Carmen, Jeannette, Olivier, Joseph, Anton and Jean Baptiste. The time spent in picnics, playing koob and poker and mostly having fun was quite endearing.

Luis y Nena, excelentes anfitriones. Hicieron que me sintiera como en casa durante mi primera Navidad y año nuevo lejos de Chile. Herman que me hizo compañia a través de Skype tocando guitarra, como siempre.

Carlos, Emanuele, Gleb, Mher, I greatly appreciate the time spent with you, complaining about life and your funny discussions and stories. Specially when having beers, coffees and cigarettes.

A mis amigos que me visitaron desde Chile: Diego, Navarrete y Alejandro, muchas gracias. Las aventuras por Europa con ustedes las recordaré siempre con carinño.

I would like to thank all of my office mates during these five years in Leiden: Sergio, Karoliina, Silvia, Kirstin, Héctor, Gustavo, Benne and Junfeng.

To the people that have shared their passion for music with me: Andra, Matteo, Mattia and Simon having fun rocking, and to Irene my salsa dancing partner, many thanks.

Thanks to the people at the Sterrewacht that I had the luck to work with: the ISM group, in particular to Alessandra, Annemieke, Bram, Isabel, Lynn, Marcelo, Sascha and Sebastian; and to the CRRL group, Pedro, Leah, Raymond, Carmen, Huub and Xander. I greatly appreciate the work done by the

SOFIA/FORCAST team, without their generosity and help I couldn't have done a large fraction of my thesis.

Nora, mein Liebling, you have supported me during the difficult times of finishing our respective thesis. You have made this time with you one of the best of my life and being with you is certainly the best that has happened to me in Leiden. I'm sure we will share even better moments in the future.

Last, but not least, the Chilean community: Vicente, Camila, Andrea, Seba, Javi, Nico, Pablo, Cristobal, Dani, Mariana and Mariano and our reigning queen, Heather. Gracias por su compañia, alegría y por compartir conmigo ese pedacito de Chile que llevan dentro.

Bibliography

Abergel, A. et al, 2010, *Astron. Astrophys.* **518**, L96

Allamandola, L.J., Hudgins, D.M. and Sandford, S.A., 1999, *Astrophys. J., Lett.* **511**, L115

Allen, C.W., 1973, *Astrophysical quantities*

Allers, K.N. et al, 2005, *Astrophys. J.* **630**, 368

Anantharamaiah, K.R., 1985, *Journal of Astrophysics and Astronomy* **6**, 177

Anantharamaiah, K.R., Erickson, W.C., Payne, H.E. and Kantharia, N.G., 1994, *Astrophys. J.* **430**, 682

Anderson, L.D., Bania, T.M., Balser, D.S. and Rood, R.T., 2011, *Astrophys. J., Suppl. Ser.* **194**, 32

Anderson, L.D. et al, 2012, *Astron. Astrophys.* **542**, A10

Arab, H. et al, 2012, *Astron. Astrophys.* **541**, A19

Asgekar, A. et al, 2013, *Astron. Astrophys.* **551**, L11

Bakes, E.L.O. and Tielens, A.G.G.M., 1994, *Astrophys. J.* **427**, 822

Balick, B., Gammon, R.H. and Doherty, L.H., 1974, *Astrophys. J.* **188**, 45

Barinovs, Ğ., van Hemert, M.C., Krems, R. and Dalgarno, A., 2005, *Astrophys. J.* **620**, 537

Benjamin, R.A. et al, 2003, *Publ.. Astron. Soc. Pac.* **115**, 953

Bennett, C.L. et al, 1994, *Astrophys. J.* **434**, 587

Bennett, C.L. et al, 2003, *Astrophys. J., Suppl. Ser.* **148**, 97

Bernard-Salas, J. et al, 2012, *Astron. Astrophys.* **538**, A37

Berné, O. et al, 2009, *Astrophys. J., Lett.* **706**, L160

Bik, A. et al, 2012, *Astrophys. J.* **744**, 87

Blum, J. and Wurm, G., 2008, *Ann. Rev. Astron. Astrophys.* **46**, 21

Boersma, C., Rubin, R.H. and Allamandola, L.J., 2012, *Astrophys. J.* **753**, 168

Boogert, A.C.A. et al, 2008, *Astrophys. J.* **678**, 985

Boulanger, F. et al, 2005, *Astron. Astrophys.* **436**, 1151

Brocklehurst, M., 1970, *Mon. Not. R. Astron. Soc.* **148**, 417

Brocklehurst, M., 1971, *Mon. Not. R. Astron. Soc.* **153**, 471

Brocklehurst, M., 1973, *Astrophys. Lett.* **14**, 81

Brocklehurst, M. and Salem, M., 1977, *Computer Physics Communications* **13**, 39

Brocklehurst, M. and Seaton, M.J., 1972, *Mon. Not. R. Astron. Soc.* **157**, 179

Brown, R.L. and Knapp, G.R., 1974, *Astrophys. J.* **189**, 253

Buckle, J.V. et al, 2012, *Mon. Not. R. Astron. Soc.* **422**, 521

Burgess, A., 1958, *Mon. Not. R. Astron. Soc.* **118**, 477

Burgess, A., 1965, *Mem R.A.S.* **69**, 1

Burgess, A. and Percival, I.C., 1968, *Advances in Atomic and Molecular Physics* **4**, 109

Calzetti, D. et al, 2007, *Astrophys. J.* **666**, 870

Calzetti, D. et al, 2010, *Astrophys. J.* **714**, 1256

Cardelli, J.A., Clayton, G.C. and Mathis, J.S., 1989, *Astrophys. J.* **345**, 245

Cardelli, J.A., Meyer, D.M., Jura, M. and Savage, B.D., 1996, *Astrophys. J.* **467**, 334

Carey, S.J. et al, 2009, *Publ.. Astron. Soc. Pac.* **121**, 76

Cesarsky, D., Jones, A.P., Lequeux, J. and Verstraete, L., 2000, *Astron. Astrophys.* **358**, 708

Chiar, J.E. and Tielens, A.G.G.M., 2006, *Astrophys. J.* **637**, 774

Churchwell, E., 2002, *Ann. Rev. Astron. Astrophys.* **40**, 27

Churchwell, E. et al, 2009, *Publ.. Astron. Soc. Pac.* **121**, 213

Churchwell, E. et al, 2006, *Astrophys. J.* **649**, 759

Churchwell, E. et al, 2007, *Astrophys. J.* **670**, 428

Compiègne, M. et al, 2011, *Astron. Astrophys.* **525**, A103

Cox, D.P., 2005, *Ann. Rev. Astron. Astrophys.* **43**, 337

Crawford, M.K., Genzel, R., Townes, C.H. and Watson, D.M., 1985, *Astrophys. J.* **291**, 755

Crutcher, R.M., 1977, *Astrophys. J., Lett.* **217**, L109

de Jong, T., Boland, W. and Dalgarno, A., 1980, *Astron. Astrophys.* **91**, 68

DeFrees, D.J. et al, 1993, *Astrophys. J.* **408**, 530

Deharveng, L. et al, 2010, *Astron. Astrophys.* **523**, A6

Desert, F.X., Boulanger, F. and Puget, J.L., 1990, *Astron. Astrophys.* **237**, 215

Dicker, S.R. et al, 2009, *Astrophys. J.* **705**, 226

Dickinson, A.S., 1981, *Astron. Astrophys.* **100**, 302

Doi, T., O'Dell, C.R. and Hartigan, P., 2004, *Astron. J.* **127**, 3456

Draine, B.T., 2003, *Ann. Rev. Astron. Astrophys.* **41**, 241

Draine, B.T., 2009, in *Cosmic Dust - Near and Far*, T. Henning, E. Grün, and J. Steinacker (eds.), Vol. 414 of *Astronomical Society of the Pacific Conference Series*, p. 453

Draine, B.T., 2011, *Astrophys. J.* **732**, 100

Draine, B.T. and Li, A., 2001, *Astrophys. J.* **551**, 807

Draine, B.T. and Li, A., 2007, *Astrophys. J.* **657**, 810

Dupree, A.K., 1974, *Astrophys. J.* **187**, 25

Ellingson, S.W. et al, 2013, *IEEE Transactions on Antennas and Propagation* **61**, 2540

Elmegreen, B.G. and Scalo, J., 2004, *Ann. Rev. Astron. Astrophys.* **42**, 211

Erickson, W.C., McConnell, D. and Anantharamaiah, K.R., 1995, *Astrophys. J.* **454**, 125

Ershov, A.A. et al, 1984, *Soviet Astronomy Letters* **10**, 348

Ferland, G.J. et al, 1998, *Publ.. Astron. Soc. Pac.* **110**, 761

Ferrière, K.M., 2001, *Reviews of Modern Physics* **73**, 1031

Field, G.B., Goldsmith, D.W. and Habing, H.J., 1969, *Astrophys. J., Lett.* **155**, L149

Flower, D.R., 1988, *Journal of Physics B Atomic Molecular Physics* **21**, L451

Galliano, F. et al, 2008, *Astrophys. J.* **679**, 310

Garay, G., Gómez, Y., Lizano, S. and Brown, R.L., 1998, *Astrophys. J.* **501**, 699

Garay, G., Rodriguez, L.F., Moran, J.M. and Churchwell, E., 1993, *Astrophys. J.* **418**, 368

Gee, C.S., Percival, L.C., Lodge, J.G. and Richards, D., 1976, *Mon. Not. R. Astron. Soc.* **175**, 209

Goldberg, L., 1966, *Astrophys. J.* **144**, 1225

Goldberg, L. and Dupree, A.K., 1967, *Nature* **215**, 41

Gordon, M.A. and Sorochenko, R.L. (eds.), 2009, *Radio Recombination Lines*, Vol. 282 of *Astrophysics and Space Science Library*

Griem, H.R., 1967, *Astrophys. J.* **148**, 547

Güdel, M. et al, 2008, *Science* **319**, 309

Hachisuka, K. et al, 2006, *Astrophys. J.* **645**, 337

Haraguchi, K. et al, 2012, *Publ. Astron. Soc. Japan* **64**, 127

Harper, D.A., 1974, *Astrophys. J.* **192**, 557

Harper-Clark, E. and Murray, N., 2009, *Astrophys. J.* **693**, 1696

Harris, S. and Wynn-Williams, C.G., 1976, *Mon. Not. R. Astron. Soc.* **174**, 649

Haslam, C.G.T., Salter, C.J., Stoffel, H. and Wilson, W.E., 1982, *Astron. Astrophys. Suppl.* **47**, 1

Hayes, M.A. and Nussbaumer, H., 1984, *Astron. Astrophys.* **139**, 233

Heiles, C. and Troland, T.H., 2003a, *Astrophys. J., Suppl. Ser.* **145**, 329

Heiles, C. and Troland, T.H., 2003b, *Astrophys. J.* **586**, 1067

Henning, T., 2010, *Ann. Rev. Astron. Astrophys.* **48**, 21

Herrmann, F. et al, 1997, *Astrophys. J.* **481**, 343

Herter, T.L. et al, 2012, *Astrophys. J., Lett.* **749**, L18

Herter, T.L. et al, 2013, *Publ.. Astron. Soc. Pac.* **125**, 1393

Heyminck, S. et al, 2012, *Astron. Astrophys.* **542**, L1

Hirsch, L. et al, 2012, *Astrophys. J.* **757**, 113

Hoang-Binh, D. and Walmsley, C.M., 1974, *Astron. Astrophys.* **35**, 49

Hofner, P. et al, 2002, *Astrophys. J., Lett.* **579**, L95

Hogerheijde, M.R., Jansen, D.J. and van Dishoeck, E.F., 1995, *Astron. Astrophys.* **294**, 792

Hollenbach, D.J. and Tielens, A.G.G.M., 1997, *Ann. Rev. Astron. Astrophys.* **35**, 179

Hollenbach, D.J. and Tielens, A.G.G.M., 1999, *Reviews of Modern Physics* **71**, 173

Howe, J.E., Jaffe, D.T., Genzel, R. and Stacey, G.J., 1991, *Astrophys. J.* **373**, 158

Hummer, D.G. and Storey, P.J., 1987, *Mon. Not. R. Astron. Soc.* **224**, 801

Hummer, D.G. and Storey, P.J., 1992, *Mon. Not. R. Astron. Soc.* **254**, 277

Jacobs, V.L. and Davis, J., 1978, *Phys. Rev. A* **18**, 697

Johnstone, D. and Bally, J., 1999, *Astrophys. J., Lett.* **510**, L49

Jones, A.P., Tielens, A.G.G.M. and Hollenbach, D.J., 1996, *Astrophys. J.* **469**, 740

Kalberla, P.M.W. et al, 2005, *Astron. Astrophys.* **440**, 775

Kalberla, P.M.W. and Kerp, J., 2009, *Ann. Rev. Astron. Astrophys.* **47**, 27

Kantharia, N.G. and Anantharamaiah, K.R., 2001, *Journal of Astrophysics and Astronomy* **22**, 51

Kantharia, N.G., Anantharamaiah, K.R. and Payne, H.E., 1998, *Astrophys. J.* **506**, 758

Kassis, M. et al, 2006, *Astrophys. J.* **637**, 823

Knapp, G.R., Brown, R.L., Kuiper, T.B.H. and Kakar, R.K., 1976a, *Astrophys. J.* **204**, 781

Knapp, G.R., Kuiper, T.B.H. and Brown, R.L., 1976b, *Astrophys. J.* **206**, 109

Konovalenko, A.A. and Sodin, L.G., 1980, *Nature* **283**, 360

Konovalenko, A.A. and Sodin, L.G., 1981, *Nature* **294**, 135

Kraus, S. et al, 2007, *Astron. Astrophys.* **466**, 649

Krijt, S., Ormel, C.W., Dominik, C. and Tielens, A.G.G.M., 2015, *Astron. Astrophys.* **574**, A83

Kulkarni, S.R. and Heiles, C., 1987, in *Interstellar Processes*, D. J. Hollenbach and H. A. Thronson, Jr. (eds.), Vol. 134 of *Astrophysics and Space Science Library*, pp 87–122

Kurtz, S., 2005, in *Massive Star Birth: A Crossroads of Astrophysics*, R. Cesaroni, M. Felli, E. Churchwell, and M. Walmsley (eds.), Vol. 227 of *IAU Symposium*, pp 111–119

Landecker, T.L. and Wielebinski, R., 1970, *Australian Journal of Physics Astrophysical Supplement* **16**, 1

Langhoff, S.R., 1996, *J. Phys. Chem.* **100**, 2819

Lau, R.M., Herter, T.L., Morris, M.R. and Adams, J.D., 2014, *Astrophys. J.* **794**, 108

Lau, R.M. et al, 2013, *Astrophys. J.* **775**, 37

Launay, J.M. and Roueff, E., 1977, *Journal of Physics B Atomic Molecular Physics* **10**, 879

Liu, X.L., Wang, J.J. and Xu, J.L., 2014, *Mon. Not. R. Astron. Soc.* **443**, 2264

Marconi, A., Testi, L., Natta, A. and Walmsley, C.M., 1998, *Astron. Astrophys.* **330**, 696

Martin, P.G., 1988, *Astrophys. J., Suppl. Ser.* **66**, 125

Martins, F., Schaerer, D. and Hillier, D.J., 2005, *Astron. Astrophys.* **436**, 1049

Mathis, J.S., Rumpl, W. and Nordsieck, K.H., 1977, *Astrophys. J.* **217**, 425

McKee, C.F. and Ostriker, E.C., 2007, *Ann. Rev. Astron. Astrophys.* **45**, 565

McKee, C.F. and Ostriker, J.P., 1977, *Astrophys. J.* **218**, 148

Megeath, S.T. et al, 1996, *Astron. Astrophys.* **307**, 775

Meixner, M. et al, 1992, *Astrophys. J.* **390**, 499

Menten, K.M., Reid, M.J., Forbrich, J. and Brunthaler, A., 2007, *Astron. Astrophys.* **474**, 515

Menzel, D.H., 1968, *Nature* **218**, 756

Morabito, L.K. et al, 2014a, *Astrophys. J., Lett.* **795**, L33

Morabito, L.K. et al, 2014b, *Astrophys. J., Lett.* **795**, L33

Morabito, L.K. et al, 2014c, *Mon. Not. R. Astron. Soc.* **441**, 2855

Nakagawa, T. et al, 1998, *Astrophys. J., Suppl. Ser.* **115**, 259

Natta, A., Walmsley, C.M. and Tielens, A.G.G.M., 1994, *Astrophys. J.* **428**, 209

Neugebauer, G. et al, 1984, *Astrophys. J., Lett.* **278**, L1

Ney, E.P., Strecker, D.W. and Gehrz, R.D., 1973, *Astrophys. J.* **180**, 809

Ochsendorf, B.B. et al, 2014a, *Astron. Astrophys.* **563**, A65

Ochsendorf, B.B. and Tielens, A.G.G.M., 2015, *Astron. Astrophys.* **576**, A2

Ochsendorf, B.B. et al, 2014b, *Astron. Astrophys.* **566**, A75

O'dell, C.R., 2001, *Ann. Rev. Astron. Astrophys.* **39**, 99

O'dell, C.R. and Bally, J., 1999, in *Optical and Infrared Spectroscopy of Circumstellar Matter*, E. Guenther, B. Stecklum, and S. Klose (eds.), Vol. 188 of *Astronomical Society of the Pacific Conference Series*, p. 25

O'Dell, C.R. and Harris, J.A., 2010, *Astron. J.* **140**, 985

O'Dell, C.R., Muench, A., Smith, N. and Zapata, L., 2008, *Star Formation in the Orion Nebula II: Gas, Dust, Proplyds and Outflows*, p. 544

O'Dell, C.R. and Yusef-Zadeh, F., 2000, *Astron. J.* **120**, 382

Ojha, D.K. et al, 2004, *Astrophys. J.* **608**, 797

Okada, Y. et al, 2013, *Astron. Astrophys.* **553**, A2

Oonk, J.B.R. et al, 2015a

Oonk, J.B.R. et al, 2015b, *ArXiv e-prints*

Oonk, J.B.R. et al, 2014, *Mon. Not. R. Astron. Soc.* **437**, 3506

Ormel, C.W. et al, 2011, *Astron. Astrophys.* **532**, A43

Ormel, C.W., Paszun, D., Dominik, C. and Tielens, A.G.G.M., 2009, *Astron. Astrophys.* **502**, 845

Ossenkopf, V. and Henning, T., 1994, *Astron. Astrophys.* **291**, 943

Ossenkopf, V. et al, 2013, *Astron. Astrophys.* **550**, A57

Pagani, L. et al, 2010, *Science* **329**, 1622

Paladini, R. et al, 2012, *Astrophys. J.* **760**, 149

Palmer, P., Zuckerman, B., Penfield, H. and Lilley, A.E., 1967, *Nature* **215**, 40

Pankonin, V., Barsuhn, J. and Thomasson, P., 1977, *Astron. Astrophys.* **54**, 335

Pankonin, V. and Walmsley, C.M., 1978a, *Astron. Astrophys.* **67**, 129

Pankonin, V. and Walmsley, C.M., 1978b, *Astron. Astrophys.* **64**, 333

Parmar, P.S., Lacy, J.H. and Achtermann, J.M., 1991, *Astrophys. J., Lett.* **372**, L25

Payne, H.E., Anantharamaiah, K.R. and Erickson, W.C., 1989, *Astrophys. J.* **341**, 890

Payne, H.E., Anantharamaiah, K.R. and Erickson, W.C., 1994, *Astrophys. J.* **430**, 690

Peeters, E. et al, 2002, *Astron. Astrophys.* **381**, 571

Pellegrini, E.W. et al, 2009, *Astrophys. J.* **693**, 285

Pengelly, R.M. and Seaton, M.J., 1964, *Mon. Not. R. Astron. Soc.* **127**, 165

Percival, I.C. and Richards, D., 1978, *Mon. Not. R. Astron. Soc.* **183**, 329

Peters, W.M. et al, 2011, *Astron. Astrophys.* **525**, A128

Petrosian, V., Silk, J. and Field, G.B., 1972, *Astrophys. J., Lett.* **177**, L69

Pilbratt, G.L. et al, 2010, *Astron. Astrophys.* **518**, L1

Pineda, J.L., Langer, W.D., Velusamy, T. and Goldsmith, P.F., 2013, *Astron. Astrophys.* **554**, A103

Planck Collaboration et al, 2014, *Astron. Astrophys.* **566**, A55

Planck Collaboration et al, 2011, *Astron. Astrophys.* **536**, A1

Poglitsch, A. et al, 2010, *Astron. Astrophys.* **518**, L2

Ponomarev, V.O. and Sorochenko, R.L., 1992, *Soviet Astronomy Letters* **18**, 215

Quireza, C., Rood, R.T., Balser, D.S. and Bania, T.M., 2006, *Astrophys. J., Suppl. Ser.* **165**, 338

Rathborne, J.M., Jackson, J.M. and Simon, R., 2006, *Astrophys. J.* **641**, 389

Redman, M.P., Williams, R.J.R. and Dyson, J.E., 1998, *Mon. Not. R. Astron. Soc.* **298**, 33

Robberto, M. et al, 2005, *Astron. J.* **129**, 1534

Roelfsema, P.R. and Goss, W.M., 1991, *Astron. Astrophys. Suppl.* **87**, 177

Roshi, D.A., Kantharia, N.G. and Anantharamaiah, K.R., 2002, *Astron. Astrophys.* **391**, 1097

Rubin, R.H. et al, 2011, *Mon. Not. R. Astron. Soc.* **410**, 1320

Ruch, G.T. et al, 2007, *Astrophys. J.* **654**, 338

Rybicki, G.B. and Lightman, A.P., 1986, *Radiative Processes in Astrophysics*

Salas, P.e.a., 2015

Salgado, F. et al, 2012, *Astrophys. J., Lett.* **749**, L21

Sánchez, S.F. et al, 2007, *Astron. Astrophys.* **465**, 207

Savage, B.D. and Sembach, K.R., 1996, *Ann. Rev. Astron. Astrophys.* **34**, 279

Scalo, J. and Elmegreen, B.G., 2004, *Ann. Rev. Astron. Astrophys.* **42**, 275

Seaton, M.J., 1959a, *Mon. Not. R. Astron. Soc.* **119**, 81

Seaton, M.J., 1959b, *Mon. Not. R. Astron. Soc.* **119**, 90

Shaver, P.A., 1975, *Pramana* **5**, 1

Shuping, R.Y., Morris, M. and Bally, J., 2004, *Astron. J.* **128**, 363

Shuping, R.Y. et al, 2012, *Astrophys. J., Lett.* **749**, L22

Simon, R., Stutzki, J., Sternberg, A. and Winnewisser, G., 1997, *Astron. Astrophys.* **327**, L9

Simón-Díaz, S., Herrero, A., Esteban, C. and Najarro, F., 2006, *Astron. Astrophys.* **448**, 351

Smith, C.H. et al, 1999, *Mon. Not. R. Astron. Soc.* **303**, 367

Smith, N. et al, 2005, *Astron. J.* **130**, 1763

Snow, T.P. and McCall, B.J., 2006, *Ann. Rev. Astron. Astrophys.* **44**, 367

Sorochenko, R.L. and Tsivilev, A.P., 2000, *Astronomy Reports* **44**, 426

Sorochenko, R.L. and Walmsley, C.M., 1991, *Astronomical and Astrophysical Transactions* **1**, 31

Spitzer, Jr., L., 1978, in *Bulletin of the American Astronomical Society*, Vol. 10 of *Bulletin of the American Astronomical Society*, pp 298–303

Spitzer, Jr., L., 1990, *Ann. Rev. Astron. Astrophys.* **28**, 71

Stahl, O. et al, 2008, *Astron. Astrophys.* **487**, 323

Steinacker, J., Pagani, L., Bacmann, A. and Guieu, S., 2010, *Astron. Astrophys.* **511**, A9

Stepkin, S.V., Konovalenko, A.A., Kantharia, N.G. and Udaya Shankar, N., 2007, *Mon. Not. R. Astron. Soc.* **374**, 852

Stepnik, B. et al, 2003, *Astron. Astrophys.* **398**, 551

Storey, P.J. and Hummer, D.G., 1991, *Computer Physics Communications* **66**, 129

Storey, P.J. and Hummer, D.G., 1995, *Mon. Not. R. Astron. Soc.* **272**, 41

Strelnitski, V.S., Ponomarev, V.O. and Smith, H.A., 1996, *Astrophys. J.* **470**, 1118

Tenorio-Tagle, G., 1979, *Astron. Astrophys.* **71**, 59

Tieftrunk, A.R. et al, 1997, *Astron. Astrophys.* **318**, 931

Tielens, A.G.G.M., 2005, *The Physics and Chemistry of the Interstellar Medium*

Tielens, A.G.G.M., 2008, *Ann. Rev. Astron. Astrophys.* **46**, 289

Tielens, A.G.G.M. and de Jong, T., 1979, *Astron. Astrophys.* **75**, 326

Tielens, A.G.G.M. and Hollenbach, D., 1985, *Astrophys. J.* **291**, 722

Tielens, A.G.G.M., McKee, C.F., Seab, C.G. and Hollenbach, D.J., 1994, *Astrophys. J.* **431**, 321

Tielens, A.G.G.M. et al, 1993, *Science* **262**, 86

Tingay, S.J. et al, 2013, *Publ. Astron. Soc. Australia* **30**, 7

Vallee, J.P., 1987, *Astrophys. and Space Science* **133**, 275

Vallee, J.P., 1989, *Astron. Astrophys.* **213**, 295

van der Werf, P.P., Stutzki, J., Sternberg, A. and Krabbe, A., 1996, *Astron. Astrophys.* **313**, 633

van Haarlem, M.P. et al, 2013, *Astron. Astrophys.* **556**, A2

Vriens, L. and Smeets, A.H.M., 1980, *Phys. Rev. A* **22**, 940

Vrinceanu, D., Onofrio, R. and Sadeghpour, H.R., 2012, *Astrophys. J.* **747**, 56

Wada, K. et al, 2013, *Astron. Astrophys.* **559**, A62

Walmsley, C.M. and Watson, W.D., 1982a, *Astrophys. J.* **260**, 317

Walmsley, C.M. and Watson, W.D., 1982b, *Astrophys. J., Lett.* **255**, L123

Watson, D. et al, 2015, *Nature* **519**, 327

Watson, W.D., Western, L.R. and Christensen, R.B., 1980, *Astrophys. J.* **240**, 956

Weaver, H. and Williams, D.R.W., 1973, *Astron. Astrophys. Suppl.* **8**, 1

Weaver, R. et al, 1977, *Astrophys. J.* **218**, 377

Weingartner, J.C. and Draine, B.T., 2001, *Astrophys. J.* **548**, 296

Wen, Z. and O'dell, C.R., 1995, *Astrophys. J.* **438**, 784

Werner, M.W. et al, 1976, *Astrophys. J.* **204**, 420

Wilson, N.J. and Bell, K.L., 2002, *Mon. Not. R. Astron. Soc.* **337**, 1027

Wolfire, M.G. et al, 1995, *Astrophys. J.* **443**, 152

Wolfire, M.G., McKee, C.F., Hollenbach, D. and Tielens, A.G.G.M., 2003, *Astrophys. J.* **587**, 278

Wood, D.O.S. and Churchwell, E., 1989, *Astrophys. J., Suppl. Ser.* **69**, 831

Wright, E.L., 1973, *Astrophys. J.* **185**, 569

Wynn-Williams, C.G., Becklin, E.E. and Neugebauer, G., 1972, *Mon. Not. R. Astron. Soc.* **160**, 1

Wyrowski, F., Schilke, P., Hofner, P. and Walmsley, C.M., 1997, *Astrophys. J., Lett.* **487**, L171

Xu, Y., Reid, M.J., Menten, K.M. and Zheng, X.W., 2006, *Astrophys. J., Suppl. Ser.* **166**, 526

Young, E.T. et al, 2012, *Astrophys. J., Lett.* **749**, L17

Zinnecker, H. and Yorke, H.W., 2007, *Ann. Rev. Astron. Astrophys.* **45**, 481

Zubko, V., Dwek, E. and Arendt, R.G., 2004, *Astrophys. J., Suppl. Ser.* **152**, 211

Zuckerman, B. and Palmer, P., 1968, *Astrophys. J., Lett.* **153**, L145